



Calhoun: The NPS Institutional Archive

DSpace Repository

Theses and Dissertations | 1. Thesis and Dissertation Collection, all items

2009-12

Investigation of advanced personnel armor using layered construction

Ong, Choon Wei Roy.

Monterey, California: Naval Postgraduate School

http://hdl.handle.net/10945/4362

Downloaded from NPS Archive: Calhoun



http://www.nps.edu/library

Calhoun is the Naval Postgraduate School's public access digital repository for research materials and institutional publications created by the NPS community. Calhoun is named for Professor of Mathematics Guy K. Calhoun, NPS's first appointed -- and published -- scholarly author.

Dudley Knox Library / Naval Postgraduate School
411 Dyer Road / 1 University Circle
Monterey, California USA 93943



NAVAL POSTGRADUATE SCHOOL

MONTEREY, CALIFORNIA

THESIS

INVESTIGATION OF ADVANCED PERSONNEL ARMOR USING LAYERED CONSTRUCTION

by

Ong Choon Wei Roy

December 2009

Thesis Advisor:	Robert Hixson
Second Reader:	Jose Sinibaldi

Approved for public release; distribution is unlimited

THIS PAGE INTENTIONALLY LEFT BLANK

REPORT DOCUMENTATION PAGE			Form Approved OMB No. 0704-0188
Public reporting burden for this collection of information is estimated to average 1 hour per response, including the time for reviewing instruction, searching existing data sources, gathering and maintaining the data needed, and completing and reviewing the collection of information. Send comments regarding this burden estimate or any other aspect of this collection of information, including suggestions for reducing this burden, to Washington headquarters Services, Directorate for Information Operations and Reports, 1215 Jefferson Davis Highway, Suite 1204, Arlington, VA 22202-4302, and to the Office of Management and Budget, Paperwork Reduction Project (0704-0188) Washington DC 20503.			
1. AGENCY USE ONLY ***(Leave blank)***	**2. REPORT DATE** December 2009	**3. REPORT TYPE AND DATES COVERED** Master's Thesis	
4. TITLE AND SUBTITLE Investigation of Advanced Personnel Armor Using Layered Construction.		**5. FUNDING NUMBERS**	
6. AUTHOR(S) Ong Choon Wei Roy			
7. PERFORMING ORGANIZATION NAME(S) AND ADDRESS(ES) Naval Postgraduate School Monterey, CA 93943-5000		**8. PERFORMING ORGANIZATION REPORT NUMBER**	
9. SPONSORING /MONITORING AGENCY NAME(S) AND ADDRESS(ES) N/A		**10. SPONSORING/MONITORING AGENCY REPORT NUMBER**	
11. SUPPLEMENTARY NOTES The views expressed in this thesis are those of the author and do not reflect the official policy or position of the Department of Defense or the U.S. Government.			
12a. DISTRIBUTION / AVAILABILITY STATEMENT Approved for public release; distribution is unlimited		**12b. DISTRIBUTION CODE**	

13. ABSTRACT (maximum 200 words)

A new method of constructing personnel armor is investigated. It comprises of a very hard 1st layer to deform and fracture the projectile, an orthotropic 2nd layer to slow down the shock wave propagation in the through-thickness direction, whilst allowing rapid propagation in the transverse directions, a 3rd porous layer to absorb the shock wave energy through PV-work, and a 4th layer to provide confinement for the porous medium. Based on the above armor protection concept, composite plates comprising of Alumina (Al2O3) Ceramic, Dyneema HB25 and porous Polyurethane (PU) foam were constructed to test against baseline armor AISI 4140 steel plate. A hypothetical orthotropic material model closely resembling that of Dyneema HB25 was derived based on fundamental materials engineering relations as well as limited available literature. Material models for the other materials used in this research were based on existing sources. A live firing experiment was conducted to validate this new composite armor against numerical simulations. Through this study, the composite armor has been shown both experimentally and numerically to be more effective in resisting penetration than conventional high strength armor of equivalent (and slightly greater) areal density, and that the material layering sequence is fundamentally correct.

14. SUBJECT TERMS Ceramic, Composite Armor, Dyneema, Orthotropic Materials, Penetration Resistance, Porous Foams.			**15. NUMBER OF PAGES** 109
			16. PRICE CODE
17. SECURITY CLASSIFICATION OF REPORT Unclassified	**18. SECURITY CLASSIFICATION OF THIS PAGE** Unclassified	**19. SECURITY CLASSIFICATION OF ABSTRACT** Unclassified	**20. LIMITATION OF ABSTRACT** UU

NSN 7540-01-280-5500 Standard Form 298 (Rev. 2-89)
Prescribed by ANSI Std. 239-18

THIS PAGE INTENTIONALLY LEFT BLANK

Approved for public release; distribution is unlimited

INVESTIGATION OF ADVANCED PERSONNEL ARMOR USING LAYERED CONSTRUCTION

Ong Choon Wei Roy
Major, Singapore Army
B.Eng (Civil Engineering), National University of Singapore, 2003

Submitted in partial fulfillment of the
requirements for the degree of

MASTER OF SCIENCE IN COMBAT SYSTEMS TECHNOLOGY

from the

NAVAL POSTGRADUATE SCHOOL
December 2009

Author: Ong Choon Wei Roy

Approved by: Robert S. Hixson
Thesis Advisor

Jose O. Sinibaldi
Second Reader

Larraza Andres
Chairman, Department of Physics

THIS PAGE INTENTIONALLY LEFT BLANK

ABSTRACT

A new method of constructing personnel armor is investigated. It consists of a very hard 1st layer to deform and fracture the projectile, an orthotropic 2nd layer to slow down the shock wave propagation in the through-thickness direction, whilst allowing rapid propagation in the transverse directions, a 3rd porous layer to absorb the shock wave energy through PV-work, and a 4th layer to provide confinement for the porous medium. Based on the above armor protection concept, composite plates consisting of Alumina (Al2O3) Ceramic, Dyneema HB25 and porous Polyurethane (PU) foam were constructed to test against baseline armor AISI 4140 steel plate. A hypothetical orthotropic material model closely resembling that of Dyneema HB25 was derived based on fundamental materials engineering relations as well as limited available literature. Material models for the other materials used in this research were based on existing sources. A live firing experiment was conducted to validate this new composite armor against numerical simulations. Through this study, the composite armor has been shown both experimentally and numerically to be more effective in resisting penetration than conventional high strength armor of equivalent (and slightly greater) areal density, and that the material layering sequence is fundamentally correct.

THIS PAGE INTENTIONALLY LEFT BLANK

TABLE OF CONTENTS

I. INTRODUCTION....1
A. BACKGROUND....1
B. LITERATURE RESEARCH....2
1. Ballistic Protection....2
2. Projectile Threats....3
3. Impetus for Ongoing Research....3
4. Approach of Investigation....5

II. MATERIAL MODELING....7
A. CONVENTIONS USED IN THIS STUDY....7
B. CERAMIC MATERIAL MODELING....8
1. Polynomial Equation of State (Johnson-Holmquist Constitutive Model)....8
C. ORTHOTROPIC MATERIAL MODELING....14
1. Hypothetical Material Modeling....16
2. Material Strength Model....18
3. Orthotropic Failure....20
D. POROUS MATERIAL MODELING....22

III. NUMERICAL SIMULATIONS....27
A. AUTODYN® VALIDATION....27
1. TA-TA Impact....27
a. Shock Wave Profile....29
b. Lagrangian vs. Eulerian Code....30
c. Erosion....30
d. Mesh Sensitivity....31
2. W-Ta Impact....31
B. CERAMIC–CERAMIC IMPACT....34
C. D1-D1 IMPACT....34
1. Shock Wave Properties of D-1....36
2. Us-Up Curve....41
D. COMPOSITE PLATE SIMULATION....43

IV. LIVE FIRING VALIDATION....49
A. TEST DESIGN....49
B. CONSTRUCTION OF TARGET SAMPLES....51
C. EXPERIMENTAL SET UP....52
D. LIVE FIRING....54
1. Dyneema HB25....54
2. Steel AISI 4140....56
3. Composite Plates....58
E. COMMENTS FROM THE LIVE FIRING EXPERIMENT....61
1. Dyneema....61

2. Composite Plate....61
3. Ceramic....62
4. Porous PU Foam....62

V. AUTODYN® SIMULATIONS....65
A. D1....66
B. AISI 4140 STEEL PLATE....69
C. COMPOSITE PLATE NUMERICAL SIMULATIONS....74
1. Composite Plate C-D....74
2. Composite Plate C-D1-P1-AL....75
3. Composite Plate C-D1-P2-AL....78
D. COMPARISON (EXPERIMENT VS. AUTODYN®)....79
1. Overall Depth....80
2. Time Taken to Arrest Projectile....80
3. Porous Foams....81
E. COMPARISON (AUTODYN® AT 483M/S)....81
F. LIMITATIONS OF SIMULATIONS AND EXPERIMENTS....82

VI. CONCLUSIONS....85

VII. RECOMMENDATIONS FOR FUTURE WORK....87
A. ACTUAL DYNEEMA HB25 PROPERTIES....87
B. DESIGN OPTIMIZATION....87
C. MATERIAL CHOICE....87
D. HIGHER VELOCITY IMPACT....88

LIST OF REFERENCES....89

INITIAL DISTRIBUTION LIST....91

LIST OF FIGURES

Figure 1. Graphical Illustration Of New Armor Layering Concept 2
Figure 2. Relative Strength/ Tensile Modulus of Advanced Fiber Composites (From [2]) Note that units are in centi-Newtons/deci-tex, which is the load per unit line density. 1 deci-tex is the weight in grams of 10,000m of a single strand of fiber. 3
Figure 3. A Composite Plate Construction Was Shown By Poh To Defeat A Projectile Where A High Strength AISI 4340 Steel Had Failed. 5
Figure 4. 1-2-3 directions correspond to the conventional x-y-z directions. 7
Figure 5. Simplified Relation between Pressure P, and Material Deformation, μ (From [8]) 10
Figure 6. Graphical Interpretation of the Damage Constant, D (From [8]) 11
Figure 7. Strength Model for Ceramic Materials. (From [8]) 12
Figure 8. Stress-strain Behavior of Dyneema Fibers at up to Strain Rates of 1000s-1 (From [15]) 19
Figure 9. Postulated Compaction Behavior of a Ductile Porous Material. (From [18]) 23
Figure 10. Autodyn® Problem Set Up Of Tantalum Flyer Plate Impact 27
Figure 11. Shock Pressure Profile of the Ta-Ta Plate Impact (Impact velocity was 1000m/s) 29
Figure 12. Shock Pressure Profile of the W-Ta Plate Impact (Impact velocity was 1000m/s) 32
Figure 13. Pressure Profile of Ceramic-Ceramic Flyer Plate Impact at 1000m/s 34
Figure 14. Symmetric Plate Impact of D1 Material at 1 km/s. Plates were 200mm Cylindrical Plates of 5 mm and 10 mm Thickness Respectively. (Left) Problem Setup. (Right) Planar Wave Propagation at 2μs after Impact. 35
Figure 15. Gauge History of D1 Material Subjected to a Flyer Impact of the Same Material at 1km/s 35
Figure 16. Set up of a D1-D1 Symmetric Impact of a Bullet on a Larger Target Plate. (Left) Gages are setup in the 11- and 22-directions. (Right) Lateral wave speed is seen to be faster than the through thickness wave speed as exhibited by the shock front. 36
Figure 17. Overall Shock Wave Profile in the 11-direction 37
Figure 18. (Left) Rise Times of the Shock Wave Propagating in the 11-direction. (Right) Rise Times of the Shock Wave Propagating in the 22/33-directions 38
Figure 19. (Left) Impact of Flyer Plate onto D1 in the 22-direction. (Right)Wave Propagation Remains Faster in the 22- direction Compared to the 11-direction. 39
Figure 20. (Left) Shock Profile in the 22-direction. (Right) Shock Profile in the 11-direction. 39
Figure 21. Elastic Wave Moving Ahead of Plastic Wave in the 22-direction. 39
Figure 22. Explanation of the Difference between the Elastic and Plastic Wave Speed. (From [21]) 40

Figure 23. (Left) Plastic Wave at 5km/s Impact Velocity. (Right) Plastic Wave at 10km/s Impact Velocity. 41
Figure 24. Us-Up relationship of the D1 Material in the 11- and 22/33- directions 42
Figure 25. Autodyn® Simulation of an A2 Steel Cylinder Bullet Impacting at 1000m/s onto a Ceramic-D1 Composite Plate. *(Left) Problem setup. (Right) Overall Pressure-Time profile.* 44
Figure 26. Ceramic Material Results. 17.3 GPa Peak Pressure is Observed, with a 3.45km/s Shock Velocity in the 11-direction 44
Figure 27. (Left) Ceramic Shock Profile in the 22/33-direction. (Right) D1 Shock Profile in the 22/33-direction. 45
Figure 28. Shock Wave Propagation is Slowed Down in the 11-direction Due to the Presence of the D1 Material 45
Figure 29. Possible Us-Up Relationship in the 22/33-Direction for D1 Material. (Not to Scale) 46
Figure 30. A2 Tool Steel Cylinder Projectile that was Used in the Experiment. (Rockwell Hardness C 55-56. Yield Strength of 1.8 GPa) 50
Figure 31. Photos Illustrating the Placement Process as well as the Application of Uniform Pressure over the Sample Using Top and Bottom 20mm Mild Steel Plates 52
Figure 32. Schematic of the Gas Gun Facility 52
Figure 33. Photo Showing (a) the Gas Pressure Breech, (b) the entire length of the barrel and (c) the Impact Chamber/ Bullet Catcher 53
Figure 34. Photo Showing (a) the Break Wire Connection, (b) the Impact Chamber, and (c) the High speed Camera Setup 53
Figure 35. Scanning Electron Microscope Picture of Dyneema HB25, Magnified 675 times. Taken at SEM Lab, NPS. [21] 54
Figure 36. Samples of Dyneema HB25 Showing Full Penetration by an E52100 9/32" Steel Ball. 55
Figure 37. High speed photos showing Dyneema before and after penetration by steel sphere. 55
Figure 38. Addition of a Shock Porous Foam in the Rear did not Appear to Help in Resisting Penetration as Can be Seen from the Similar Exit Velocity of the Projectile. 55
Figure 39. Target Samples and the Associated Damage of the AISI 4140 Steel Plate Impacted with ½" A2 Projectile at 596m/s. No Penetration was Observed. 57
Figure 40. Target Samples and the Associated Damage of the AISI 4140 Steel Plate Impacted with ¾" A2 Projectile at 500m/s. No Penetration was Observed. 57
Figure 41. Target Samples and High Speed Camera Frame Photographs and the Associated Damage of the AISI 4140 Steel Plate Impacted with 1" A2 Projectile at 484m/s 58
Figure 42. Sample of C-D Showing Complete Fracture of the Ceramic First Layer, and no Penetration of the Projectile. 59
Figure 43. Sample of C-D-P2-Al Showing Complete Fracture of the Ceramic First Layer, and no Penetration of the Projectile. 60

Figure 44. Sample of C-D-P1-Al Showing Complete Fracture of the Ceramic First Layer, and no Penetration of the Projectile.....60
Figure 45. Dimensions that were measured using a 1/1000th accuracy Venier Calipers 61
Figure 46. D1 Problem Setup. Impact Velocity was the Same as That of the Experiment – 610m/s. (a) Problem Setup of a 9/32"E52100 Steel Ball impacting a D1 Target. (b)Shock Wave Propagation at 1.5μs after Impact. (c)Simulation Residual Velocity was 275 m/s.....66
Figure 47. End State of Autodyn® Simulations Showing Complete Penetration with 275 m/s Residual Velocity. The Actual Damage Sample is on the Right for Comparison Purposes.....67
Figure 48. (Left) Shockspeed of 3.0 km/s was seen to propagate in the 11 direction. (Right) In the 22/33 directions, the shockspeed was 9.9 km/s.....68
Figure 49. Results of Autodyn® Simulations of a ½" A2 Cylinder Projectile Impacting AISI 4140 Steel at 596m/s. (Top Left)Problem Setup of a ½"A2 Steel Cylinder Impacting at 595 m/s onto a AISI 4140 Steel Plate. (Top Right)Projectile is stopped by the Steel Plate. (Bottom Left)Velocity Profile of the Steel Projectile. (Bottom Right)Pressure-Time Profile in the Target Steel Plate. 71
Figure 50. Results of Autodyn® Simulations of a ¾" A2 Cylinder Projectile Impacting AISI 4140 Steel at 500m/s. Peak Interfacial Pressure was 9.52 GPa. (*Top Left)Problem Setup of a ¾"A2 Steel Cylinder Impacting at 500 m/s onto a AISI 4140 Steel Plate. (Top Right)Projectile is stopped by the Steel Plate. (Bottom Left)Velocity Profile of the Steel Projectile. (Bottom Right)Pressure-Time Profile in the Target Steel Plate.* 72
Figure 51. Results of Autodyn® Simulations of a 1" A2 Cylinder Projectile Impacting AISI 4140 Steel at 484m/s. A Peak Interfacial Pressure of 9.07 GPa is Obtained. *(Top Left)Problem Setup of 1"A2 Steel Cylinder Impacting at 484 m/s onto a AISI 4140 Steel Plate. (Top Right)Projectile is shown to penetrate the Steel Plate. (Bottom Left)Velocity Profile of the Steel Projectile with a residual velocity of 137 m/s is obtained. (Bottom Right)Pressure-Time Profile in the Target Steel Plate.* 73
Figure 52. (Left) Problem Setup of 1" A2 Steel Cylinder Rod Impacting at 483 m/s onto a Composite Plate Comprising of Ceramic, and D1 (C-D1). (Right) Velocity Profile showing that the Projectile is stopped after about 0.32 ms. ..74
Figure 53. Results Of Autodyn® Simulations Of Composite Plate (C-D1). (Left) Final Deformation Shape of the Composite Plate. (Right) Bulk Failure and Brittle Fracture of the Ceramic Plate can be observed. 75
Figure 54. Cross Sectional View of the Actual Composite Plate (C-D1) for Comparison. 75
Figure 55. Problem Setup of C-D1-P1-Al Composite Plate. Impact velocity is 481m/s. 77
Figure 56. Shock Wave Propagation in the 11 and 22 directions. Overall Shock Pressure is Shown on the Right. 77

Figure 57. (Left) Peak Pressure Profiles Obtained During the Initial Stages of Impact. (Right) Time Taken for Projectile to Reach Zero Velocity was 0.2 ms. 77
Figure 58. Problem Set up of C-D1-P2-Al Composite Plate. Impact Velocity of 463m/s. Final Deformation Shape is Shown on the Right. 78
Figure 59. Shock Wave Propagation in the 11 and 22 directions. Time Taken to Arrest the Projectile was 0.177ms 79
Figure 60. Comparative Autodyn® Simulation of the Three Composite Plates, C-D1, C-D1-P1-Al, and C-D1-P2-Al, Subjected to Same Projectile Impact at 483 m/s.....82

LIST OF TABLES

Table 1. Material Properties of Technical Ceramic, Alumina 99.5%....13
Table 2. Comparison of Alumina 99.5% and Corbit 98....13
Table 3. Material Properties of Orthotropic Material D1....21
Table 4. Material Properties of PR 6720-GR (Porous Foam) – P2....24
Table 5. Material Properties of PR 6710-GR (Porous Foam) – P1....25
Table 6. Material Properties of Tantalum....28
Table 7. Material Properties of Tungsten....32
Table 8. Comparison of Cb, Cl and Cs between Design Values and Autodyn® Output....42
Table 9. Test Matrix....49
Table 10. Types of Materials Used in Experiment....50
Table 11. Properties of steel projectiles used....50
Table 12. Specifications of Anstrom Bond® Epoxy AB9110LV from Fiber Optic Center Inc....51
Table 13. Test Set 1 - Dyneema HB25....54
Table 14. Test Set 2 - Baseline Armor Steel AISI 4140....57
Table 15. Test Set 3 – Composite Plates using Ceramic (C), Dyneema HB25 (D) and PU Foams (P1 and P2)....59
Table 16. Post Test Measurements of Specimen Damage....61
Table 17. Autodyn® Simulation....65
Table 18. Material Properties of E52100 CARBON STEEL Projectile....67
Table 19. Quantitative Comparison between Autodyn® Results and Those of the Experiment for the Dyneema HB25 Sample....68
Table 20. Material Properties of AISI 4140 STEEL....69
Table 21. Material Properties of AISI A2 TOOL STEEL....70
Table 22. Material Properties of AL 6061-T6....76
Table 23. Comparison of Experimental and Autodyn® Results....79
Table 24. Deformation Calculations from Autodyn® of Composite Plates with Impact Velocity of 483 m/s....82

THIS PAGE INTENTIONALLY LEFT BLANK

ACKNOWLEDGMENTS

I would like to extend my heartfelt thanks to my two professors, Professor Rob Hixson and Professor Jose Sinibaldi, of the Physics Department at the Naval Postgraduate School, Monterey, California, in supporting and advising my work, without which, this project would not have been possible. Their invaluable time, patience, wealth of experience and knowledge has made this project work a wonderful experience, and a great learning opportunity for me.

On behalf of Professor Hixson, Professor Sinibaldi and myself, I would like to thank Professor Frank Zok and the late Professor Anthony Evans of the Mechanical Engineering (ME) Department at the University of California, Santa Barbara (UCSB) for granting us free access to their gas-gun facilities. Without their kind support, this research could never have been completed.

I would also like to thank Kirk Fields, Nell Gamble and Brett Compton of the ME Department of UCSB for their invaluable time and help in conducting the gas-gun live firing experiments for myself and my research partner, Mr. Boey Chung Wai.

Last, but not least, I would like to thank my wife back home in Singapore for her immense emotional support that I continue to receive while being so far away from home and for so long.

THIS PAGE INTENTIONALLY LEFT BLANK

I. INTRODUCTION

A. BACKGROUND

This research is a continuation of prior thesis work done in 2008 by Poh [1] to investigate the feasibility of employing a layered structure for personnel armor, making use of a fundamental understanding of shock waves to decrease projectile velocity, spread out the shock waves laterally away from the axis of penetration, and subsequently absorb the kinetic energy via means of porous compression, and stopping the projectile at a final stopping layer. Success in this domain will potentially allow an innovative change in the way armor plates are currently designed. Potential space and weight savings are anticipated with associated better specific (per unit mass) penetration resistance abilities.

The background of this study was to investigate a new concept in armor plate technology based on fundamental shock physics to stop a projectile penetration in a series of stages:

Stage 1: Momentum Dispersion – Using high yield strength, high impedance materials to resist penetration from compressive forces as much as possible and spread the momentum delivery out with time, thus decreasing impulse.

Stage 2: Wave Spreading – Using special orthotropic composites, with as high a lateral speed of sound as possible to spread shock waves laterally away from the incident axis.

Stage 3: Energy Absorption – Using porous materials to convert kinetic energy into heat and work done in compressing the pores of the material (PV-work).

Stage 4: Penetration Prevention – Final stopping layer to prevent penetration of the projectile with nominal velocity.

Figure 1. illustrates the above idea:

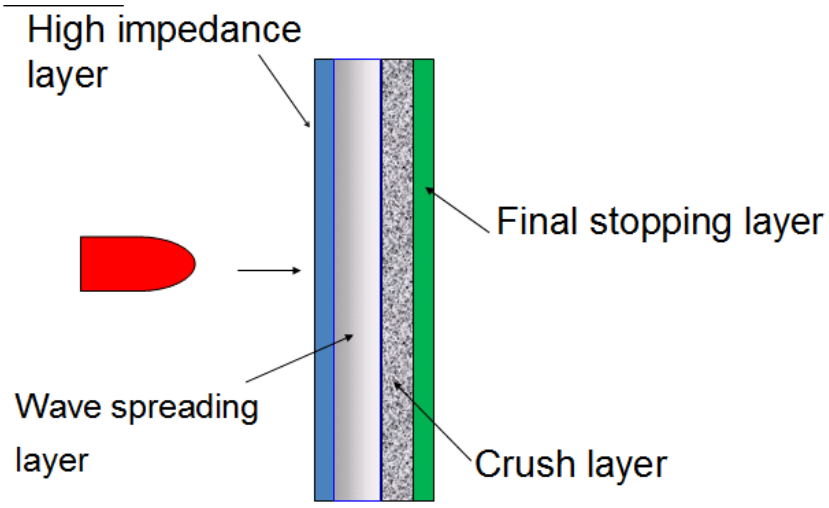


Figure 1. Graphical Illustration Of New Armor Layering Concept

B. LITERATURE RESEARCH

1. Ballistic Protection

Current armor solutions available in the market are typically based on a single type of material to provide penetration protection. In the past, high strength steels (with yield strength in excess of 1 GPa) have performed well against conventional projectile threats given their high yield strength and hardness. However, more advanced high-energy projectile threats have been known to defeat such armor protection fairly easily. Its high density also makes it undesirable as personnel protection. Such material toughness requirements gradually evolved to the use of technical ceramics (Aluminum Oxide, Boron Carbide, Silicon Carbide, Aluminum Nitrates, etc) which are of very high strength and relatively lightweight. Even more advanced materials make use of layering techniques comprised of composite structures. Examples include Kevlar Fiber-Reinforced Polymers (KFRP), Carbon Fiber Reinforced Polymers (CFRP), and Aramid or Polyethylene woven fabric composites. Figure 2. shows a brief classification of these advanced composites. Such evolution of protection technology has had varying success in the defeat of a certain class of projectiles, depending upon the usage requirements. It is possible that the protection level for these existing technologies may have reached a

plateau with marginal improvements within each spiral of armor development.

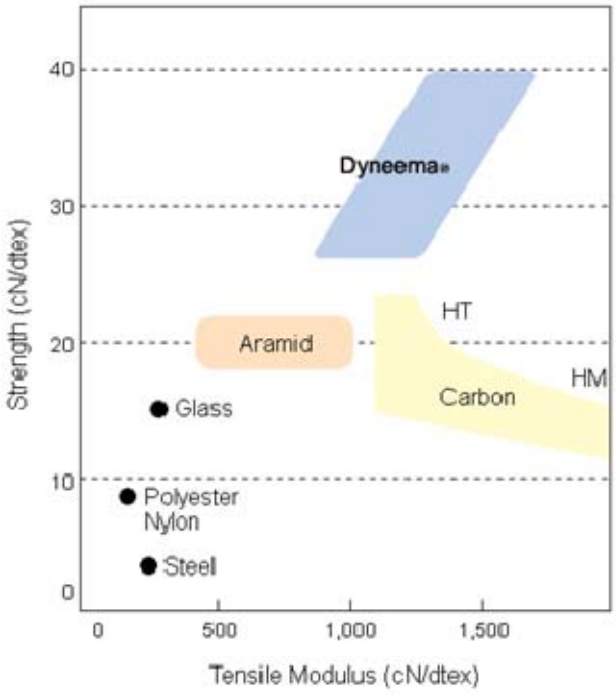


Figure 2. Relative Strength/ Tensile Modulus of Advanced Fiber Composites (From [2]) Note that units are in centi-Newtons/deci-tex, which is the load per unit line density. 1 deci-tex is the weight in grams of 10,000m of a single strand of fiber.

2. Projectile Threats

On the other hand, projectile threats have evolved at a faster pace than armor protection systems, and are becoming increasingly commonplace. Technology such as EFPs (explosively formed projectiles) and shaped charges are now easily discovered and harnessed (and unfortunately, put to use) by rogue nations and terrorist organizations alike. High heat and kinetic energy projectiles are extremely difficult to stop because of the fundamental physics of momentum and energy conservation, which govern the impact event.

3. Impetus for Ongoing Research

Given the evolving projectile threats, it is imperative that new armor protection schemes be developed in order to match up to the challenge of penetration protection.

There has been much interest in the development of armor protection using layered construction in recent years as shown by Robbins et al. [2]. Gupta et al. [3] have shown the effectiveness and feasibility of using a wave spreading layer to dissipate the compressive forces of the incoming projectile, within the μs timescale. Wilkins et al. [4] have shown the effectiveness of ceramics in plastically deforming the projectile thus defeating it from the onset, preventing extensive damage to the lower layers of armor. Herrman [5] has also demonstrated the effectiveness of porous materials and their associated equation of states in absorbing energy due to shock compression. These are all great concepts of armor penetration developed independently. However, work has been lacking in putting these concepts together to synergize into a cohesive armor system.

Poh [1] has shown the feasibility of a composite layered construction made up of quite dissimilar materials each with specific properties to aid penetration resistance of the composite plate. It consists of a hard first layer to plastically defeat the projectile, and a multiple wave spreading layer to laterally dissipate the compressive shock waves. This is then followed by a porous layer to aid energy absorption. Numerical simulation using the Autodyn® hydrodynamic computer code, have shown the benefits of having this sequence of layers to arrest the shock propagation due to a projectile impact, and it was predicted that this type of construction has the potential to outperform an AISI 4340 armor grade high strength steel plate of equivalent thickness. Figure 3. shows a 15mm length, 8mm diameter Tantalum cylinder penetrating completely through a 16mm thick AISI 4340 16mm Steel Plate at an impact velocity of 1000m/s. The same projectile is stopped by a composite plate of the same thickness (16mm).

It is worthwhile to note that this method of armor protection is primarily focused on the early time wave propagation of an impact event, and the ability to rapidly spread out the initial momentum of the projectile upon impact (μs timeframe) through fundamental shock physics theory, with the late time (millisecond timeframe) energy dissipation effects as a secondary objective.

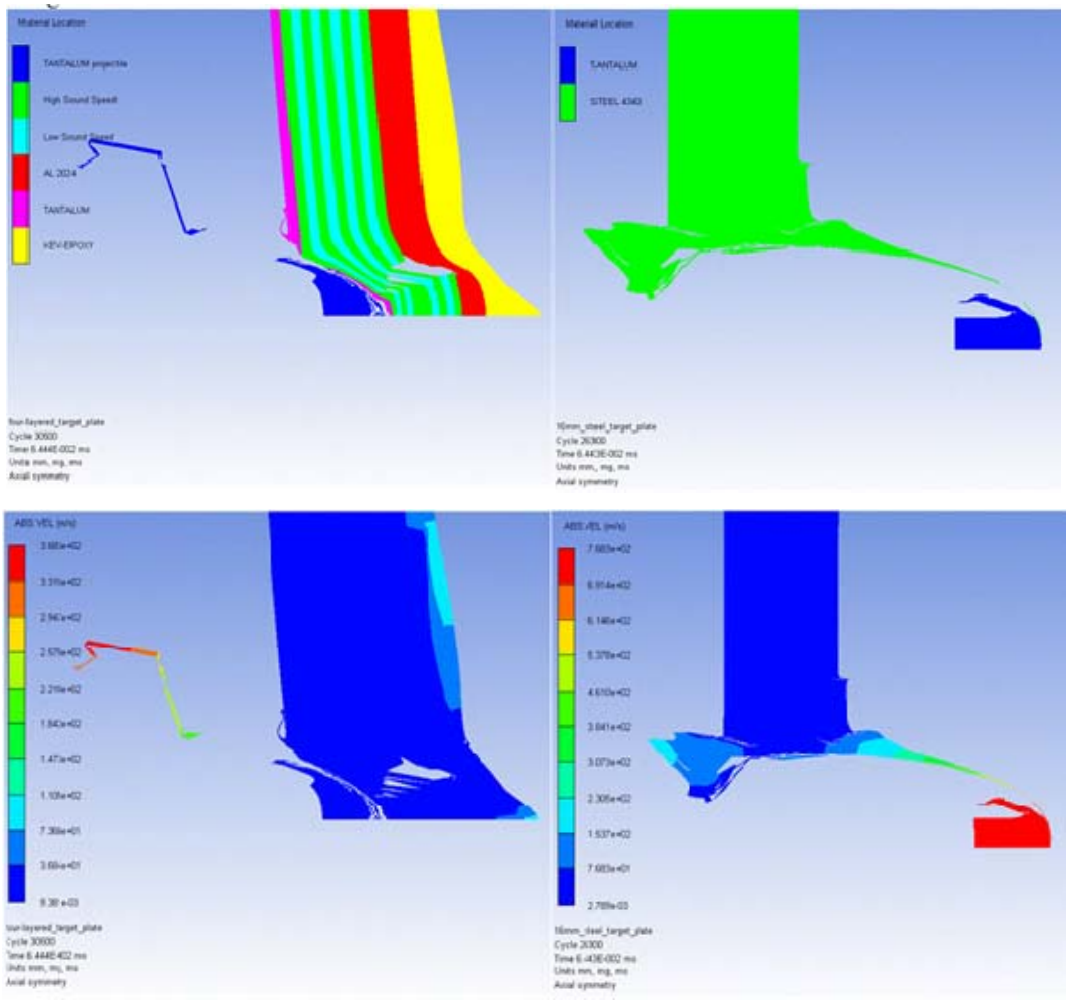


Figure 3. A Composite Plate Construction Was Shown By Poh To Defeat A Projectile Where A High Strength AISI 4340 Steel Had Failed.

4. Approach of Investigation

In view of the novel challenges this project presents, a conservative and careful approach has been taken in order to arrive at the final recommendation. The investigation will begin with a presentation of the relevant material models, equation of states and strength and failure models, which are of concern in this project. This includes ceramics, fiber-based composites, and porous media. This is followed by a brief introduction of the software, Autodyn®, which is to be used for all the numerical simulations in this research. One of the primary focus areas of this research is to simulate the orthotropic

behavior of new generation advanced fiber composites such as Ultra High Molecular Weight Polyethylene (UHMWPE) fibers. A commercially available example is Dyneema®. Results and modeling efforts of porous materials from a concurrent research by Boey [6] are also used to aid in the development of this new composite armor material.

A live firing experiment was conducted to investigate the actual performance of these materials. Following which, numerical simulations of the performance of the composite armor are then generated to validate the numerical models against live firing results. This will give an indication of the accuracy of the simulation models, and provide a benchmark from which further research into this area can be conducted.

II. MATERIAL MODELING

A. CONVENTIONS USED IN THIS STUDY

Generally, the 1-2-3 directions represent the x-y-z directions respectively. This is the convention adopted in this study, as well as Autodyn®. Figure 4. shows the conventions.

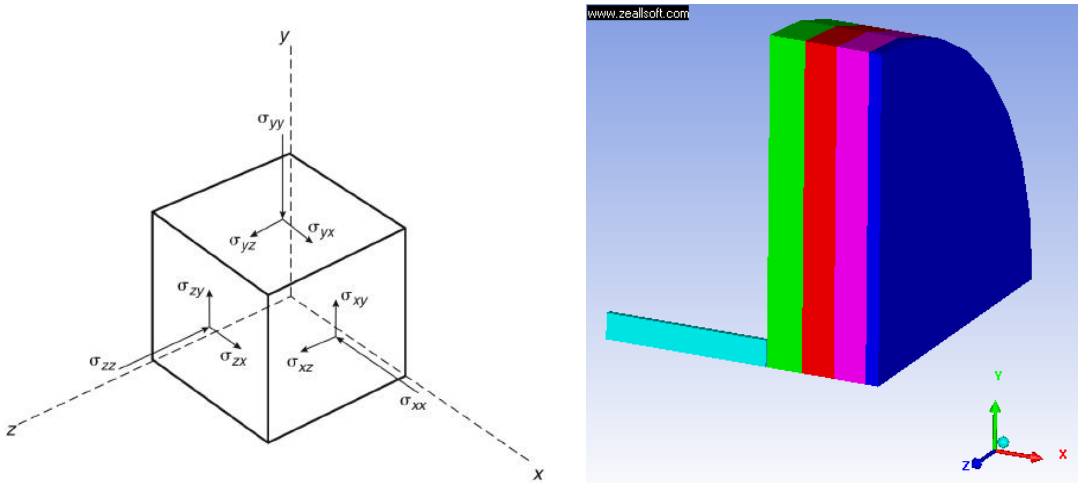


Figure 4. 1-2-3 directions correspond to the conventional x-y-z directions.

Axial symmetry in Autodyn® is symmetry with respect to a rotation about the x-axis. In this study, the x-axis is taken to be the through thickness direction of the target sample.

The ij- subscript of each normal stress or shear component represents the respective force in the i-direction acting on the j-plane. In the case of Poisson ratios (e.g. *v12*) , the ij- subscript represents contraction in the j-direction, when subjected to extension in the i-direction. The simulations in this research were modeled using axial symmetry about the x-axis. This would mean that the 11-direction would refer to the through thickness direction (x-axis), while the 22-direction would refer to the transverse direction (y-axis) of the material samples. Where this is not the convention, it will be indicated clearly in this report.

Dyneema HB25 is a proprietary material manufactured and marketed by Koninklijke DSM N.V. (DSM), a company based in the Netherlands. Where the actual material is used, it is referred to by its given name. In Autodyn® simulations used in this research, it is designated as D1 so as not to confuse readers because the material properties used for this D1 material only approximates that of the Dyneema HB25, and is not intended to match the real material exactly. Actual material properties of Dyneema HB25 have been unavailable in open literature during the period of this research, and until such time when they become available, it is necessary to do detailed material testing on the Dyneema HB25 samples to evaluate relevant properties.

B. CERAMIC MATERIAL MODELING

Technical ceramics (such as Al2O3, SiC, B4C, and AlN) have shown great potential for use as a material for ballistic protection due to their low density, very high compressive strength, and high hardness. However, this benefit comes at a price of brittleness. The dominant failure mechanism of technical ceramics is inevitably that of sudden fracture, and though very strong in compression, they are weak in tension due to their molecular structure and heat treatment process. Many methods of limited and varying successes have been used to overcome, or at least mitigate, the relatively low tensile strength of ceramics, which include confinement and prestressing. Nevertheless, the usefulness of the very high compressive strength of technical ceramics to cause plastic deformation to an incoming projectile can be leveraged in this research study to assist in penetration resistance.

For the purpose of this research, the Al2O3 ceramic is used because it is a well-established material and is currently widely used for ballistic protection purposes. Its properties can also be modeled in Autodyn® fairly accurately.

1. Polynomial Equation of State (Johnson-Holmquist Constitutive Model)

Ceramics are unique in their response to impact loading. Their low ductility makes them very brittle, and when subjected to dynamic impact, there are two distinct

responses. In the first phase, a compressive stress wave initiated at the impact point, spreads out radially within the first few microseconds upon impact. Crack formation occurs when the compressive stress wave intensity exceeds the local dynamic strength of the material. This fracture front travels at the elastic wave speed of the material, and forms a region of pulverized material under the impact location. When the compressive wave meets a free surface (or a surface with lower impedance), it will reflect as a tensile wave as the waves try to travel in opposite directions (incident and reflected). If the dynamic tensile strength of the ceramic material is exceeded, tensile cracking occurs. This is also known as *spall*.

In the millisecond timeframe after initial impact, the second phase of damage occurs and results in large-scale deformation and erosion of the ceramic and projectile. This phase stops only when the projectile fully penetrates the ceramic target, or is stopped by the material. At low impact velocities, the projectile may be defeated with moderate damage to the ceramic surface, and plastic deformation and fracture of the projectile may occur. From intermediate to high impact velocities, and for harder projectiles, both the projectile and the ceramic will undergo erosion (over a few milliseconds timescale). To capture the response of such brittle and sophisticated damage mechanisms, Autodyn® uses the Johnson-Holmquist (JH-2) Constitutive Model, which captures the progressive damage of the ceramic, subjected to impact loading. It requires several material constants to completely (at least numerically) describe the behavior of the particular material. The JH-2 model is described as follows:

a. Initially, the material response is considered to be elastic. With reference from Holmquist [7], its equation of state in Autodyn® is represented simply by a polynomial relationship between the Pressure, P, and the Corresponding Material Deformation, μ. [8].

$$\mu = \frac{\rho}{\rho_o} - 1$$

$For \mu > 0 (compression)$

$$P = A_1\mu + A_2\mu^2 + A_3\mu^3 + (B_0 + B_1\mu)\rho_0 e \qquad (2.1)$$

$For \mu < 0 (tension)$

$$P = T_1\mu + T_2\mu^2 + B_0\rho_0 e$$

b. The constants Ai define the reference curve as shown in Figure 5. , while B0 and B1 describe the amount of bulking of fragments after they have failed, which takes up a greater volume, and thus exert a bulking pressure, Δp, (where $\Delta p = (B_0 + B_1\mu)\rho_0 e$) in the matrix. They are determined by the amount of accumulated damage. The symbol e represents the *energy* of the system. A1 is the bulk modulus of the material.

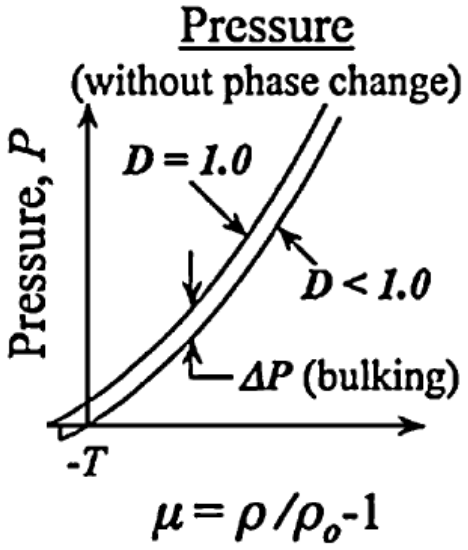


Figure 5. Simplified Relation between Pressure P, and Material Deformation, μ (From [7])

The damage constant, D, ($0 \leq D \leq 1.0$), is defined in (2.2) and shown in Figure 6. :

$$
\begin{aligned}
\Delta D &= \Delta\varepsilon_p / \varepsilon_f \\
D &= \sum(\Delta\varepsilon_p / \varepsilon_p^f) \\
P^* &= P / \sigma_{\max} \\
T^* &= T / \sigma_{\max} \\
\varepsilon_f &= D_1(P^* + T^*)^{D_2} \\
\varepsilon_p^f &= D_1(P^* + T^*)^n
\end{aligned}
\qquad (2.2)
$$

εpf is the plastic strain to failure under the dimensionless pressure P* and T*.

T is the hydrostatic tensile limit of that material at that computation cycle. Where tensile forces exceed T, D=1.0 instantaneously, and the material fails.

εf is the plastic strain to fracture under constant pressure

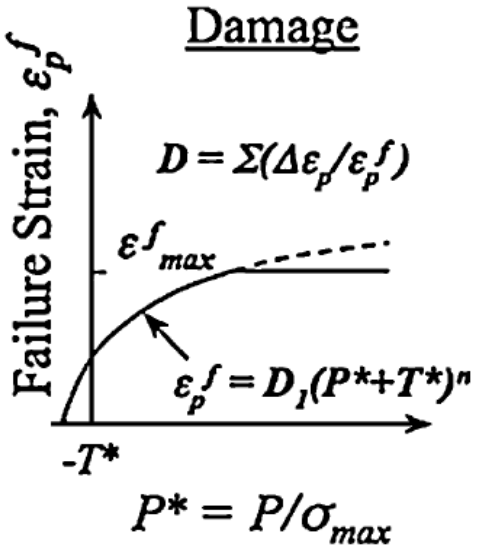


Figure 6. Graphical Interpretation of the Damage Constant, D (From [7])

c. The current material strength is thus determined by the damaged and the undamaged strength curves as well as the current material damage, D. When subjected to tensile forces, the ceramic material responds elastically until the brittle failure point is reached (T*). Subsequent re-compression of the fractured/bulked material will follow the curve described by the “Failed” material (D=1.0)

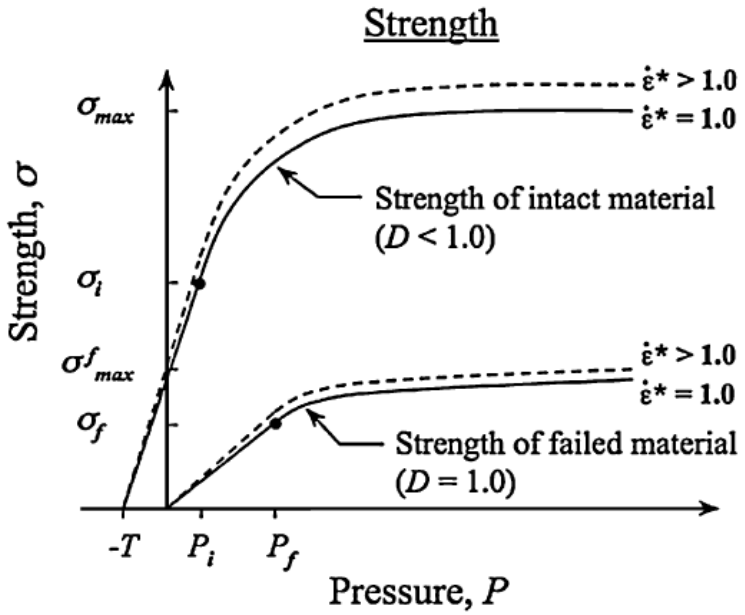


Figure 7. Strength Model for Ceramic Materials. (From [7])

Ceramic materials subjected to tension (decreasing P) follows the D<1.0 curve as shown in Figure 7. . Once fractured, and subjected to recompression (Increasing P), the material follows the D=1.0 curve, which represents the strength of the failed material.

d. The intact material strength is defined as:

$$\sigma_i^* = A(P^* + T^*)^N (1 + C \ln \dot{\varepsilon}^*) \tag{2.3}$$

where $\dot{\varepsilon}^* = \dot{\varepsilon} / \dot{\varepsilon}_0$ and C is a dimensionless strain rate constant. A and N are material constants, and ε0 = 1.0 s-1. The fractured material strength is:

$$\sigma_f^* = B(P^*)^M (1 + C \ln \dot{\varepsilon}^*) \tag{2.4}$$

The current material strength is now a function of both the intact and fractured strength and related by (2.5):

$$\sigma^* = \sigma_i^* - D(\sigma_i^* - \sigma_f^*) \tag{2.5}$$

Although the JH-2 model accounts for strain rate effects through ε*, these effects are typically secondary compared to pressure effects. This has been observed

experimentally by Anderson et al. [9]

Anderson at al. had also experimentally derived the various properties of Alumina (Al2O3) and the values are shown in Table 1. These values have also been adopted and incorporated into the Autodyn® Material Library.

Table 1. Material Properties of Technical Ceramic, Alumina 99.5%

EOS	Polynomial	Strength	Johnson Holmquist	Failure	Johnson Holmquist
Ref Density	3.89 gm/cc	Shear Modulus, G	152 GPa	Hydro Tensile Limit	-0.262 GPa
A1, Bulk Modulus	231 GPa	Model	Continuous JH2	Model	Continuous JH2
A2	-160 GPa	HEL	6.57 GPa	D1	0.01
A3	2774 GPa	A	0.88	D2	0.7
B0	0	N	0.64	Bulking constant, β	1.0
B1	0	C	0.007	Damage	Gradual JH2
T1	231 GPA	B	0.28	Tensile Failure	Hydro Pmin
T2	0	M	0.60	Erosion	Geometric Strain
				Erosion Strain	2.0
				Type	Instantaneous

In this research, the Alumina Ceramic that was used is Corbit 98, manufactured by Industrie Botossi, Italy. It is 98% pure Alumina (Al2O3) with unspecified additives and impurities. Corbit 98 has a specified Young's Modulus of 384 GPa, and density of 3.81 gm/cc. In Autodyn®, based on a Bulk Modulus, K, of 231 GPa, and a Shear Modulus, G, of 152 GPa and using E = 9KG/(3K+G), we can calculate the Young's Modulus, E, as 374 GPa. As shown in Table 2. , this value is within 2.6% of Corbit 98 which we have used in our experiment. Therefore, in the opinion of the author, it is reasonable that we adopt the library values in Autodyn® (for Alumina 99.5%) in our estimation of the performance of Corbit 98.

Table 2. Comparison of Alumina 99.5% and Corbit 98

	Density (gm/cc)	Bulk Modulus, K (GPa)	Shear Modulus, G (GPa)	Young's Modulus, E (GPa)	Remarks
99.5% Al2O3	3.89	231	152	374	E=9KG/(3K+G)
Corbit 98	3.81	-	-	384	Manufacturer Specified
Difference	-2.0%			2.6%	

C. ORTHOTROPIC MATERIAL MODELING

Since the 1990s, polyethylene woven fabrics have seen numerous applications in the areas of ballistic protection and high strength composite applications. Many of these fibers, particularly those made from high-density polyethylene, have remarkably high sound speeds in the direction of the fiber. This unique property leads us to consider this kind of material for use as a wave-spreading (orthotropic) layer to disperse the shock in the lateral direction. This is investigated next.

Of specific interest to this research are Ultra High Molecular Weight Polyethylene (UHMWPE) fibers such as those manufactured by DSM and marketed as "Dyneema HB25." These fibers offer high strength (elastic strength of at least 300 MPa, and up to 700 MPa) and light weight (~0.97 gm/cc) properties, which appeared to us to make them ideal for ballistic protection. Ultimate breaking strength has been reported to be in the region of 1-3 GPa [10]. These fibers are available in layers with identical 0/90˚ fiber orientation, and so fall into a special class of orthotropic materials known as "transversely isotropic." This reduces the Compliance Tensors Matrix (also known as engineering constants) to 5 unknowns from the original 36. Equations (2.6) to (2.14) can be found in [11].

$$\begin{bmatrix} \varepsilon_1 \\ \varepsilon_2 \\ \varepsilon_3 \\ \gamma_{23} \\ \gamma_{31} \\ \gamma_{12} \end{bmatrix} = \begin{bmatrix} S_{11} & S_{12} & S_{13} & 0 & 0 & 0 \\ S_{12} & S_{11} & S_{13} & 0 & 0 & 0 \\ S_{13} & S_{13} & S_{33} & 0 & 0 & 0 \\ 0 & 0 & 0 & S_{44} & 0 & 0 \\ 0 & 0 & 0 & 0 & S_{55} & 0 \\ 0 & 0 & 0 & 0 & 0 & S_{66} \end{bmatrix} \begin{bmatrix} \sigma_1 \\ \sigma_2 \\ \sigma_3 \\ \tau_{23} \\ \tau_{31} \\ \tau_{12} \end{bmatrix} \text{ for Orthotropic} \qquad (2.6)$$

$$\begin{bmatrix} \varepsilon_1 \\ \varepsilon_2 \\ \varepsilon_3 \\ \gamma_{23} \\ \gamma_{31} \\ \gamma_{12} \end{bmatrix} = \begin{bmatrix} S_{11} & S_{12} & S_{13} & 0 & 0 & 0 \\ S_{12} & S_{11} & S_{13} & 0 & 0 & 0 \\ S_{13} & S_{13} & S_{33} & 0 & 0 & 0 \\ 0 & 0 & 0 & S_{44} & 0 & 0 \\ 0 & 0 & 0 & 0 & S_{44} & 0 \\ 0 & 0 & 0 & 0 & 0 & 2(S_{11}-S_{12}) \end{bmatrix} \begin{bmatrix} \sigma_1 \\ \sigma_2 \\ \sigma_3 \\ \tau_{23} \\ \tau_{31} \\ \tau_{12} \end{bmatrix} \text{ for Transversely Isotropic} \qquad (2.7)$$

The coordinate system adopted here is as defined in Chapter I of this thesis. The matrix [Sij] is also known as the Compliance Matrix, and is detailed as follows for Orthotropic materials:

$$[S_{ij}] = \begin{bmatrix} \frac{1}{E_1} & -\frac{\nu_{21}}{E_2} & -\frac{\nu_{31}}{E_3} & 0 & 0 & 0 \\ -\frac{\nu_{12}}{E_1} & \frac{1}{E_2} & -\frac{\nu_{32}}{E_3} & 0 & 0 & 0 \\ -\frac{\nu_{13}}{E_1} & -\frac{\nu_{23}}{E_2} & \frac{1}{E_3} & 0 & 0 & 0 \\ 0 & 0 & 0 & \frac{1}{G_{23}} & 0 & 0 \\ 0 & 0 & 0 & 0 & \frac{1}{G_{31}} & 0 \\ 0 & 0 & 0 & 0 & 0 & \frac{1}{G_{12}} \end{bmatrix} \qquad (2.8)$$

To obtain the Stiffness (Elastic Constant) Matrix, the following relationships are invoked:

$$C_{11} = \frac{1-\nu_{23}\nu_{32}}{E_2E_3\Delta},\ C_{22} = \frac{1-\nu_{13}\nu_{31}}{E_1E_3\Delta},\ C_{33} = \frac{1-\nu_{12}\nu_{21}}{E_1E_2\Delta},\ C_{12} = \frac{\nu_{21}+\nu_{31}\nu_{23}}{E_2E_3\Delta}, \qquad (2.9)$$

$$C_{23} = \frac{\nu_{32}+\nu_{12}\nu_{31}}{E_1E_3\Delta}, C_{13} = \frac{\nu_{31}+\nu_{21}\nu_{32}}{E_2E_3\Delta},\ C_{44} = G_{23},\ C_{55} = G_{31},\ C_{66} = G_{12}$$

where *v*ij are the Poisson ratios in the 1,2,3 directions which is a general representation of the more commonly known Cartesian x,y,z directions. Δ is defined by as:

$$\Delta = \frac{1 - \nu_{12}\nu_{21} - \nu_{23}\nu_{32} - \nu_{31}\nu_{13} - 2\nu_{21}\nu_{32}\nu_{31}}{E_1 E_2 E_3} \tag{2.10}$$

Additional Constraints are:

$$\frac{\nu_{ij}}{E_i} = \frac{\nu_{ji}}{E_j} \; where_i,\, j = 1,2,3_ and_ i \neq j \tag{2.11}$$

And:

(1- v23 v32) > 0, (1- v13 v31) > 0, (1- v12 v21) > 0

Δ > 0, Sii > 0 and Cii > 0 for i=1, 2, 3, 4, 5, 6

E1, E2, E3 and G23, G31, G12 > 0 (2.12)

It can also be shown that the following must be fulfilled for Cii > 0

$$|S_{23}| < \sqrt{S_{22}S_{33}}\,,\; |S_{13}| < \sqrt{S_{11}S_{33}}\,,\; |S_{12}| < \sqrt{S_{11}S_{22}} \tag{2.13}$$

And because of (2.11) we get

$$|\nu_{21}| < \sqrt{\frac{E_2}{E_1}}\,,\; |\nu_{32}| < \sqrt{\frac{E_3}{E_2}}\,,\; |\nu_{13}| < \sqrt{\frac{E_1}{E_3}}\,,\; |\nu_{12}| < \sqrt{\frac{E_1}{E_2}}\,,\; |\nu_{23}| < \sqrt{\frac{E_2}{E_3}}\,,\; |\nu_{31}| < \sqrt{\frac{E_3}{E_1}} \tag{2.14}$$

The above engineering constants and their associated relationships are necessary in order to define the material properties of the hypothetical “D-1” which is intended to closely resemble the real Dyneema HB25 material used in this research.

1. Hypothetical Material Modeling

Based on a density, ρo, of 1.0 gm/cc, and a through-thickness (longitudinal) sound speed of 2 km/s (CL1) and a lateral (transverse) sound speed of 12km/s (CL2,3) as reported by Hearle [12], we shall assume that the shear sound speeds in the two directions are approximately half that of the longitudinal sound speed. That is, CS1 = 1km/s, and CS2,3 = 6km/s. This is known to be approximately true for a wide range of materials.

These assumptions will give us the longitudinal modulus, F, for the material:

F11 = ρo CL12 = 4 GPa

F22/33 = ρo CL2,32 = 144 GPa

The shear modulus, G, of the material is

G23 = ρo CS2,32 = 36 GPa

G12/31 = ρo CS12 = 1 GPa

And thus, the Theoretical Youngs' Modulus can be obtained using (2.15):

$$E = \frac{G(3F - 4G)}{F - G} \tag{2.15}$$

E11 = 2.6667 GPa, and E22 = E33 = 96 GPa

The engineering constants are obtained by defining the Poisson Ratios in the 3-1, 1-2, and 2-3 directions. Based on Literature research, with reference to similar materials such as Kevlar Fiber Reinforced Polymers (KFRP), it was assumed that the hypothetical material will have the following *v* properties:

v31 = 2.52, v12 = 0.07, v23 = 0.07.

The Poisson Ratios for the other directions are easily calculated using the relationship defined by (2.11), and we obtain:

v13 = 0.07, v21 = 2.52, v32 = 0.07.

Note that for Orthotropic materials, Poisson Ratios of > 0.5 (the upper limit for isotropic materials) are relatively common, and are in fact necessary to represent the behavior of the material.

To obtain the Effective Bulk Modulus, K', for the material, the Stiffness Matrix has to be calculated, and the following is obtained (to 5 decimal places):

$$[C_{ij}] = \begin{bmatrix} 4.29660 & 11.64241 & 11.64241 & 0 & 0 & 0 \\ 11.64241 & 128.01990 & 38.30027 & 0 & 0 & 0 \\ 11.64241 & 38.30027 & 128.01990 & 0 & 0 & 0 \\ 0 & 0 & 0 & 36.00000 & 0 & 0 \\ 0 & 0 & 0 & 0 & 1.00000 & 0 \\ 0 & 0 & 0 & 0 & 0 & 1.00000 \end{bmatrix} \quad (2.16)$$

$$\Delta = 2.51 \times 10^{-5} > 0$$

$$K' = \frac{1}{9}[C_{11} + C_{22} + C_{33} + 2(C_{12} + C_{23} + C_{31})] = 42.61184 \text{ GPa} \quad (2.17)$$

The preceding section defines the Equation of State for the Orthotropic Material. These values have been entered into the Autodyn® material library by modifying the existing KFRP model.

2. Material Strength Model

An Orthotropic Yielding Strength Model was chosen to represent the yielding behavior of the Dyneema material. Autodyn® uses the Quadratic Yield Function as defined by Chen et al [13]. It is described as follows:

The yield surface is given by the function, *f*.

$f(\sigma ij) = a11\sigma 211 + a22\sigma 222 + a33\sigma 233 + 2a12\ \sigma 11\sigma 22 +$

$2a23\ \sigma 22\sigma 33 + 2a13\ \sigma 11\sigma 33 + 2a44\sigma 223 + 2a55\sigma 231 + 2a66\sigma 212 = k$ (2. 18)

The 9 constant plasticity coefficients aij describe the amount of anisotropy in plasticity. k is a state variable and varies with the effective inelastic strain of the material, and is used to represent the hardening behavior. The aij being constants means that only isotropic hardening is modeled, i.e. the yield surface can change its size, but not its shape.

It is also shown that the aij's are related to the Plastic Poisson Ratios (PPR's) by (2.19):

$$a_{11} = a_{22}\frac{\nu_{21}^p}{\nu_{12}^p},\ a_{33} = a_{22}\frac{\nu_{23}^p}{\nu_{32}^p},\ a_{11} = a_{33}\frac{\nu_{31}^p}{\nu_{13}^p},$$

$$a_{12} = -a_{22}\nu_{21}^{p},\ a_{23} = -a_{22}\nu_{23}^{p},\ a_{13} = -a_{33}\nu_{31}^{p} \tag{2.19}$$

The six PPR must also satisfy (2.20):

$$\frac{\nu_{21}^{p}}{\nu_{12}^{p}}\frac{\nu_{13}^{p}}{\nu_{31}^{p}} = \frac{\nu_{23}^{p}}{\nu_{32}^{p}} \tag{2.20}$$

For *transversely isotropic* materials, a22=a33=1.0, and for KFRP, a44, a55, a66 =4.0 a11 can be chosen such that the data on the curve is mapped as near to the master σ-ε curve for the material. In view of the lack of a real material for testing, a11 is taken to be 1.50, which is the same as that for the KFRP used in Autodyn®.

The master σ-ε curve is taken (conservatively) to be that as documented by Rodriguez et al [14] for strain rates of 1000/s for Dyneema SK/66. In ballistic tests, it is likely that strain rates approach the order of 100,000/s and will thus give a much higher dynamic yield strength than that approximated by stress strain tests conducted at 1000/s. Autodyn ® approximates this by a 10 point piecewise σ-ε curve, to be input by the user.

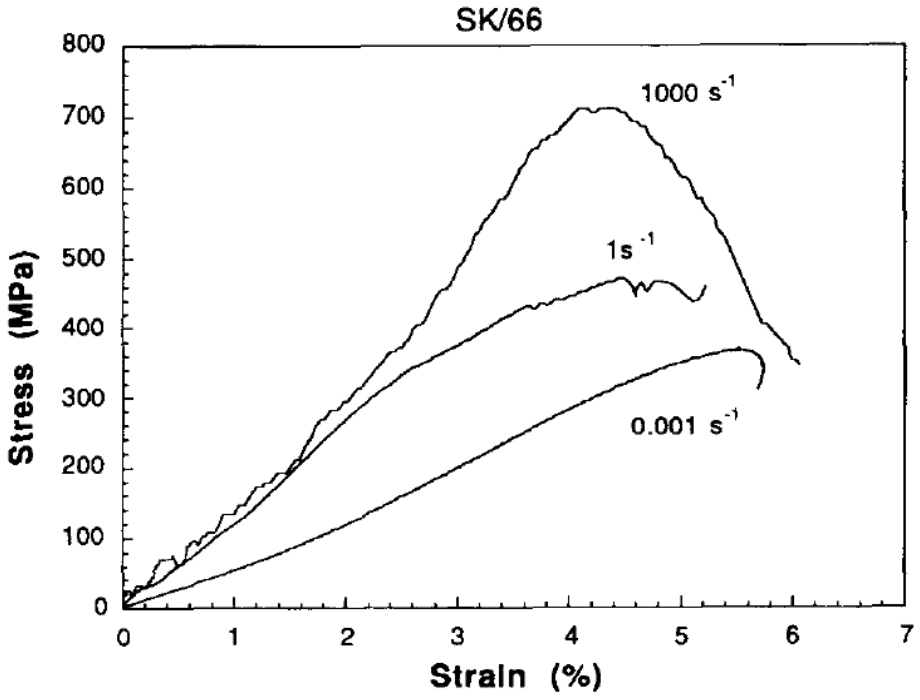


Figure 8. Stress-strain Behavior of Dyneema Fibers at up to Strain Rates of 1000s-1 (From [14])

The other coefficients used are based on the assumption that the "shape" of the yield surface of this transversely isotropic material follows that of the KFRP.

3. Orthotropic Failure

Failure of the transversely isotropic material occurs through a mechanism known as linear softening. A combination of damage mechanisms occurs, such as delamination, matrix cracking, fiber failure, and both through thickness and shear strains. These effects are combined (for problem simplification) into a single phase of deformation called softening. The orthotropic properties allow the material to have residual strength, even after failure. For example, delamination destroys the through thickness tensile strength, but the in-plane tensile strength remains. The failure model in Autodyn® [15] takes into account the "fracture energy," i.e. the area under the σ-ε curve, and a damage coefficient is updated with each iteration.

$$
\begin{aligned}
ii-plane::e_{iif}^2 &= \left(\frac{\sigma_{ii}}{\sigma_{ii,fail}(1-D_{ii})}\right)^2+\left(\frac{\sigma_{ij}}{\sigma_{ii,fail}(1-D_{ij})}\right)^2+\left(\frac{\sigma_{ik}}{\sigma_{ii,fail}(1-D_{ik})}\right)^2\geq 1\\
jj-plane::e_{jjf}^2 &= \left(\frac{\sigma_{jj}}{\sigma_{jj,fail}(1-D_{jj})}\right)^2+\left(\frac{\sigma_{ji}}{\sigma_{jj,fail}(1-D_{ji})}\right)^2+\left(\frac{\sigma_{jk}}{\sigma_{jj,fail}(1-D_{jk})}\right)^2\geq 1 \qquad (2.21)\\
kk-plane::e_{iif}^2 &= \left(\frac{\sigma_{kk}}{\sigma_{kk,fail}(1-D_{kk})}\right)^2+\left(\frac{\sigma_{ki}}{\sigma_{kk,fail}(1-D_{ki})}\right)^2+\left(\frac{\sigma_{kj}}{\sigma_{kk,fail}(1-D_{kj})}\right)^2\geq 1
\end{aligned}
$$

where i-j-k is a more specific representation of the 1-2-3 plane respectively.

Equation (2.21) is checked at each iteration for every element. If any one is exceeded (eiif2 $\geq$ 1), the damage model is used. The material stiffness matrix is then updated in (2.22):

$$
C_{ij}=\begin{bmatrix}
C_{11} & C_{12}(1-MAX(D_{11},D_{22})) & C_{13}(1-MAX(D_{11},D_{33})) & 0 & 0 & 0\\
C_{12}(1-MAX(D_{11},D_{22})) & C_{11} & C_{13}(1-MAX(D_{22},D_{33})) & 0 & 0 & 0\\
C_{13}(1-MAX(D_{11},D_{33})) & C_{13}(1-MAX(D_{22},D_{33})) & C_{33} & 0 & 0 & 0\\
0 & 0 & 0 & C_{44} & 0 & 0\\
0 & 0 & 0 & 0 & C_{55} & 0\\
0 & 0 & 0 & 0 & 0 & C_{66}
\end{bmatrix} \qquad (2.22)
$$

and Dij, i = 1, 2, 3, j = 1, 2, 3 is defined in (2.23) in terms of the inelastic crack strain,

εijcr .

$$D_{ij} = (\frac{L_{ij} F_{ij}^2}{2G_{ij}^f})(\frac{\varepsilon_{ij}^{cr}}{F_{ij}}) \quad (2.23)$$

Fij represents the initial failure stress and in the three axial and 3 shear directions, while Gijf is the fracture energy in the respective directions. Lij is a local characteristic dimension of the numerical integration point in each direction.

Autodyn® requires the user to define Fij and Gij. Due to the lack of further information about D1, and given the tensile failure stress of Dyneema fibers to be in the region of 1-3 GPa, which is about 10 times that of KFRP, and the plastic strain to be about twice that of KFRP, the fracture energies are taken (reasonably) to be about 10 times (1/2 base x height of a triangle) that of the more well known, KFRP. Thus, the material properties of the orthotropic material D1 are completely defined in Table 3.

Table 3. Material Properties of Orthotropic Material D1

EOS - Orthotropic					
Ref. Density	1.00 gm/cc	G 12	1 GPa	Volumetric Response	Polynomial
E 11	2.67 GPa	G 23	36 GPa	Bulk Modulus, A1	42.61
E 22	96 GPa	G 31	1 GPa	A 2	50 GPa
E 33	96 GPa	Ref Temp	300 K	A 3	0 GPa
V 12	0.07	Specific Heat	1420 J/kgK	B 0	0
V 23	0.07	Thermal Conductivity	0 J/mKs	B 1	0
V 31	2.52			T 1 (=A1)	42.61 GPa
				T 2	0 GPa

Strength Model - Orthotropic Yield					
A 11	1.5	Eff Stress #1	20.0 MPa	Eff Plastic Strain #1	0.000
A 22	1.0	Eff Stress #2	75.0 MPa	Eff Plastic Strain #2	0.005
A 33	1.0	Eff Stress #3	140.0 MPa	Eff Plastic Strain #3	0.010
A 12	-0.68	Eff Stress #4	200.0 MPa	Eff Plastic Strain #4	0.015
A 13	-0.68	Eff Stress #5	300.0 MPa	Eff Plastic Strain #5	0.020
A 23	-0.26	Eff Stress #6	380.0 MPa	Eff Plastic Strain #6	0.025
A 44	4.0	Eff Stress #7	470.0 MPa	Eff Plastic Strain #7	0.030
A 55	4.0	Eff Stress #8	600.0 MPa	Eff Plastic Strain #8	0.035
A 66	4.0	Eff Stress #9	680.0 MPa	Eff Plastic Strain #9	0.040
		Eff Stress #10	720.0 MPa	Eff Plastic Strain #10	0.045

Failure/ Damage Model- Orthotropic Softening (10 times of KFRP)					
Tensile Failure Stress 11	2 MPa	Tensile Failure Stress 22	2000 MPa	Tensile Failure Stress 33	2000 MPa
Max Shear Stress 12	1.5 MPa	Max Shear Stress 23	1.5 MPa	Max Shear Stress 31	1.5 MPa
Fracture Energy 11	5447.1 J/m2	Fracture Energy 22	300 J/m2	Fracture Energy 33	300 J/m2
Fracture Energy 12	14613 J/m2	Fracture Energy 23	14613 J/m2	Fracture Energy 31	14613 J/m2
Damage Coupling coefficient	1.0				

D. POROUS MATERIAL MODELING

Porous materials have been known to be useful shock wave isolators and absorbers. Fowles and Curran [16] showed that this was because of the ability of the porous material to support appreciable elastic stress before compaction. As such porous materials may prove to be a useful material in ballistic protection.

Herrmann [17] developed a set of constitutive equations to describe the behavior of ductile porous materials in a simple way. The objective was to be able to use the theory to produce reasonable results at both low and high stresses. The method takes into account the thermodynamic behavior at high stresses and also the compaction behavior at lower ones. Figure 9. shows the simplified p-α theory from Hermann.

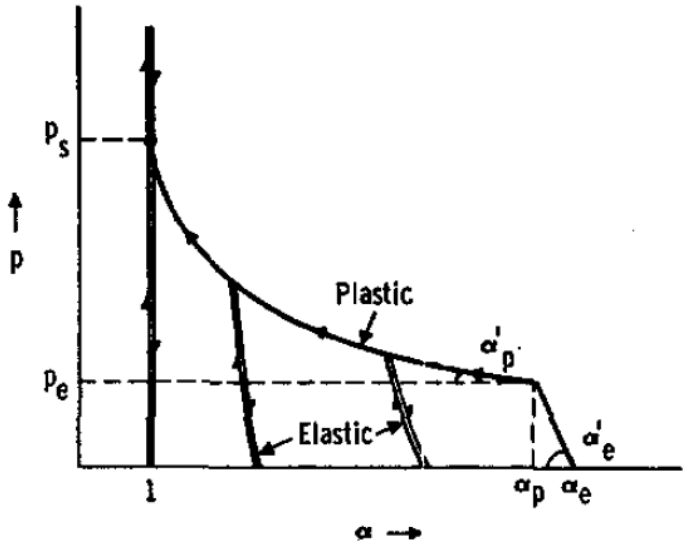


Figure 9. Postulated Compaction Behavior of a Ductile Porous Material. (From [17])

The theory starts by defining a variable known as α.

$$\alpha = v/vs \tag{2.24}$$

where

v is the specific volume of the porous material, and

vs is that of the solid material.

Upon application of compressive pressure, the material is compressed elastically to an initial compaction pressure, pe, and subsequently, it follows a plastic compaction curve towards the solid compaction pressure, ps, before it begins to behave like a solid at α=1.0. For an initially highly distended (high porosity) material, elastic compression mostly occurs through elastic buckling of the cell walls, and permanent volume change coincides with the onset of plastic deformation of the cell walls, occurring at relatively low pressures. For less porous materials, most of the elastic compressions will be due to volume compression of the cell walls with relatively little change to α due to surrounding material confinement. It is assumed that the Hugoniot and Isentrope of the porous material are the same at STP conditions in this simple theory, and the relationship between the shock velocity and particle velocity is linear. This gives the following:

$$\begin{aligned} p_r &= \frac{c_0^2(v_{s0} - v_s)}{[v_{s0} - s(v_{s0} - v_s)]^2} \; and \\ E_r &= \frac{1}{2} p_r (v_{s0} - v_s) \end{aligned} \tag{2.25}$$

where pr and Er are the reference line PV-Hugoniot and Specific Internal Energy respectively.

The solid equation of state is given by the Mie-Gruneisen equation:

$$p = p_r + \frac{(E - E_r)\Gamma}{v_s}$$
$$\frac{\Gamma}{v_s} = \frac{\Gamma_0}{v_{s0}} \qquad (2.26)$$

Where $\Gamma_0 = v_{s0}\beta K_0 / C_p$, is the Gruneisen parameter at ambient conditions, Cp is the specific heat at constant pressure, and K0 is the isentropic bulk modulus. β is the volumetric thermal expansion coefficient.

Hence, based on the above, we only need an initial porous density (1/vs0), the compacted density (1/vs), the ambient Gruneisen parameter, the linear Us-Up relationship, and the specific heat of the porous media in order to define its performance in Autodyn®. Boey [6] deals with the p-α model in greater depth, and provided the parameters, shown in Table 4. Table 5. , of the PU (polyurethane) foam used in this experiment.

Table 4. Material Properties of PR 6720-GR (Porous Foam) – P2

EOS – P-Alpha					
Ref Density	1.265 gm/cc	Solid Compaction Pressure	112.54 MPa	Parameter C1	2.490 km/s
Porous Density	0.3204 gm/cc	Solid EOS	Shock	Parameter S1	1.56
Porous Soundspeed	859.92 m/s	Gruneisen coefficient	1.55	Specific Heat	86 J/kgK

Initial Compaction Pressure	9.64 MPa	Ref Temp	300K	Compaction Curve	Standard
Compaction Exponent	3.0				
Strength Model – Von Mises					
Shear Modulus	68.58 MPa	Yield Stress	9.64 MPa		
Failure Model – Hydro (pmin)		Erosion			
Hydro Tensile Limit	-2 GPA	Erosion Strain	2.0	Geometric Strain	Instantaneous

Table 5. Material Properties of PR 6710-GR (Porous Foam) – P1

EOS – P-Alpha					
Ref Density	1.265 gm/cc	Solid Compaction Pressure	112.54 MPa	Parameter C1	2.490 km/s
Porous Density	0.1602 gm/cc	Solid EOS	Shock	Parameter S1	1.56
Porous Soundspeed	669.44 m/s	Gruneisen coefficient	1.55	Specific Heat	86 J/kgK
Initial Compaction Pressure	2.6 MPa	Ref Temp	300K	Compaction Curve	Standard
Compaction Exponent	3.0				
Strength Model – Von Mises					
Shear Modulus	68.58 MPa	Yield Stress	9.64 MPa		
Failure Model – Hydro (pmin)		Erosion			
Hydro Tensile Limit	-2 GPA	Erosion Strain	2.0	Geometric Strain	Instantaneous

The preceding section defines all the initial material properties of our target plates, which are used throughout this thesis. Projectiles and other materials (such as steel) are given where mentioned, as they are not the focus of this section.

THIS PAGE INTENTIONALLY LEFT BLANK

III. NUMERICAL SIMULATIONS

A. AUTODYN® VALIDATION

1. TA-TA Impact

Prior to starting Autodyn® simulation, it is important that the models and hydrodynamic codes used in Autodyn® be understood in fair amount of detail so that the underlying assumptions and limitations can be captured and taken into consideration when analyzing the results from Autodyn® of calculations on more complex materials. In order to achieve this objective, a basic flyer plate impact was done with a material that was fairly well understood, Tantalum. The problem set up was as shown in Figure 10. :

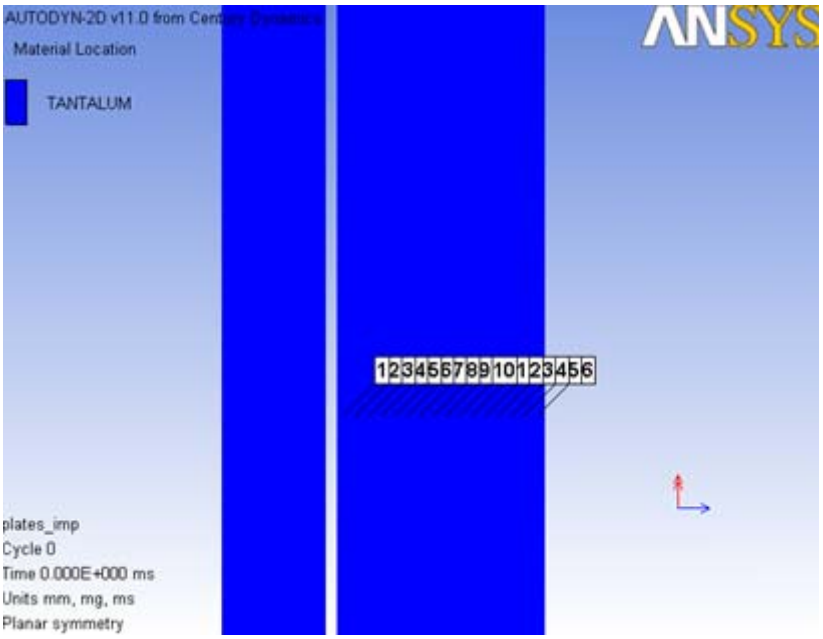


Figure 10. Autodyn® Problem Set Up Of Tantalum Flyer Plate Impact

Two square plates (2 mm and 4 mm thicknesses with a height of 300mm) were generated using Autodyn® in planar symmetry with one plate (of a greater thickness) being stationary, and the flyer plate having an impact velocity of 1.0km/s. The mesh set up had a density of 2 cells/mm. The material properties, pulled from Autodyn® library, for Tantalum are shown in Table 6. :

Table 6. Material Properties of Tantalum

EOS	SHOCK
Ref Density	16.69 gm/cc
Gruneisen Coeff	1.67
C1	3.41 km/s
S1	1.20
Quadratic S2	0
Ve/Vo	0
Vb/Vo	0
C2	0
S2	0
Ref Temp.	300 K
Specific Ht	135 J/kgK
Thermal Conductivity	0 J/mKs

Strength	SteinBerg Guinan
Shear Modulus, G	69 GPa
Yield Stress	0.77 GPa
Max Yield Stress	1.1 GPa
Hardening Const	1
Hardening Expnt	0.1
dG/dP	1.001
dG/dT	-8970 kPa
dY/dP	0.01117
Melting Temp	4340 K

Failure	Hydro (Pmin)
Hydro Tensile Limit	-2.0 GPa
Reheal	Yes
Crack Softening	No
Stochastic Failure	No
Erosion	Geometric Strain
Erosion Strain	2.0
Type	Instantaneous

Figure 11. shows the planar shock wave propagation at an arbitrary time of 0.44μs and the pressure-time profile for the Target Plate with a peak pressure of 33.36 GPa.

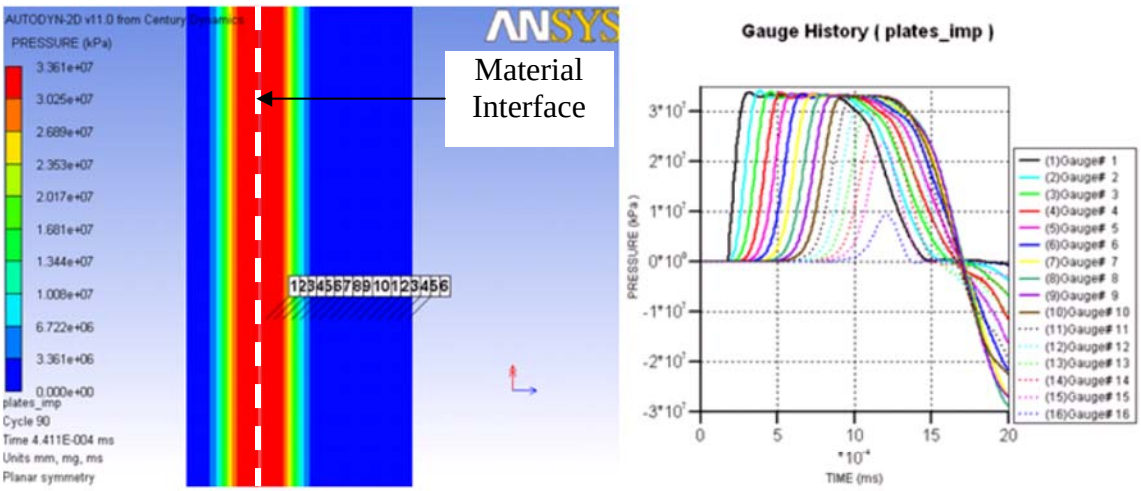


Figure 11. Shock Pressure Profile of the Ta-Ta Plate Impact (Impact velocity was 1000m/s)

Hand Calculations were done to verify the Autodyn® results and the shock jump conditions used are documented as follows:

The Hugoniot of Tantalum is:

Us = 3.43 + 1.19 Up

For a flyer plate velocity 1 km/s, symmetric impact, the particle velocity, Up, is simply 0.5 km/s. This gives the Us as 4.025 km/s.

Hence, P = ρo Us Up = 16.56 (gm/cc) x 0.5 (km/s) x 4.025 (km/s)= 33.33 GPa (a result that is very close to Autodyn's®). The existence of negative pressure as shown in the pressure gauge plots are also verified by hand calculation to be caused by the interaction of release waves from the target free surface and from the back of the flyer plate. This verifies the hydrodynamic code used by Autodyn®.

a. Shock Wave Profile

As can be seen in Figure 11. , the shock wave profile shows notable perturbations (small peaks) at the peak pressure region, and although it shows a relatively flat top, these small peaks are caused by a deliberate addition of artificial viscosity to the hydrocode. Artificial viscosity was discovered by von Neumann and Richtmyer [18] who added this concept to the pressure in order to smear out the shock wave over several mesh widths. The concept of a solid having a viscous effect may seem difficult to grasp initially however, this eliminates the discontinuities (jump conditions) associated with shock waves in order to allow the code (both Eulerian and Lagrangian) to handle steep stress gradients, as opposed to mathematical discontinuities. Although the "jump" is now approximated by a very steep stress gradient, this slightly "distorted" solution has two properties: (1) the solution is only locally affected at the shock front, and away from the shock front, this artificial viscosity no longer affects the calculation, and (2) the accuracy of the calculation is preserved.

b. Lagrangian vs. Eulerian Code

In Autodyn® Version 11/12, it is not possible to model an orthotropic material under the Eulerian frame of reference. Hence, even though high velocity impact simulations typically favor the Eulerian frame over the Lagrangian frame due to large distortions of the mesh, as well as an infinitesimal time step, we are limited to using the Lagrangian code. The drawbacks of using the Lagrangian code are mitigated by good control of the erosion criteria, and a faster calculation cycle time.

c. Erosion

It is important that the concept of erosion be documented early in the simulation process because it has a direct impact on the visual representation of the physical damage that occurs. In the Lagrangian mesh, the mesh tends to distort with the material as it is subjected to stresses. As the time step is dependent on the smallest side of the mesh, the time step can become infinitesimally small to make calculations overly time intensive, slow, or impossible. Distortion can also cause a volume inversion (negative volume) of the mesh elements, thus resulting in an invalid calculation. In Autodyn®, the

concept of erosion is invoked, and elements are conveniently “deleted” once they have reached a user-specified instantaneous geometric strain. However, this method of “bookkeeping,” though conserves the mass and momentum exactly, loses track of the internal energies of failed (and hence deleted) elements. In general, throughout this investigation, the erosion criteria has been set to 2.0 (200%) of the geometric strain. Where appropriate, it may be set to 1.0 (100%) to better represent graphically the damage observed in brittle materials such as ceramics.

d. Mesh Sensitivity

The same model (Ta-Ta plate impact) was set up, but this time with a higher mesh density of 4 cell/mm. The objective of this exercise was to check the sensitivity between the numerical results and mesh density. It was found that when the mesh density was doubled from 2 cells/mm to 4 cells/mm the pressure profiles obtained from the simulations were numerically identical i.e., the peak pressures and time-axis intercept were the same. However, computational time was significantly increased.

A lower mesh density, subjected to a limit, has obvious advantages in terms of calculation time. However, it is not justifiable if this affects the accuracy of the calculation, resulting in meaningless results. For high velocity impacts, Zukas [19] has shown that a 6 cell/cm mesh density for an impact velocity of 1103m/s is adequate to generate results within 3% of the residual velocity in that particular model set up. Increasing the mesh density improved the accuracy marginally (to within 1.5%), but increased the computational costs significantly. Zukas and Kimsey [20] has also shown that doubling the mesh density in 2D simulations increased the computational time by 8 times for explicit methods, of which Autodyn® is based upon. In view of the above findings, the mesh density in this research shall not be less than 2 cells/mm (equivalent to 20 cells/cm) in order to obtain accurate results within reasonable computational times in our simulations.

2. W-Ta Impact

As another exercise, a Tungsten projectile was made to impact upon a

Tantalum target plate. The Tantalum properties were as before, whilst the Tungsten library properties provided by Autodyn® are shown in Table 7. .

Table 7. Material Properties of Tungsten

EOS	SHOCK	Strength	SteinBerg Guinan	Failure	Hydro (Pmin)
Ref Density	19.30 gm/cc	Shear Modulus, G	160 GPa	Hydro Tensile Limit	-2.0 GPa
Gruneisen Coeff	1.67	Yield Stress	2.2 GPa	Reheal	Yes
C1	4.03 km/s	Max Yield Stress	4 GPa	Crack Softening	No
S1	1.237	Hardening Const	7.7	Stochastic Failure	No
Quadratic S2	0	Hardening Expnt	0.13	Erosion	Geometric Strain
Ve/Vo	0	dG/dP	1.501	Erosion Strain	2.0
Vb/Vo	0	dG/dT	-22,080 kPa	Type	Instantaneous
C2	0	dY/dP	0.02064		
S2	0	Melting Temp	4520 K		
Ref Temp.	300 K				
Specific Ht	129 J/kgK				
Thermal Conductivity	0 J/mKs				

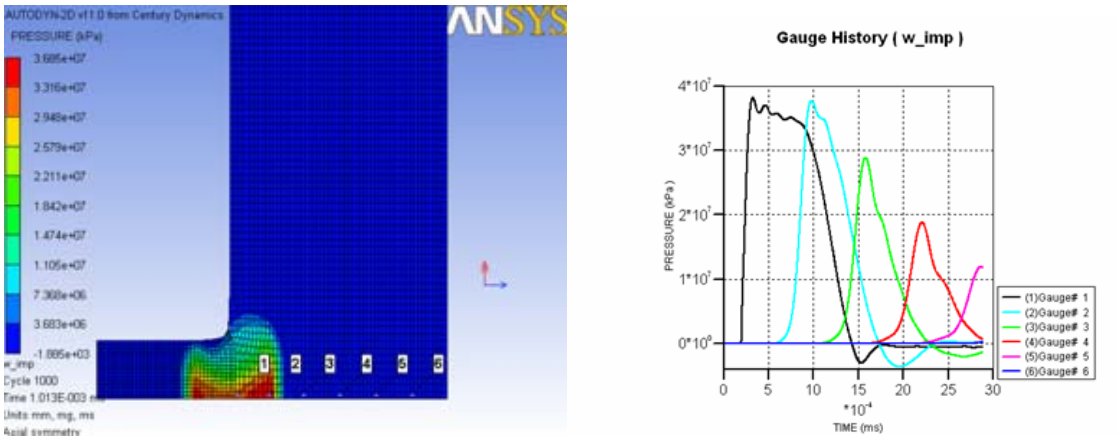


Figure 12. Shock Pressure Profile of the W-Ta Plate Impact (Impact velocity was 1000m/s)

Figure 12. shows the problem set up. A very large and flat plate (16mm x 300mm) of axial symmetry is used. The cylindrical projectile is made of Tungsten with a

15mm length and 8mm diameter.

Referring to the Pressure-Time history for the impact scenario, a triangular shock wave is quickly obtained in the target instead of the usual flat top shock wave for flat plate impacts. This is not unexpected due to the small projectile which does not hold off edge releases for a very long time. The peak pressure can be shown to be consistent with hand-calculations.

Given Tungsten,

$\rho o = 19.235$ gm/cm3

$Us = 4.04+1.23Up$

And Tantalum,

$\rho o=16.656$ gm/cm3

$Us =3.43+1.19Up$

UD = 1000m/s = 1km/s (impact velocity)

Using

($s1=1.23$, $s2=1.19$, $c1=4.04$, $c2=3.43$, $\rho1=19.235$, $\rho2=16.656$)

And doing impedance matching,

$(\rho1s1-\rho2s2)\, up22 – (2\rho1s1Ud+\rho1c1+\rho2c2)up2 +\rho1(s1Ud2 +c1Ud) = 0$

Up2 = 0.56317km/s

$P2 = \rho2(s2Up2+c2)Up2 = 38.46$ GPa

Checking,

$P1 = \rho1(s1(Ud-Up2)+c1)(Ud-Up2) = 38.46$ GPa (ok)

From Autodyn® Output, a peak pressure of 38.1 GPa was obtained. This is in good agreement with the results from manual calculations. The Autodyn® stress is expected to be slightly lower due to the “artificial viscosity” which causes slight attenuation of the stress wave. The pressure profile is seen to become negative at about t

= 1.5μs. The result of the negative pressure is primarily due to the wave interaction between the release waves from the back surface of the Tantalum target meeting the transmitted release waves from the Tungsten projectile which has a higher impedance. These waves traveling in opposing directions causes a negation of pressure where they meet. Autodyn® keeps track of this complicated sequence of wave interactions in each iteration.

B. CERAMIC–CERAMIC IMPACT

Once the material models have been defined in the Chapter II, it was necessary to do some basic flyer plate simulations to check that the user-defined model was working correctly. The material parameters used in the Ceramic-Ceramic flyer plate impact were as defined earlier. A peak interfacial pressure of 15.2 GPa was obtained with an impact velocity of 1km/s.

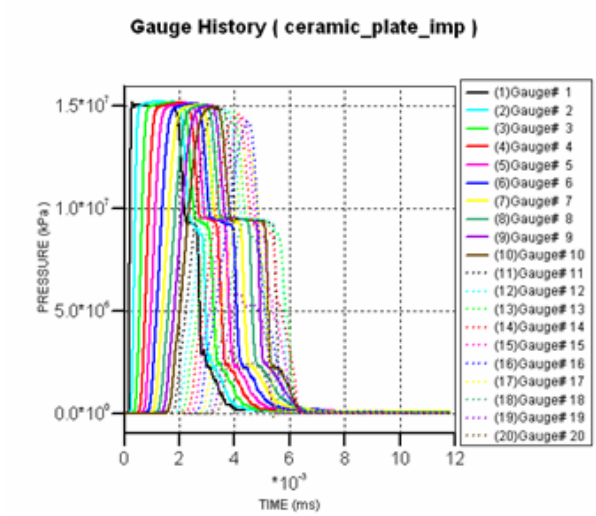


Figure 13. Pressure Profile of Ceramic-Ceramic Flyer Plate Impact at 1000m/s

The shock pressures as illustrated in Figure 13. look credible enough due to the presence of a stable shock wave (flat top) and reasonable shock pressures. The secondary flat top as shown is due to the reflected release wave from the flyer plate.

C. D1-D1 IMPACT

A similar numerical simulation was done to investigate the inherent properties

in the D-1 material. Figure 14. shows the problem setup, and the planar wave generated upon impact. Again, the results were credible, and a flat top shock wave is obtained, as shown in Figure 15.

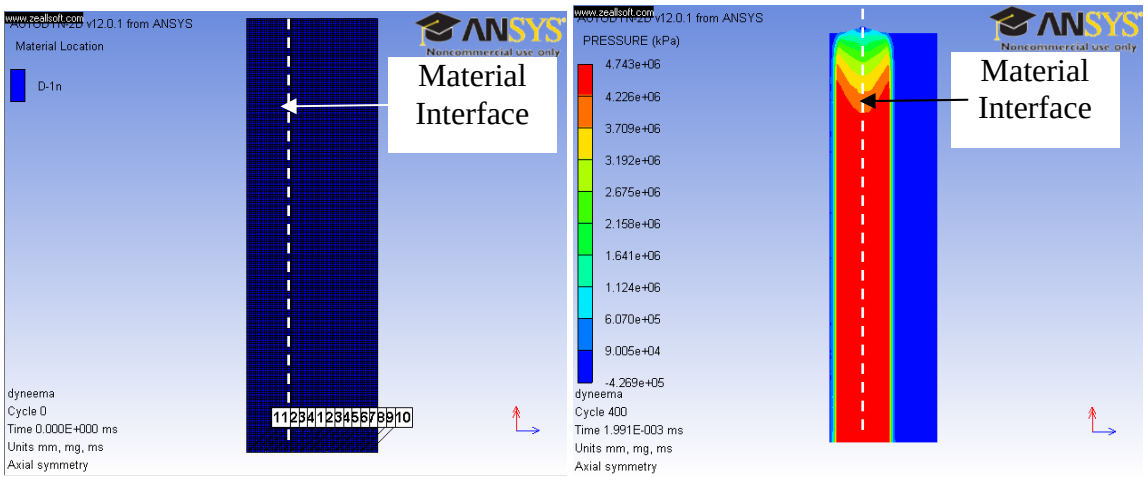


Figure 14. Symmetric Plate Impact of D1 Material at 1 km/s. Plates were 200mm Cylindrical Plates of 5 mm and 10 mm Thickness Respectively. (Left) Problem Setup. (Right) Planar Wave Propagation at 2μs after Impact.

A peak pressure of about 1.75 GPa was obtained from this study, compared to 15.2 GPa for the ceramic material. This is an indication of the lower impedance of the D1 material that is being modeled. Again, the negative pressures being shown in Figure 15. are due to the opposing wave interactions between the release waves coming from the back surface of the target plate, interacting with transmitted release waves from the flyer plate.

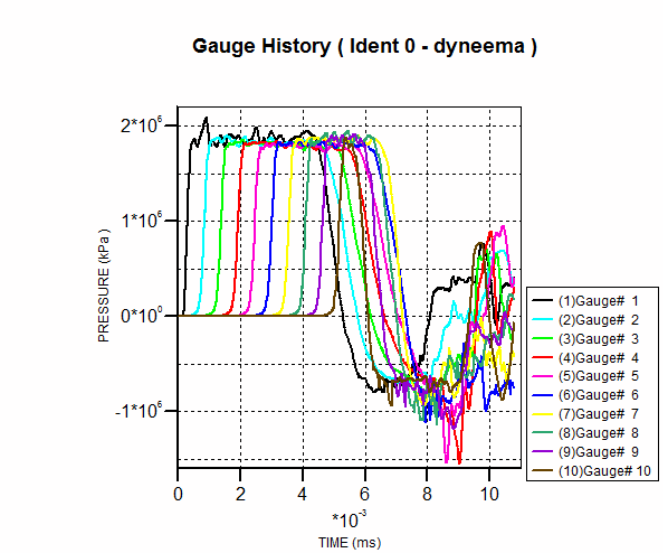


Figure 15. Gauge History of D1 Material Subjected to a Flyer Impact of the Same Material at 1km/s

1. Shock Wave Properties of D-1

In order to investigate the shock propagation properties of D1, the following was set up. A D1 bullet of 10 mm thickness and 40 mm diameter is impacted against a large D1 target plate of 20 mm thickness and 200 mm diameter at 1 km/s. The shock front is tracked via gauges placed in the 11- and 22- directions. As can be seen in Figure 16. , the *lateral* wave speed of the shock front is seen to be faster than the *through-thickness* wave speed. Figure 17. shows the overall pressure profile in the 11-direction.

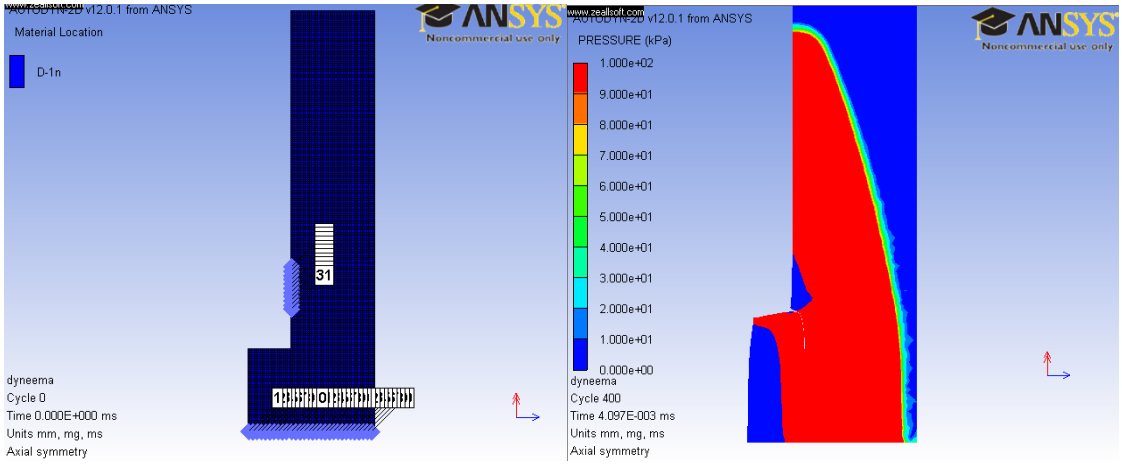


Figure 16. Set up of a D1-D1 Symmetric Impact of a Bullet on a Larger Target Plate. (Left) Gages are setup in the 11- and 22-directions. (Right) Lateral wave speed is seen to be faster than the through thickness wave speed as exhibited by the shock front.

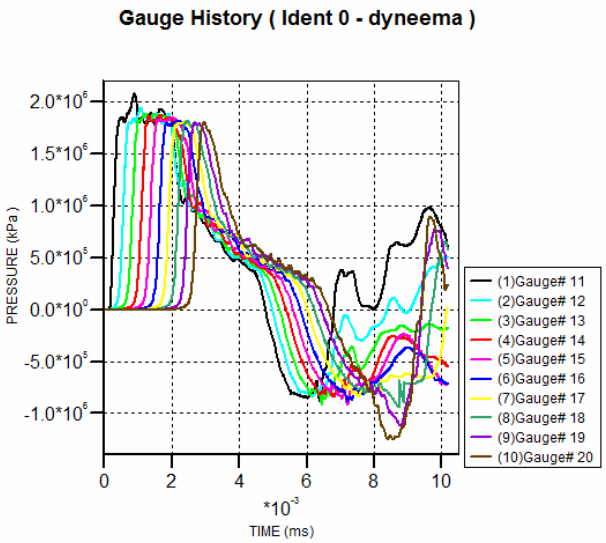


Figure 17. Overall Shock Wave Profile in the 11-direction

To investigate the results of our input parameters, the gauge histories which track the rise times of the pressures at discrete points in the target were analyzed in greater detail. Of greater interest to this investigation were the rise times of the individual gauges. These times were used to determine the speed of the shock wave propagation. Figure 18. shows a close up view of rise times of each gauge spaced 1mm apart. The observed 11-direction shock velocity was 3.70 km/s. This shock velocity is above the longitudinal sound speed of 2.0 km/s due to the higher stress state that the material is subjected to

at this impact velocity of 1 km/s. The lateral shock speed was **11.76 km/s** which, as expected, is very close to the design sound speed of 12km/s.

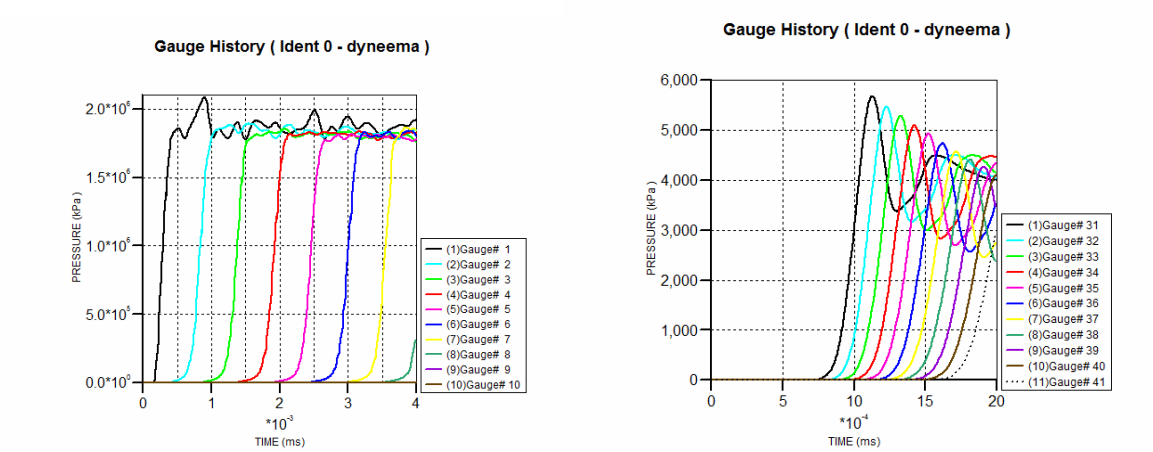


Figure 18. (Left) Rise Times of the Shock Wave Propagating in the 11-direction. (Right) Rise Times of the Shock Wave Propagating in the 22/33-directions

A similar simulation test set up with the impact direction set in the 22-direction was done to investigate the shock properties in the 22/33- directions. Figure 19. illustrates the test set up and results of the simulations.

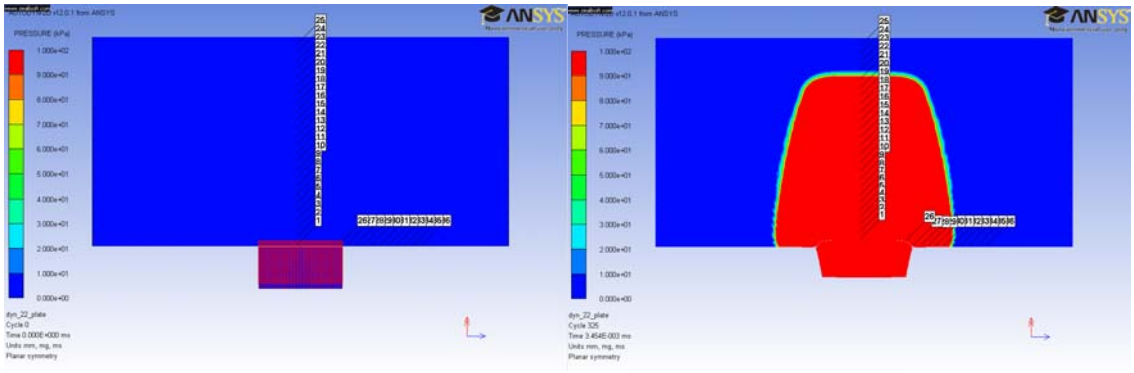


Figure 19. (Left) Impact of Flyer Plate onto D1 in the 22-direction. (Right)Wave Propagation Remains Faster in the 22- direction Compared to the 11-direction.

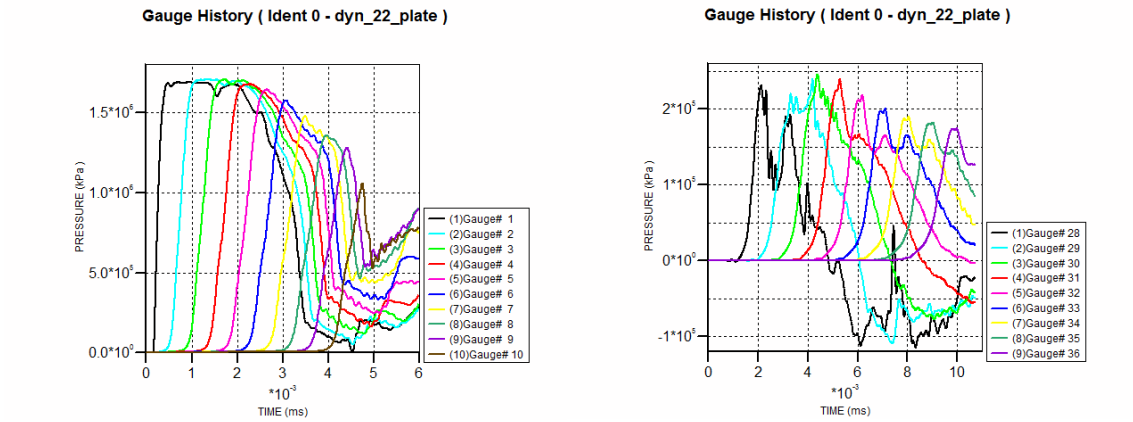


Figure 20. (Left) Shock Profile in the 22-direction. (Right) Shock Profile in the 11-direction.

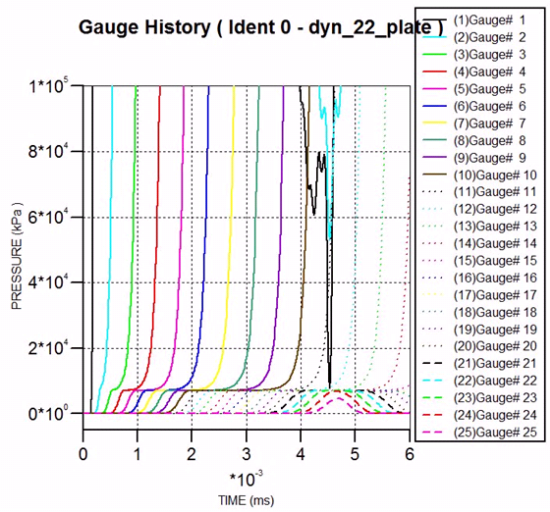


Figure 21. Elastic Wave Moving Ahead of Plastic Wave in the 22-direction.

Figure 20. shows a peak pressure of 1.705 GPa obtained in the 22-direction, close to the previous result of 1.75 GPa. In the 11-direction, the shock velocity was **2.16 km/s**, a value very close to the design wave speed of 2.0 km/s. Careful analysis of the shock profile in the 22-direction of Figure 20 revealed a 2-wave structure comprising of a faster elastic wave being trailed by a slower plastic wave. This is shown in Figure 21. This 2- wave structure had a plastic wave speed of 4.3km/s and an elastic wave speed of 11.7km/s. An explanation of this phenomenon is given in Figure 22.

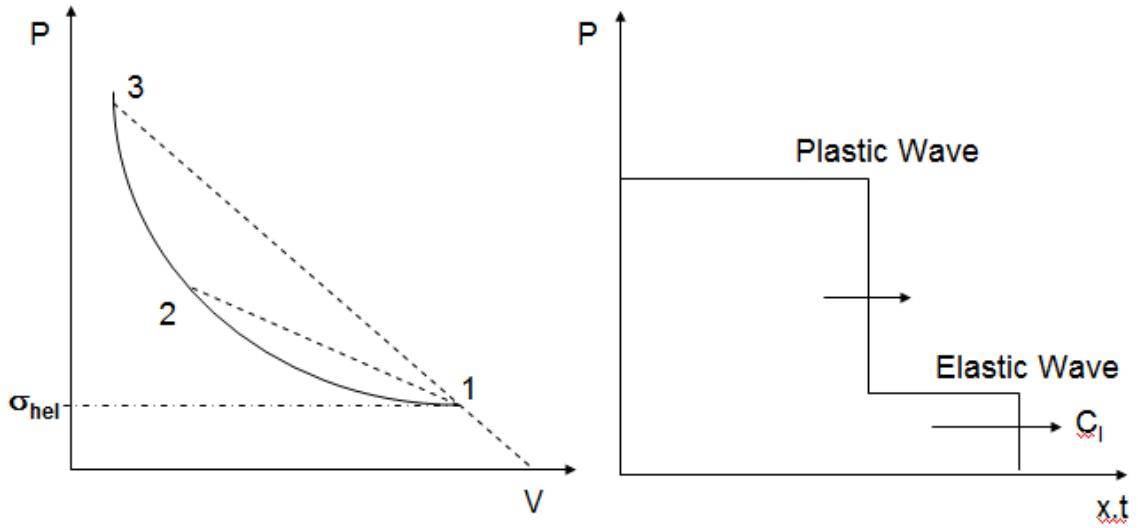


Figure 22. Explanation of the Difference between the Elastic and Plastic Wave Speed. (From [21])

Figure 22 shows an elastic wave moving ahead of the plastic wave. The reason for this 2-wave structure is because the impact velocity was not enough to drive the material beyond its Hugoniot Elastic Limit, σhel, to Material State 3. Instead, the shock wave drives the material to State 1 (σhel), causing the elastic wave to form, before going to State 2 which sees the formation of the slower plastic wave. Increasing the impact velocity (and hence shock pressure) should see the gradual disappearance of the elastic wave as it is overdriven by the plastic wave. The result of this increase in impact velocity is shown in Figure 23.

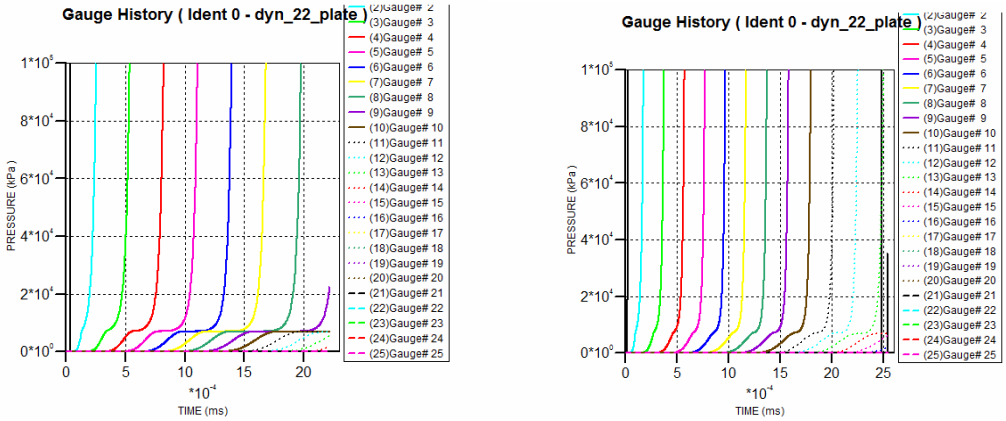


Figure 23. (Left) Plastic Wave at 5km/s Impact Velocity. (Right) Plastic Wave at 10km/s Impact Velocity.

As expected, Figure 23. shows the plastic wave catching up with the elastic wave as the impact velocity is increased from 1km/s to 5km/s and 10km/s respectively. At 10km/s impact velocity, a plastic wave speed of 9.9 km/s was observed, while the elastic wave speed remained at 11.7 km/s. It was found that at 24 km/s impact speed, the elastic wave had completely disappeared, and the plastic wave had overdriven the elastic wave.

2. Us-Up Curve

Even though Autodyn® uses the mass, momentum and energy jump conditions for its calculations, it was desirable to check whether the Us-Up relationship was indeed linear within the velocity range that we are investigating for the D1 material. In order to do this, flyer plate simulations at different flyer plate velocities (10,000, 5,000, 2,000, 1,000, 800, 600, 500, 400 m/s) were used to determine the shock speed, and also the shock pressure upon impact in both 11- and 22/33- directions. As this was a symmetric (same material) impact, the particle speed, Up, is taken to be exactly half that of the flyer plate velocity. Pressure rise time profiles in the 11- and 22/33- directions were analyzed, and the incident shock pressure noted. This information will allow us to obtain the Us-Up curve of the D1 material in the respective directions.

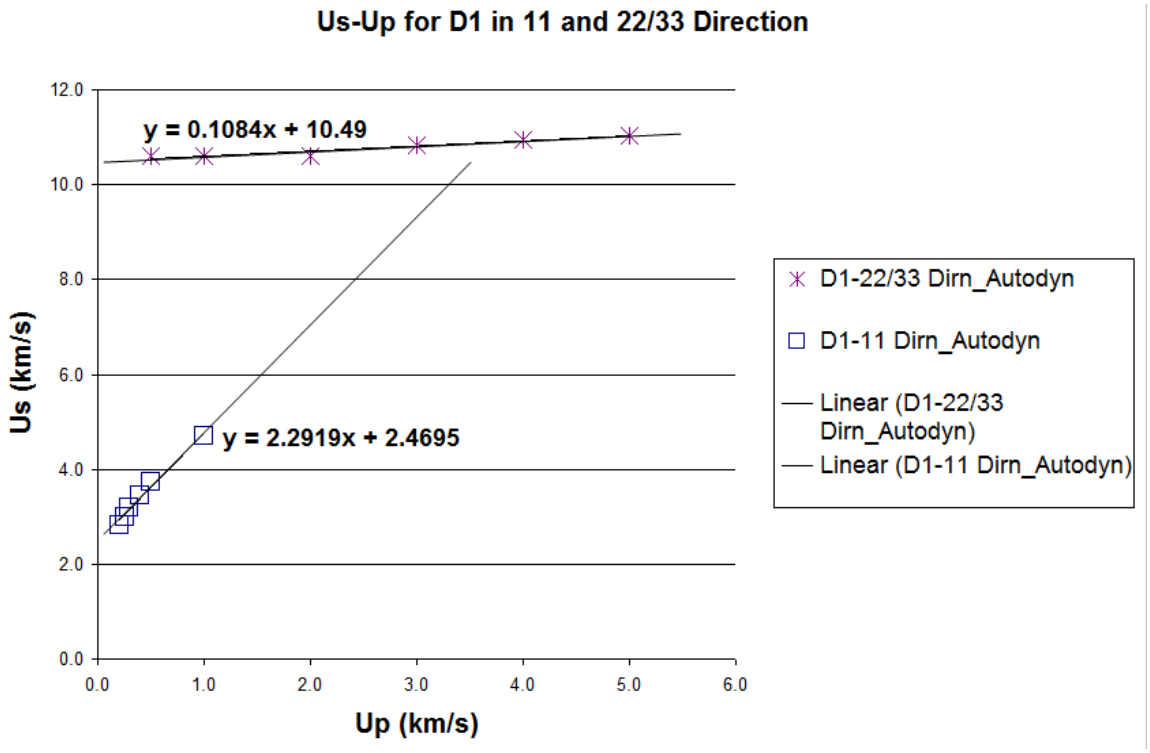


Figure 24. Us-Up relationship of the D1 Material in the 11- and 22/33- directions

As can be seen, the Us-Up relationships are reasonably linear within the 0-2km/s impact velocity in the 11-direction and 1-10km/s impact velocity in the 22/33-direction. Figure 24 reveals some important information about our assumptions that we have made in our material modeling. Based on the Us-intercept, which is close to the Cb, we can work out the Cl and Cs as shown in Table 8, using isotropic relations between Cb and Cl.

Table 8. Comparison of Cb, Cl and Cs between Design Values and Autodyn® Output

22/33 Direction	Cl (km/s)	Cs (km/s)	Cb (km/s)	Remarks
Design Value	12	6	9.8*	cb2 = cl2-(4/3)cs2
Autodyn®	12.85*	6.42*	10.49	cs= (1/2) cl cb2 = (2/3)cl2

11- Direction	Cl (km/s)	Cs (km/s)	Cb (km/s)	Remarks
Design Value	2	1	1.63*	cb2 = cl2-(4/3)cs2
Autodyn®	3.03*	1.52*	2.47	cs= (1/2) cl cb2 = (2/3)cl2

**: Calculated Values using the given formulae.*

It can be seen from Table 8 that the observed bulk sound speeds observed in Autodyn® is *slightly different* from the theoretical calculations. The same can be said of the longitudinal and shear sound speeds. These slight deviations are not unexpected because of the simple cb, cl and cs relationships which were derived based on isotropic materials, and are therefore not *directly* applicable in deriving the actual values for an orthotropic material. Nevertheless, they give a quick and simple estimation of the actual values, and it is clear from Table 8, that we are not very far off in our estimations. Interestingly, it is worthwhile to note that based on the effective bulk modulus calculated to be K' = 42.6118 GPa, the *effective* (average) c'b = SQRT(K'/ρ) = 6.53 km/s. A value that is somewhere in between the cb in the 11- and 22/33- directions. However, as we are dealing with an orthotropic material which has different behaviors in different principle directions, we would expect the bulk sound speeds to be different in different directions.

These results in Figure 24 and Table 8 were pretty encouraging as the respective wave speeds were approximately in the correct order of magnitude that it was designed for (i.e. 2km/s and 12 km/s, using the transverse isotropic assumption to model D1). This would allow us to proceed to investigate D1 further for ballistic applications.

D. COMPOSITE PLATE SIMULATION

Having completed the basic simulation which illustrated the basic mechanical properties of the material models that are being used, a composite plate was created to investigate the combined properties of a very hard technical ceramic as a 1st layer and D1 as the 2nd layer.

The results of the simulation are as shown in Figures 25 and 26:

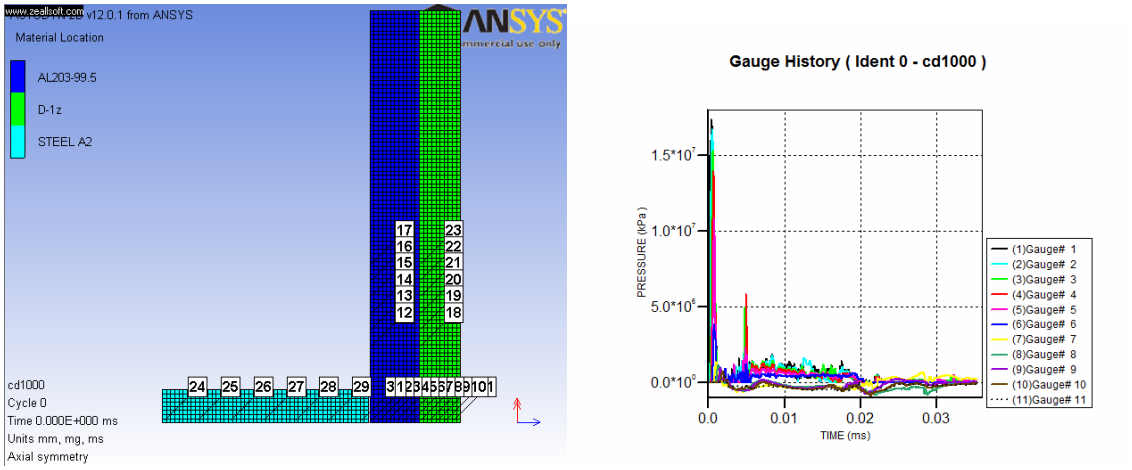


Figure 25. Autodyn® Simulation of an A2 Steel Cylinder Bullet Impacting at 1000m/s onto a Ceramic-D1 Composite Plate. ***(Left) Problem setup. (Right) Overall Pressure-Time profile.***

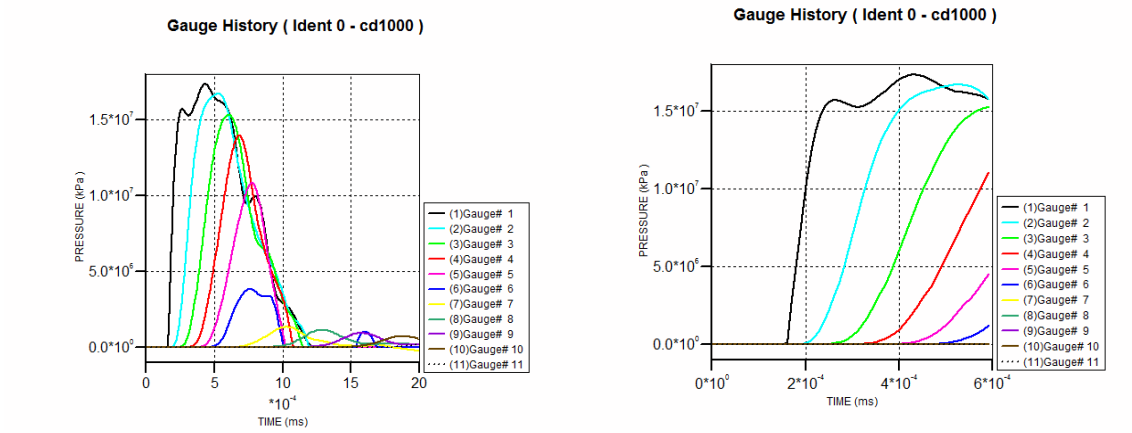


Figure 26. Ceramic Material Results. 17.3 GPa Peak Pressure is Observed, with a 3.45km/s Shock Velocity in the 11-direction

The pressure profile obtained from the impact simulation on the composite plate is shown in Figure 26. A peak pressure of about 17.3 GPa is obtained in the ceramic. Gauges embedded in the D1 material show significantly lower peak pressures (shown by gauges 7-11) due to the much lower impedance of this material and its high transverse wave spreading properties.

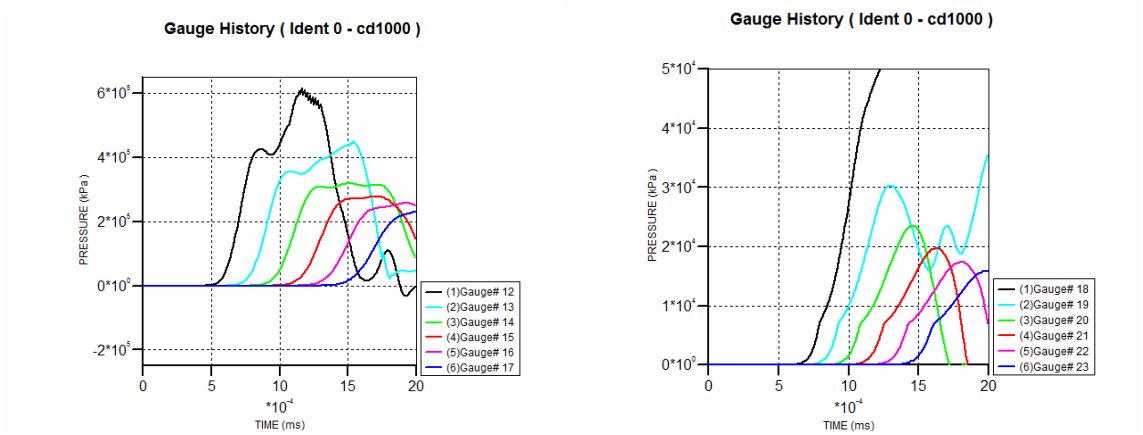


Figure 27. (Left) Ceramic Shock Profile in the 22/33-direction. (Right) D1 Shock Profile in the 22/33-direction.

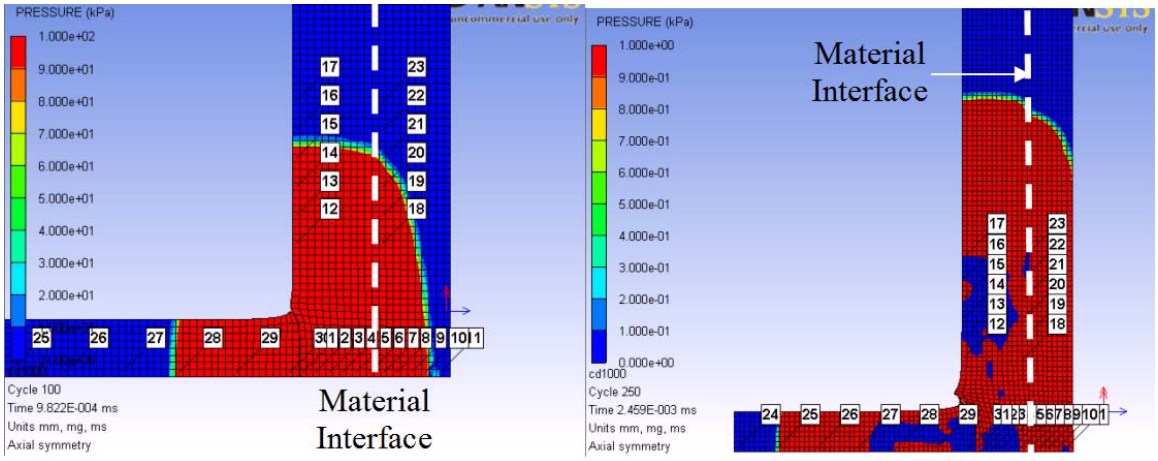


Figure 28. Shock Wave Propagation is Slowed Down in the 11-direction Due to the Presence of the D1 Material

Figure 27. shows the shock wave profiles in the 22/33 directions. Looking at the shock front propagation, it is seen that the transverse isotropic behavior modifies the way the shock front propagates through the material. The shock wave at the interface between ceramic and D1 is slowed down from propagating in the 11-direction. However, it is observed that the lateral shockwave in the D1 material does not outrun that of the ceramic because of the following relationships:

Ceramic:

Density, ρ = 3.89 gm/cc

Bulk Modulus, K = 231 GPa

Shear Modulus, G = 152 GPa

Longitudinal Modulus, F = K+(4/3)G = 433.67 GPa

Longitudinal Soundspeed = SQRT(F/ρ) = 10.56 km/s in all 11-22-33 directions

D1:

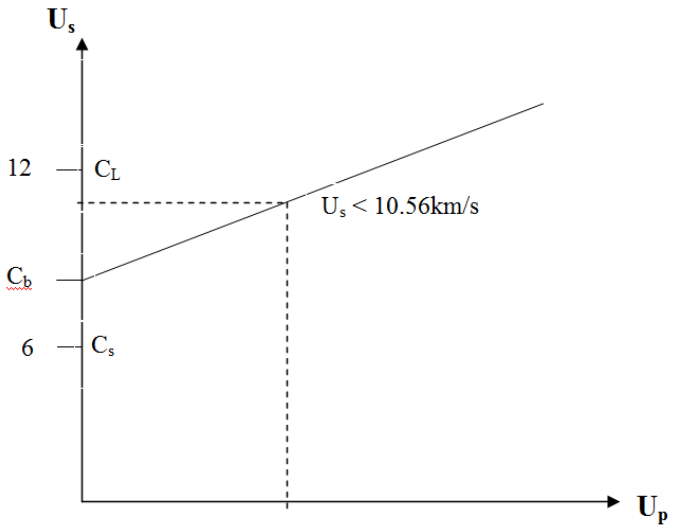


Figure 29. Possible Us-Up Relationship in the 22/33-Direction for D1 Material. (Not to Scale)

A possible Us-Up relationship for the D1 material in the 22/33 direction is shown in Figure 29. Figure 26. showed the significantly low pressures of about 1.5 GPa in the D1 material when the composite plate was impacted with the steel projectile. This lower pressure exhibited might be an indication that the shock speed, Us, in the D1 material had not gone beyond the design longitudinal wave speed of 12km/s and is also less than the Us of the ceramic (shown by dotted line in Figure 29), thus allowing the shock wave in the Ceramic material to outrun that in the D1 material.

Nevertheless, it is clear from these simulations that the shock wave is slowed

down significantly in its propagation in the 11-direction, while the shock wave propagates rapidly in the other two directions (22 and 33).

The above section concludes the preliminary theoretical modeling of the new orthotropic material which this study seeks to better define. In order to test the validity of the computer simulations, a live firing experiment is planned to test the simulated material models against the real test target samples.

THIS PAGE INTENTIONALLY LEFT BLANK

IV. LIVE FIRING VALIDATION

A. TEST DESIGN

In order to validate the potential benefits of the layering concept as described during the introductory paragraphs, and the preliminary investigation into the properties of each layer, it is appropriate to conduct a live firing experiment. A test matrix was defined in order to minimize the efforts for the test (due to time and budget constraints) and maximize the outcome and conclusions. Table 9 shows the test matrix.

Table 9. Test Matrix

Test Sample	Material	Total Thickness	Average Density (gm/cc)	Areal Density [gm/cm2] (Density x Thickness)	Purpose
1.	Dyneema HB25	5mm	0.97	0.485	Ballistic Resistance of Dyneema HB25 on its own
2.	Dyneema HB25 +P2 +Al plate	11.5mm	0.91	1.05	Effectiveness of a PU Foam.
3.	AISI 4140 Steel	4.76mm	7.85	3.737	Baseline comparison of armor plates
4.	Ceramic + Dyneema HB25	11mm	2.52	2.771	Basic composite plate to replace armor steel
5.	Ceramic + Dyneema HB25 + P2 + Al plate	17.5mm	1.91	3.336	Effectiveness of a PU Foam.
6.	Ceramic + Dyneema HB25 + P1 + Al plate	17.5mm	1.86	3.256	Comparison of P2 and P1

Material Notes:
All target plates were 100mm x 100mm
6mm thick ceramic plates from Industrie Botossi were used.
5mm thick Dyneema HB25 from DSM
5mm thick Polyurethane, P2 (Density 0.32 gm/cc)
5mm thick Polyurethane, P1 (Density 0.16 gm/cc)
1.5mm Thick aluminum 6061 as an inertial backing plate for the porous foam.
4.76mm thick AISI 4140 Steel Plate as a control sample

AISI 4140 steel of yield strength 655 MPa was used as a baseline to compare the performance of the composite layered armor plate. It is estimated that commercially available armor steel has similar performance characteristics as AISI 4140, even though

most armor steels are proprietary materials whose yield strength, construction and additives are not available in open literature. Actual Material Properties are as shown in Table 10.

Table 10. Types of Materials Used in Experiment.

Material	**Description**
AISI 4140 Steel (from McMaster-Carr)	Precision ground in accordance to ASTM A322, Rockwell C30, with a yield strength of 95,000 psi (655 Mpa)
Ceramic (Corbit 98 from Botossi)	Alumina 98% with a Young's Modulus of 384 GPa, and hardness H of 16.3 GPa, and Density of 3.81 gm/cc
Dyneema **HB25**	Density 0.97 gm/cc and fiber tensile strength of approximately 2 GPa
Porous Foam 1	Made of Polyurethane of density 0.16 gm/cc PR 6710
Porous Foam 2	Made of Polyurethane of density 0.32 gm/cc PR 6720
Aluminum 6061T	Inertial Backing Plate, of density 2.703 gm/cc to support the foam

A variety of projectiles were used in this experiment and their properties are as shown below in Table 11.

Table 11. Properties of steel projectiles used.

Specification/ Shape	**Dimension**	**Density (gm/cc)**	**Hardness**	**Yield Strength**
E52100/ Sphere	9/32"	7.75	Rockwell C 60-67	295, 000 psi 2.0 GPa
SS304/ Sphere	0.299"	7.89	RHB - 88	205 MPa
AISI A2/ Cylinder	½", 0.295" dia	7.75	RHC – 53-60	1.8 GPa
AISI A2/ Cylinder	¾", 0.295" dia	7.75	RHC – 53-60	1.8 GPa
AISI A2/ Cylinder	1", 0.295" dia	7.75	RHC – 55-56	1.8 GPa

Steel Spheres were from McMaster. AISI A2 Cylinders were from UCSB, manufactured in-house.



Figure 30. A2 Tool Steel Cylinder Projectile that was Used in the Experiment. (Rockwell Hardness C 55-56. Yield Strength of 1.8 GPa)

B. CONSTRUCTION OF TARGET SAMPLES

A low viscosity 2-part epoxy (Angstrom Bond®) from Fiber Optic Centre Inc was used to provide a very thin bond between the surfaces of the samples. This is to allow a smooth transmission of shock waves from one material to another. The presence of a significant thickness of adhesive will affect the experimental results due to the introduction of a lower impedance layer. This is minimized through careful construction, and strict choice of adhesive.

This Angstrom Bond® AB9110LV glue has a viscosity rating of only 500 cps at 25°C which is comparable to motor oil SAE40. Water has a viscosity of 1 cps. Its low viscosity will allow the escape of trapped air pockets between the layers during the application of compressive pressure over 24hrs to allow curing, hardening and development of bond strength.

Table 12. Specifications of Anstrom Bond® Epoxy AB9110LV from Fiber Optic Center Inc.

Properties		**Properties**	
Color	*Clear/ Yellowish*	Operating Temperature	*-270℃ – 125 ℃*
Mixed Viscosity @ 25°C	*500 cps*	Mixing Ratio (resin/ hardener)	*100/30*
Specific Gravity	*1.15*	Working Time	*1hr*
Tensile Strength	*7200 psi*	Curing @ 25°C	*18hrs*

Careful formulation, mixing and application of this adhesive minimizes the amount of trapped air bubbles between the surfaces. The surfaces were cleaned with a non-alcohol based cleaning agent, air dried for 1 hour, and the epoxy was applied on one side of the sample. Subsequently, the next layer was placed over the base layer, and held in a clamping vice over 24hrs for curing and hardening.

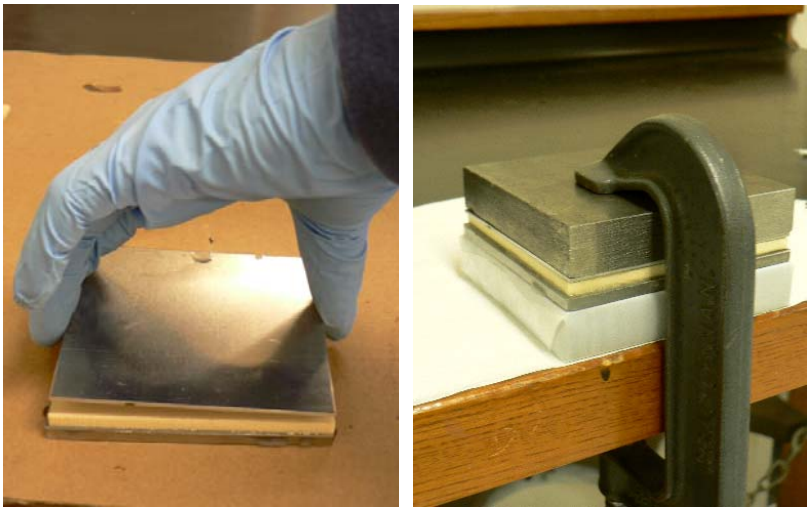


Figure 31. Photos Illustrating the Placement Process as well as the Application of Uniform Pressure over the Sample Using Top and Bottom 20mm Mild Steel Plates

C. EXPERIMENTAL SET UP

The live firing experiment was conducted at a helium pressure gun facility at University of California, Santa Barbara (UCSB). With a gas gun pressure of up to 2000 psi, the gun has a maximum projectile velocity of about 760 m/s based on the mass of a 0.3 inch diameter steel ball. The velocity decreases as the projectile mass is increased. 1-inch long steel cylinders of the same diameter had an average velocity of about 475 m/s. Figure 32. Figure 34. illustrate the experimental set up.

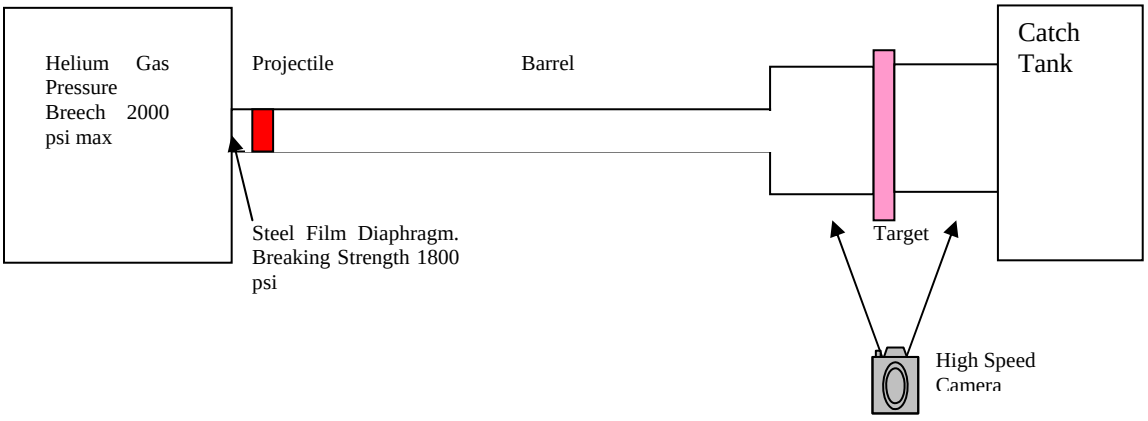


Figure 32. Schematic of the Gas Gun Facility

The breech is pressurized to begin the firing sequence. Once the diaphragm pressure has reached about 1800 psi, the diaphragm breaks, and the helium gas pushes the projectile towards the target. The target is held up by an impact chamber that contains protective bulletproof windows. The projectile passes through a break wire and triggers the camera flash as well as a high-speed camera. The IMACON 200 high-speed camera captures the images at up to 200 million fps. Through imaging software, the velocity of the projectile can be estimated to within 1% accuracy.



Figure 33. Photo Showing (a) the Gas Pressure Breech, (b) the entire length of the barrel and (c) the Impact Chamber/ Bullet Catcher

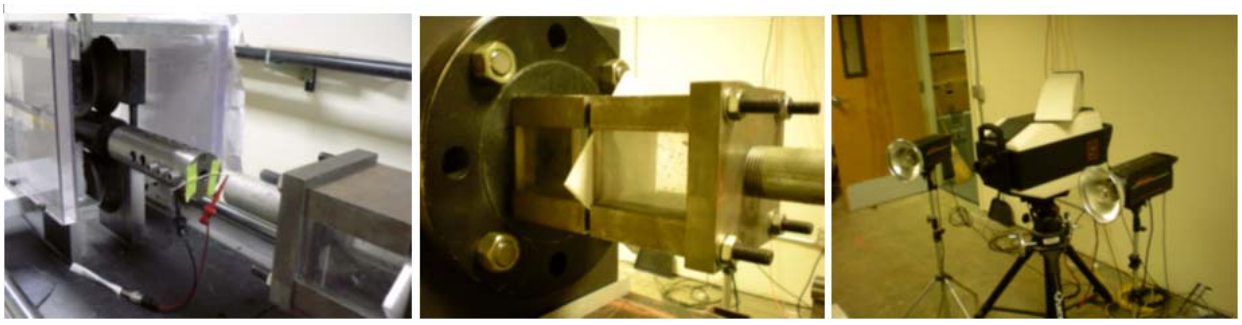


Figure 34. Photo Showing (a) the Break Wire Connection, (b) the Impact Chamber, and (c) the High speed Camera Setup

D. LIVE FIRING

1. Dyneema HB25

The experiments started with the testing of the Dyneema HB25 100mm x 100mm samples to validate the performance of Dyneema HB25 on its own, and as a baseline from which the composite plate is built upon. A test was also done using Dyneema with an unsupported foam backing to see if the foam provided additional penetration resistance.

Table 13. Test Set 1 - Dyneema HB25

Sample/ Projectile Shape	Projectile Matl	Impact Velocity (m/s)	Exit Velocity (m/s)	Penetrate (Y/N)	Volume (mm3)	Mass (gm)	KE (J)
Dyneema HB25 Ball (9/32")	E52100	610	350	Y	190.89	1.479378	275.24
Dyneema HB25+P2*+Al Ball (9/32")	E52100	633	375	Y	190.89	1.479378	296.39

**: P2 as defined in Table 8. Porous Polyurethane Foam of density 0.32 gm/cc*

Figure 35. is a close up view taken with a scanning electron microscope [21]. It clearly shows the 0-90° layout of the individual Dyneema HB25 fibers and the orthogonal 22-33 plane symmetry which was being modeled.

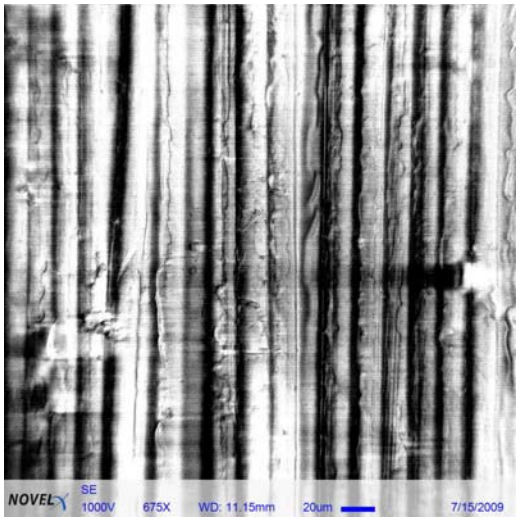


Figure 35. Scanning Electron Microscope Picture of Dyneema HB25, Magnified 675 times. Taken

at SEM Lab, NPS. [21]

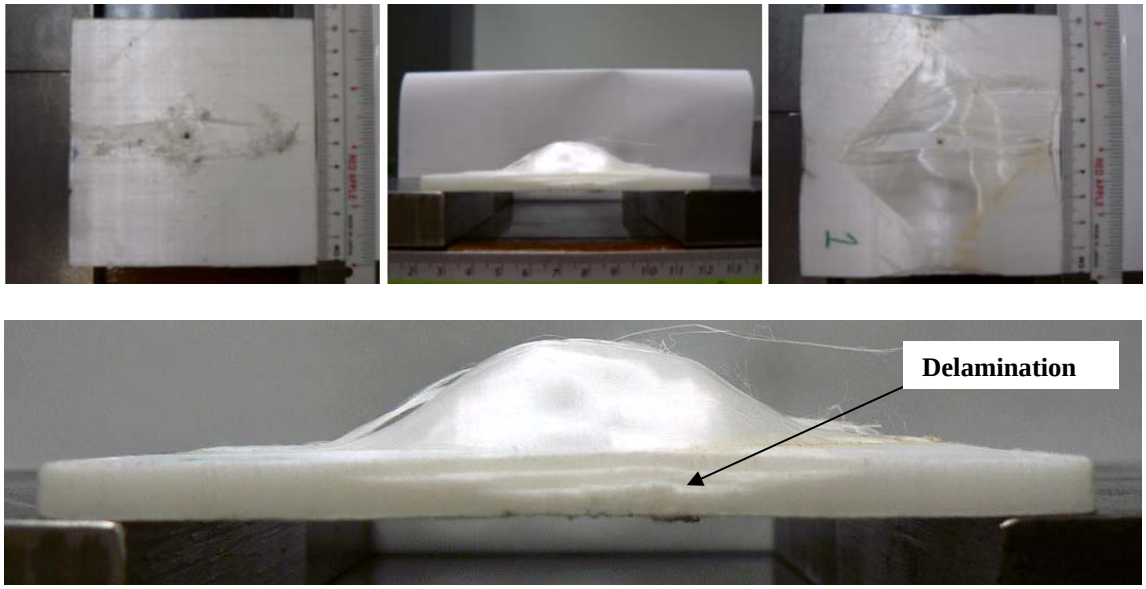


Figure 36. Samples of Dyneema HB25 Showing Full Penetration by an E52100 9/32" Steel Ball.

Figure 36. shows the results of the test sample of the single Dyneema HB 25 target plate. Delamination occurred only on the latter half of the Dyneema HB25 composite. Shear Failure occurred for the initial stages of the impact penetration.

.

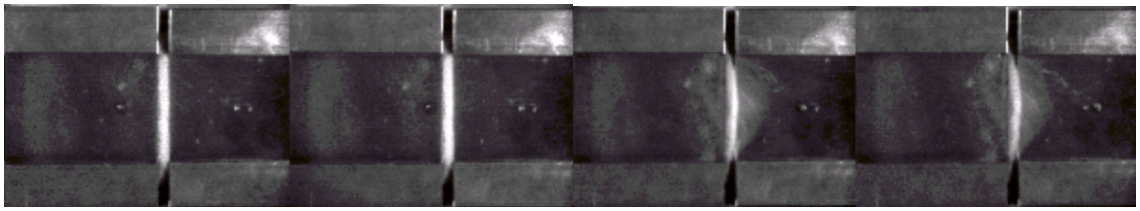


Figure 37. High-speed photos showing Dyneema before and after penetration by steel sphere.

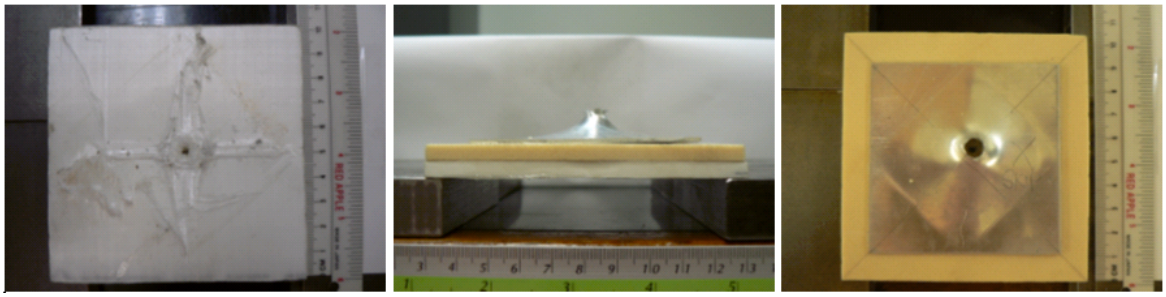


Figure 38. Addition of a Shock Porous Foam in the Rear did not Appear to Help in Resisting Penetration as Can be Seen from the Similar Exit Velocity of the Projectile.

Both samples of the Dyneema HB25 failed to resist the penetration from a E52100 Steel Ball traveling at 610-633 m/s. It is observed that although the Dyneema undergoes delamination in the later part of the impact process, the initial stages of the impact saw the projectile shearing through the material due to its shape and high speed. The breaking of at least half of the fiber thickness rendered at least 50% of the fibers inactive, and thus unable to be used to stretch to help absorb the projectile kinetic energy. This affected greatly the ability of Dyneema to absorb the kinetic energy through the process of elastic/plastic deformation and delamination, allowing the projectile to penetrate.

This initial shearing mechanism was not mitigated by the addition of a porous media to absorb the shock as can be seen from the exit velocities in both cases (Figure 38.). For the Dyneema HB25 alone, the impact velocity was 610m/s and the exit velocity was 350m/s. Thus, the Δv was 260m/s. With the addition of the porous layer and the thin aluminum plate, the impact velocity was 633m/s and the exit velocity was now 375m/s, giving a Δv of 258m/s, which is not significantly different from the earlier case.

From these visual observations of the failure mechanism, it can be concluded that Dyneema HB25 performs poorly when it is subjected to shear forces, and we postulate that its ideal failure mechanism is through a process of fiber stretching, delamination, and plastic deformation which absorbs the kinetic energy of the projectile.

2. Steel AISI 4140

As these experiments were the first we have done so far in our research program, some trials were necessary in order to evaluate the minimum kinetic energy (KE) necessary to penetrate the AISI 4140 steel armor plate. Our initial tests showed that at the maximum velocity possible on this gun with our steel spheres, we were not able to achieve penetration of the AISI 4140 target plate. We therefore switched to rod penetrators and found that a 1” rod with a diameter of 0.295” made of high strength AISI A2 tool steel was required to fully penetrate the target plate. This is summarized below in Table 14.

Table 14. Test Set 2 - Baseline Armor Steel AISI 4140

Projectile Shape	Projectile Matl	Impact Velocity (m/s)	Penetrate (Y/N)	Volume (mm3)	Mass (gm)	KE (J)	Relative Mass Ratio	Relative KE Ratio
Sphere (9/32”)	E52100	658	N	190.89	1.48	320.26	34.02%	41.47%
Sphere (0.299”)	SS304	755	N	220.89	1.71	487.92	39.31%	63.18%
Rod (1/2")	A2	596	N	561.07	4.35	772.30	100.00%	100.00%
Rod (3/4")	A2	500	N	841.60	6.52	815.30	150.00%	105.57%
Rod (1")	A2	484	Y	1122.14	8.70	1018.61	200.00%	131.89%

All Target Samples were made of AISI 4140 (100mm x 100mm) Steel Plates, of yield strength 655MPa. A2 Hardened Tool Steel had a hardness of RHC 53-60, and yield strength of 1.8 GPa.

It can be seen that a rough estimation of the KE that is necessary to penetrate the AISI 4140 armor steel plate was in the region of about 1000 Joules. High-speed photography showed that the rod penetrator was completely shattered and residual velocity of the fragments were about 118m/s. These photos, shown in Figure 41, were taken at 30μs interframe time (33, 333 fps).

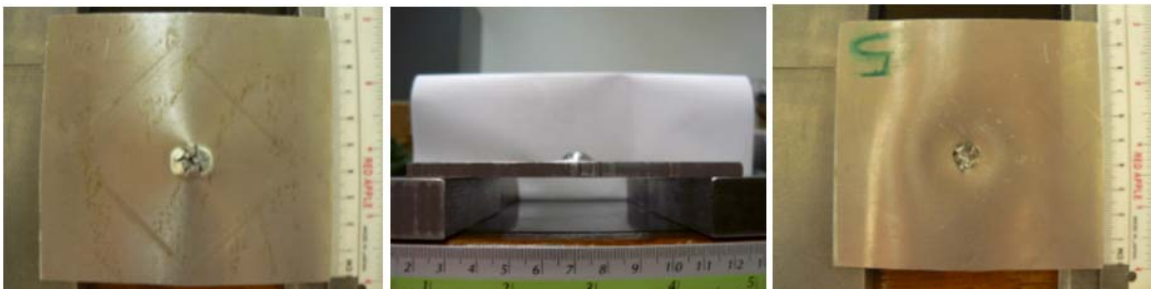


Figure 39. Target Samples and the Associated Damage of the AISI 4140 Steel Plate Impacted with ½” A2 Projectile at 596m/s. No Penetration was Observed.

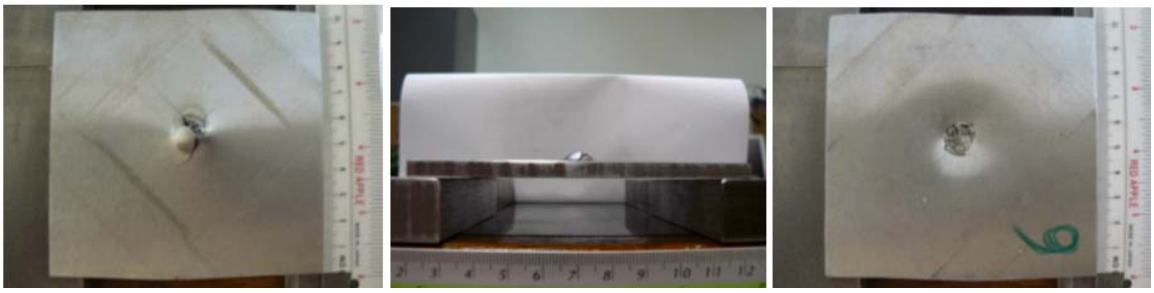


Figure 40. Target Samples and the Associated Damage of the AISI 4140 Steel Plate Impacted with ¾” A2 Projectile at 500m/s. No Penetration was Observed.

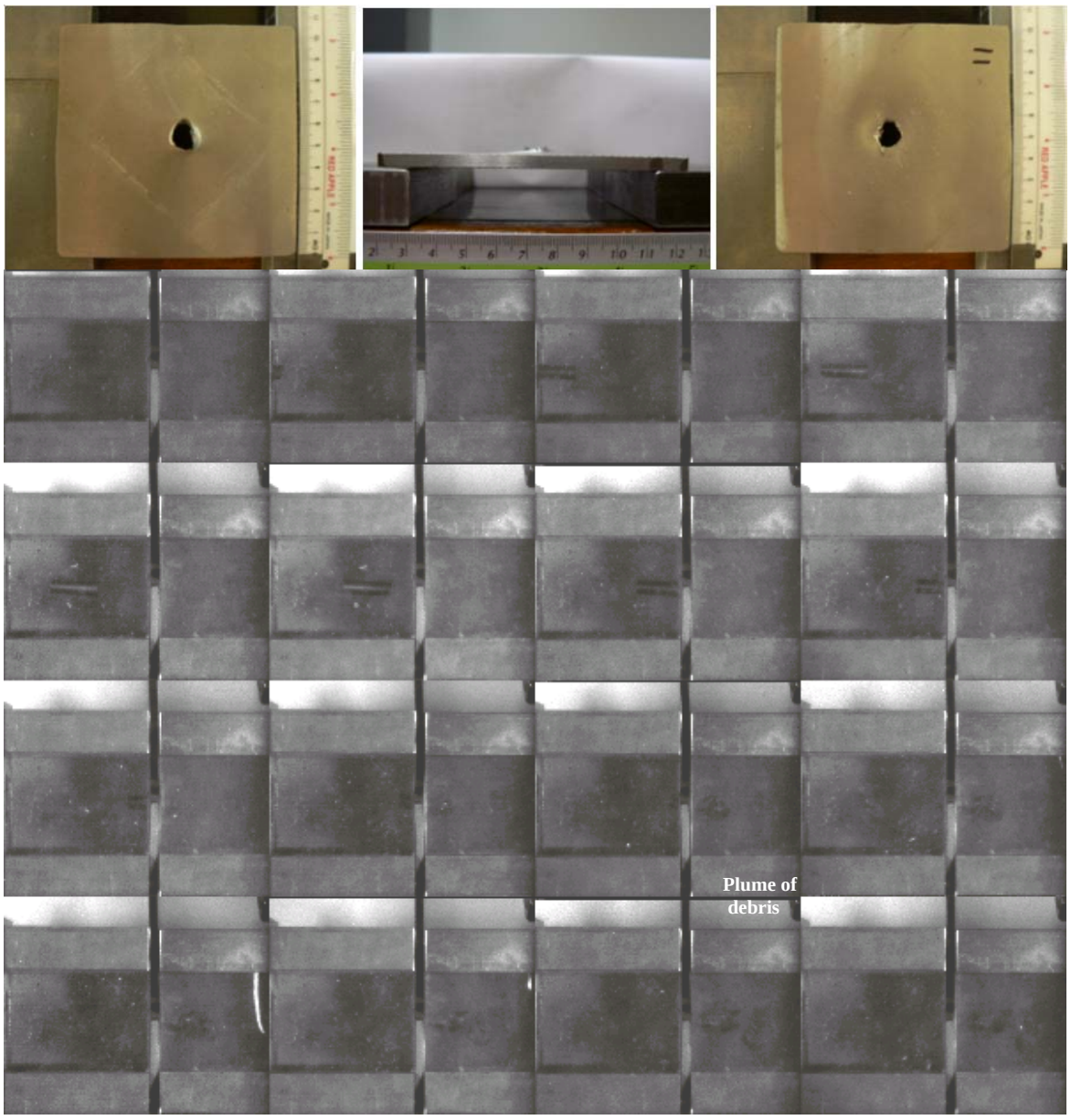


Figure 41. Target Samples and High Speed Camera Frame Photographs and the Associated Damage of the AISI 4140 Steel Plate Impacted with 1" A2 Projectile at 484m/s.

3. Composite Plates

Having established the minimum projectile size and velocity (hence kinetic energy), the next stage was to test the performance of the composite plates with reference to the AISI 4140 armor steel plate. The subsequent tests shown in Table 15. were done in a progressive manner to evaluate the effects of each material in penetration resistance.

Note that some of these composite plates have a thin Aluminum (Al) back layer and some do not. This plate serves to provide rear support to the foam materials.

Table 15. Test Set 3 – Composite Plates using Ceramic (C), Dyneema HB25 (D) and PU Foams (P1 and P2)

Sample/ Projectile Shape	Projectile Matl	Impact Velocity (m/s)	Penetrate (Y/N)	Volume (mm3)	Mass (gm)	KE (J)	Relative KE Ratio
C-D							
Rod (1")	RHC 55-56	483	N	1122.137626	8.696567	1014.407	1.0000
C-D-P1-AL							
Rod (1")	RHC 55-56	481	N	1122.137626	8.696567	1006.023	0.9917
C-D-P2-AL							
Rod (1")	RHC 55-56	463	N	1122.137626	8.696567	932.1371	0.9189

All three composite plates were able to resist the 1" A2 projectile. This was a direct indication of the better performance afforded by the composite construction over that of the AISI 4140 armor steel of equivalent areal density. Figure 42. -44 shows the actual sample and damage results.

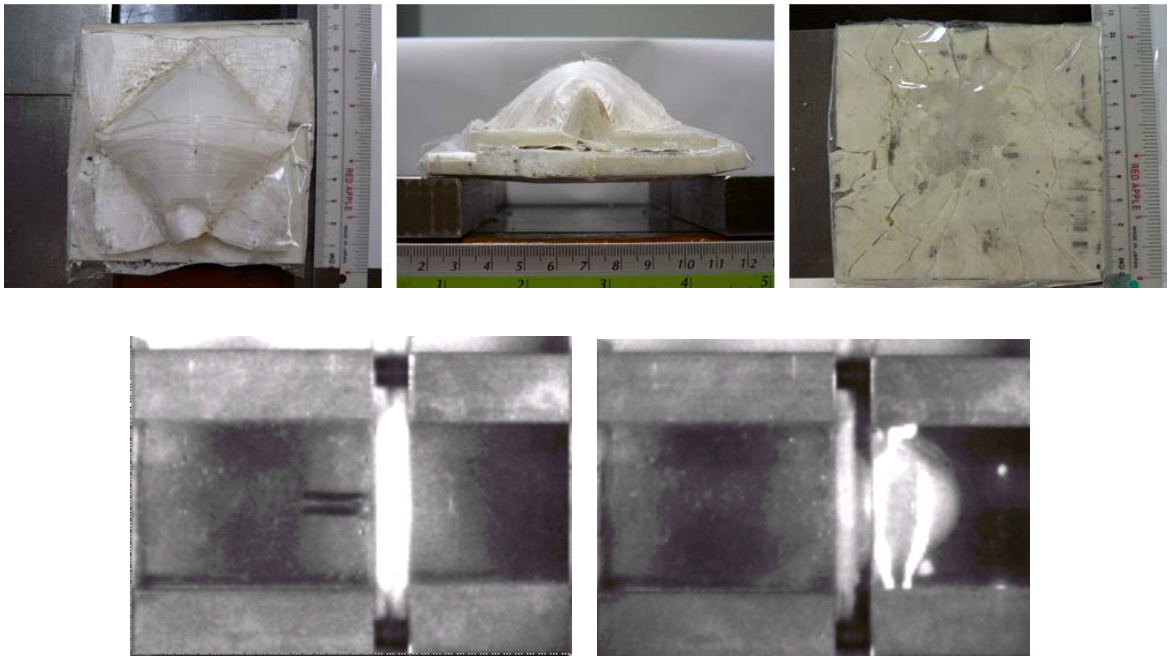


Figure 42. Sample of C-D Showing Complete Fracture of the Ceramic First Layer, and no Penetration of the Projectile.

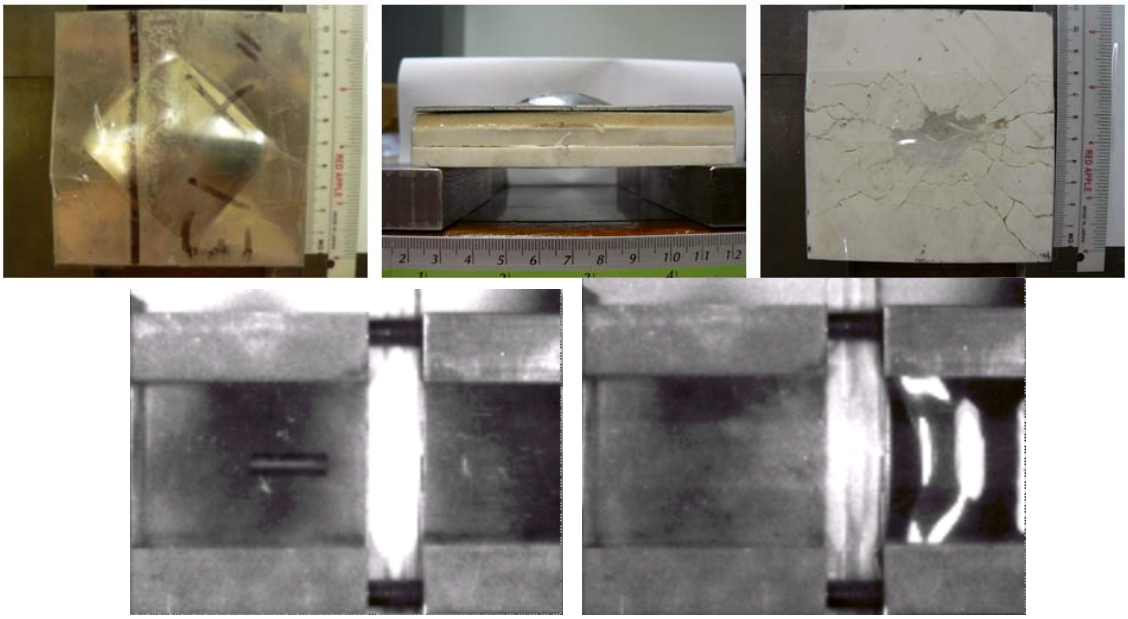


Figure 43. Sample of C-D-P2-Al Showing Complete Fracture of the Ceramic First Layer, and no Penetration of the Projectile.

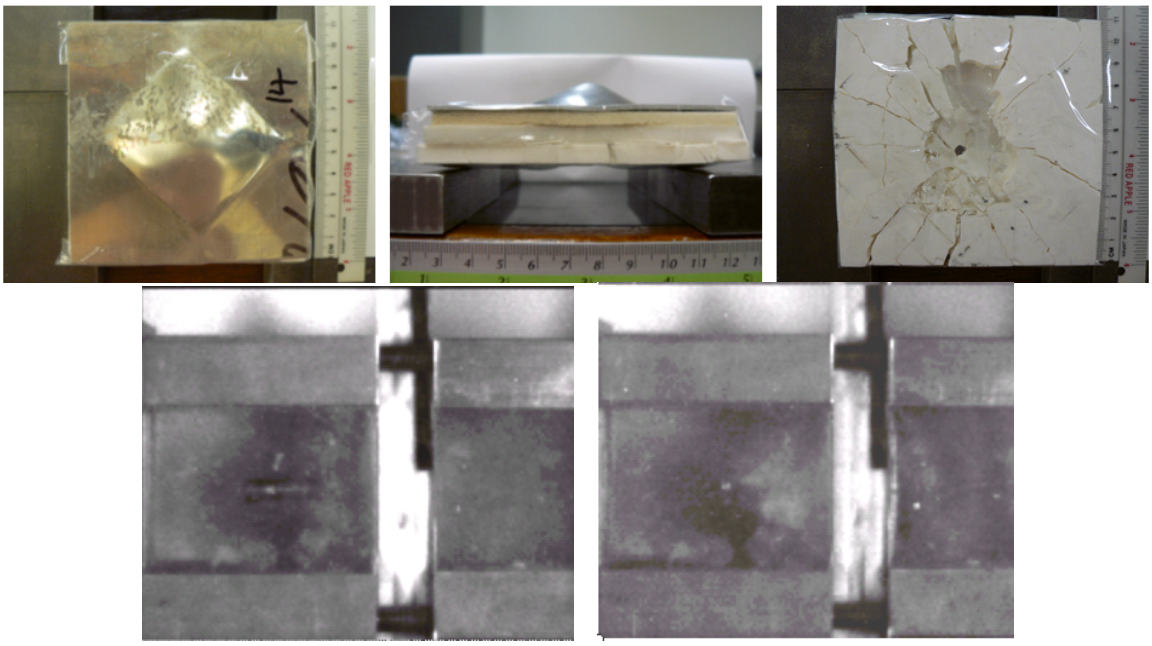


Figure 44. Sample of C-D-P1-Al Showing Complete Fracture of the Ceramic First Layer, and no Penetration of the Projectile.

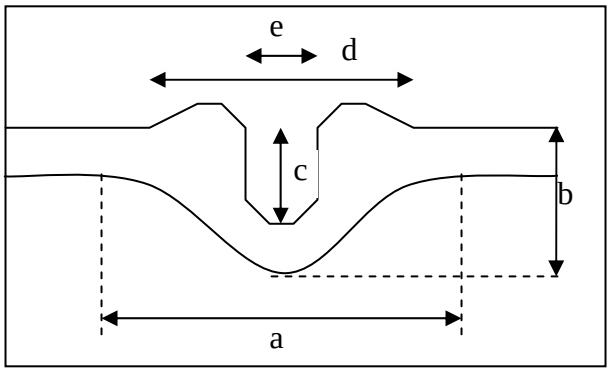


Figure 45. Dimensions that were measured using a 1/1000th accuracy Venier Calipers

0summarizes the damage results:

Table 16. Post Test Measurements of Specimen Damage

Description	Proj Type	Proj Speed (m/s)	Width bulge (mm)	Overall Depth (mm)	Hole Depth (mm)	Hole Crater (mm)	Hole Diameter (mm)
Designation			a	b	c	d	e
Dyneema HB25	9/32 Ball	610	77.55	18.57	18.57	13.67	6.36
D-P-AL	9/32 Ball	633	31.59	25.54	25.54	16.4	4.5
AISI 4140	½" Cylinder	596	15.16	10.06	2.27	11	8.77
AISI 4140	¾" Cylinder	500	19.88	12.01	2.26	13.83	9.15
AISI 4140	1" Cylinder	484	14.74	9.25	9.25	12.47	8.44
C-D	1" Cylinder	483	100	45.97	39.36	25.51	25.51
C-D-P2-AL	1" Cylinder	463	77.51	32.64	17.91	21.58	21.58
C-D-P1-AL	1" Cylinder	481	75.16	35.12	21.27	31.76	31.76

E. COMMENTS FROM THE LIVE FIRING EXPERIMENT

1. Dyneema

Dyneema HB25 on its own is unable to resist the penetration by a spherical ball projectile at speeds in excess of 600 m/s. It appears that this is not significantly mitigated by the addition of a porous PU foam behind to act as a shock absorber.

2. Composite Plate

The Ceramic/Dyneema composite plate of lower areal density outperformed that of the AISI 4140 armor steel. This provides the proof of concept for armor protection that

this investigation had initially set out to achieve. The next stage of the investigation is to develop as completely as possible the material models of the materials used in this investigation to facilitate further research.

3. Ceramic

The technical ceramic used in this experiment provided an impressive first layer to reduce the velocity of the incoming projectile through violent/brittle fracture (hence work done). This is evident from the effect that an addition of a ceramic layer had in resisting the penetration of a 1” projectile when the Dyneema HB25 alone could not defeat even a 9/32” diameter steel sphere of lower kinetic energy. We note here that the ceramic layer is expected to be even more effective against penetrators that are less hard than those used in this study. This is because, for softer projectiles, there will be a greater amount of plastic deformation when they strike the very high compressive strength ceramic material. This effectively converts projectile kinetic energy into heat through the plastic flow process.

4. Porous PU Foam

The addition of a porous foam layer decreased the amount of target deformation significantly by almost 29%. It can be said that energy dispersion by the Dyneema HB25, as well as energy absorption by the porous PU foam, are both very different processes and can be treated separately. The combination of these effects enhances penetration resistance and decreases the total amount of deformation considerably. Further explanation of the role of the polymeric foam material on the penetration process can be found in the thesis by Boey [6]. Generally speaking, the greater the porosity, subjected to a limit, the greater amount of energy absorption due to the combination effects of elastic buckling of cell walls, plastic deformation of collapsing cell walls, and volume compression. Boey has also demonstrated that the inertial backing plate is necessary to prevent the porous media from spalling thus impeding its ability to absorb shock energy.

This concludes the results obtained from the live firing experiment. The next

stage of this study was to reproduce these results numerically in order to validate our material models used in Autodyn®.

THIS PAGE INTENTIONALLY LEFT BLANK

V. AUTODYN® SIMULATIONS

Having obtained the results from the live firing experiment, it was then desirable to check the material models that were developed earlier, against the experimental results. The greatest difficulty at this point was to arrive at a set of parameters that adequately and reasonably describe the Dyneema HB25 material which was used. Properties for other materials used in this research were presumably more well- established and available in open literature. Design parameters for the porous PU foam were obtained from Boey [7].

The approach was to use Autodyn® and to define material properties for the materials that are to be used in the experiment based on either literature research or reasonable estimations. Some assumptions are necessary due to the lack of literature values for some of these properties and the lack of resources and time to do detailed material testing on the target samples in order to obtain the actual mechanical properties. The objective was to derive the material parameters necessary to model Dyneema HB25, which is referred as D1 in the Autodyn® simulations. Dyneema HB25 is a propriety material, and detailed mechanical properties are not available in the literature at this time.

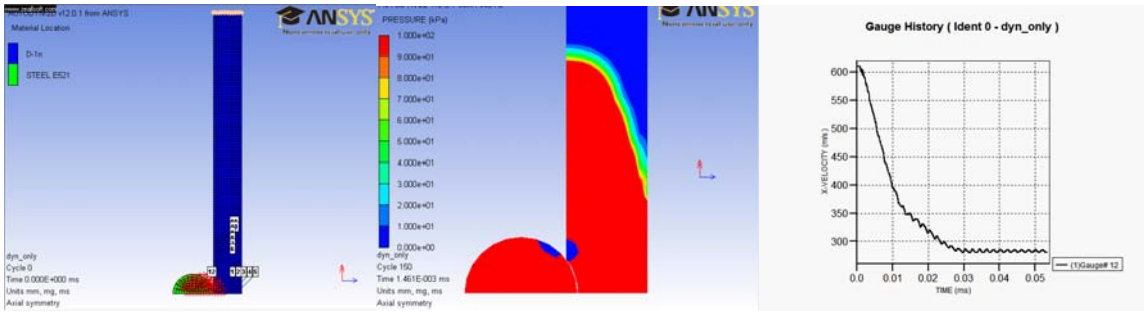
Table 17. shows the Autodyn® simulations that were done to attempt to reproduce the results of the experiment. These configurations were chosen with the focus of validating the material parameters used to simulate the behavior of the Dyneema HB25.

Table 17. Autodyn® Simulation

Target Configuration	Projectile Shape	Projectile Material	Impact Velocity (m/s)	Penetrate (Y/N)
D1	Sphere (9/32”)	E52100 – RHC 60-67	610	Y
Steel AISI 4140	Rod (1/2")	A2 – RHC 53-60	596	N
Steel AISI 4140	Rod (3/4")	A2 – RHC 53-60	500	N
Steel AISI 4140	Rod (1")	A2 – RHC 55-56	484	Y
C-D1	Rod (1")	A2 – RHC 55-56	483	N
C-D1-P1-Al	Rod (1")	A2 – RHC 55-56	481	N
C-D1-P2-Al	Rod (1")	A2 – RHC 55-56	463	N

A. D1

In order to validate the material model parameters that were assumed and defined in Chapter II, an Autodyn® simulation to replicate the live firing was done. As described in Table 17, a 9/32" E52100 Steel Ball was used as the projectile and was fired at 610m/s towards the D1 target. Figure 46. and Figure 47. illustrate the key results of the simulation. Table 18. gives the material properties of the E52100 Steel used in the simulations. The Equation of State (EOS) and Strength Model were referenced from that of S-7 Steel available in Autodyn® Library. The Yield Stress of 2.0 GPa was referenced from ASTM A295 for E52100 Steel. A Hydro (pmin) value of -2.0 GPa was chosen to reasonably assume that the E52100 steel will fail when any element experiences a tensile stress of 2 GPa or greater. In this case, it is unlikely that the steel projectile will encounter tension stresses, and so, this value has little consequence to our results.



(a) (b) (c)

Figure 46. D1 Problem Setup. Impact Velocity was the Same as That of the Experiment – 610m/s. (a) Problem Setup of a 9/32"E52100 Steel Ball impacting a D1 Target. (b)Shock Wave Propagation at 1.5μs after Impact. (c)Simulation Residual Velocity was 275 m/s.

Shock wave propagation was as expected as before having an elliptical shock wave that propagates outwards faster in the 22/33 directions. The residual velocity was about 275 m/s, which is about 12.3% (based on 610m/s impact velocity) lower than what was recorded in the experiment of 350 m/s.

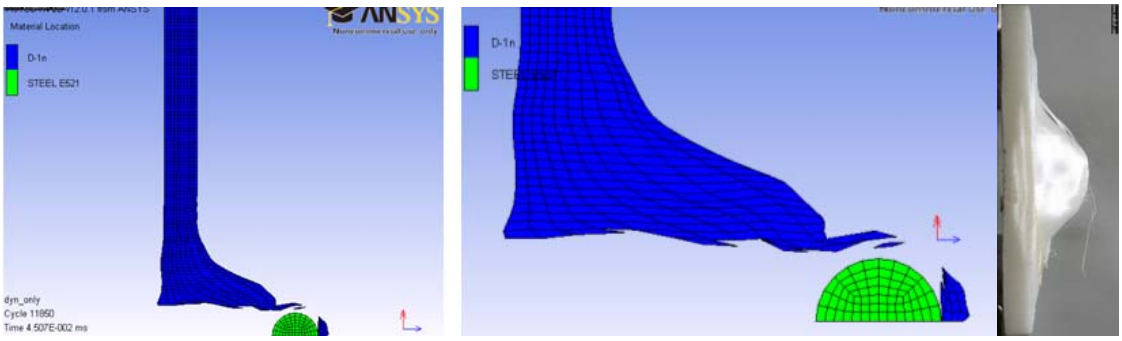


Figure 47. End State of Autodyn® Simulations Showing Complete Penetration with 275 m/s Residual Velocity. The Actual Damage Sample is on the Right for Comparison Purposes.

Table 18. Material Properties of E52100 CARBON STEEL Projectile

EOS	SHOCK
Ref Density	7.75gm/cc
Gruneisen Coeff	2.17
C1	4569 m/s
S1	1.49
Quadratic S2	0
Ve/Vo	0
Vb/Vo	0
C2	0
S2	0
Ref Temp.	300 K
Specific Ht	477 J/kgK
Thermal Conductivity	0 J/mKs

Strength	Johnson Cook
Shear Modulus, G	81.8 GPa
Yield Stress	2.0 GPa
Hardening Const	477 MPa
Hardening Expnt	0.18
Strain Rate Constant	0.012
Thermal softening Exponent	1.00
Melting Temp	1763
Ref Strain Rate	1.0
Strain Rate Correction	1st order

Failure	Hydro (Pmin)
Hydro Tensile Limit	-2 GPa
Reheal	Yes
Crack Softening	No
Stochastic Failure	No
Erosion	Geometric Strain
Erosion Strain	2.0
Type	Instantaneous

Table 19. Quantitative Comparison between Autodyn® Results and Those of the Experiment for the Dyneema HB25 Sample.

Target	Proj Shape/ Material	Imp Speed (m/s)	Type	Width Bulge (mm)	Overall Depth (mm)	Hole Depth (mm)	Hole Crater (mm)	Hole Dia (mm)
D1	Sphere (9/32")	610	Experimental	77.55	18.57	18.57	13.67	6.36
	E52100		Autodyn ®	33.12	16.77	16.77	15.15	9.3126
	Complete Penetration		**Deviation**	-57.29%	-9.69%	-9.69%	10.83%	46.42%

As can be seen from Table 19. , the overall deformation and hole crater is within 10% of the actual experimental results which shows very good indication of the material model that is being used to describe the behavior of the Dyneema HB25. However, it does not model the bulging layers as observed behind that Dyneema sample as well, as can be seen from the 57% difference in the width of the bulge. From Figure 47. , it can be seen that the projectile shears through a good first 50% of the layers before delamination begins and elastic/plastic deformation (stretching) begins. This is in good agreement with what is being observed for the actual Dyneema HB25 sample.

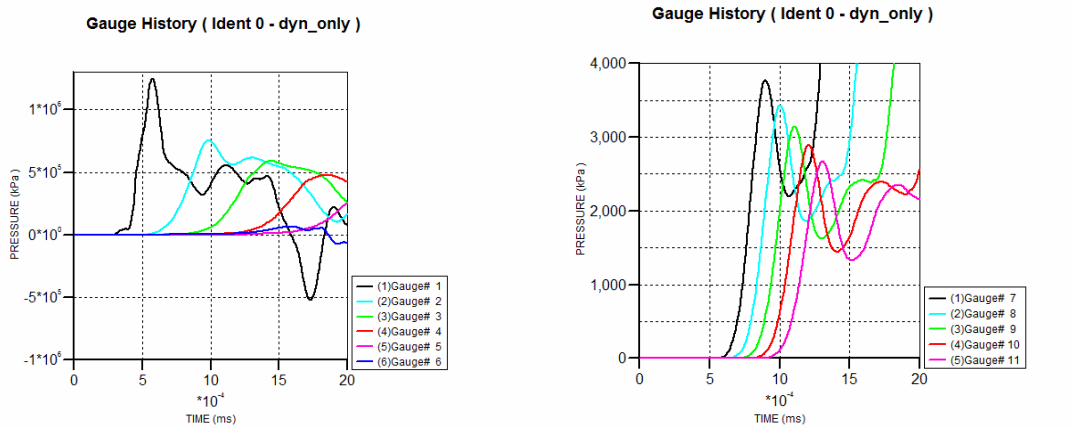


Figure 48. (Left) Shockspeed of 3.0 km/s was seen to propagate in the 11 direction. (Right) In the 22/33 directions, the shockspeed was 9.9 km/s.

Figure 48. shows the shock speed in the 11- and 22/33-directions. As before, the shock speed in the 22/33-direction was considerably faster than that in the 11-direction.

From the results of this simulation, it can be concluded that the D1 material properties which were defined above approximates the behavior of Dyneema HB25 fairly well.

B. AISI 4140 STEEL PLATE

The next sequence of simulations set out to establish a numerical model from which future AISI 4140 target samples performance subjected to high velocity impact from A2 material projectiles can be predicted. The following were the properties of the AISI 4140 Steel Plate that was used in the modeling. The material properties in Table 20. were taken from the Autodyn® Material Library of 4340 steel, with slight modifications to its yield strength.

Table 20. Material Properties of AISI 4140 STEEL

EOS	LINEAR	Strength	Johnson Cook	Failure	JOHNSON COOK
Ref Density	7.83gm/cc	Shear Modulus, G	77 GPa	Damage Constant, D1	0.005
Bulk Modulus	159 GPa	Yield Stress	655MPa	Damage Constant, D2	3.44
Ref Temp.	300 K	Hardening Const	510 MPa	Damage Constant, D3	-2.12
Specific Ht	477 J/kgK	Hardening Expnt	0.26	Damage Constant, D4	0.002
Thermal Conductivity	0 J/mKs	Strain Rate Constant	0.014	Damage Constant, D5	0.61
		Thermal softening Exponent	1.03	Melting Temperature	1793 K
		Melting Temp	1793	Ref Strain Rate	1.0
		Ref Strain Rate	1.0	Erosion	Geometric Strain
		Strain Rate Correction	1st order	Erosion Strain	2.0
				Type	Instantaneous

A 0.295” diameter A2 cylinder was modeled as the projectile, and its length was varied to replicate the experimental sequence. The A2 tool steel properties are shown in Table 21.

Table 21. Material Properties of AISI A2 TOOL STEEL

EOS	SHOCK
Ref Density	7.75gm/cc
Gruneisen Coeff	2.17
C1	4569 m/s
S1	1.49
Quadratic S2	0
Ve/Vo	0
Vb/Vo	0
C2	0
S2	0
Ref Temp.	300 K
Specific Ht	477 J/kgK
Thermal Conductivity	0 J/mKs

Strength	Johnson Cook
Shear Modulus, G	81.8 GPa
Yield Stress	1.8 GPa
Hardening Const	477 MPa
Hardening Expnt	0.18
Strain Rate Constant	0.012
Thermal softening Exponent	1.00
Melting Temp	1763
Ref Strain Rate	1.0
Strain Rate Correction	1st order

Failure	Hydro (Pmin)
Hydro Tensile Limit	-2 GPa
Reheal	Yes
Crack Softening	No
Stochastic Failure	No
Erosion	Geometric Strain
Erosion Strain	2.0
Type	Instantaneous

A total of 3 trials (½", ¾" and 1" length cylinders) were required to establish the minimum kinetic energy required to penetrate the AISI 4140 armor steel during the experiment. Figures 49-51 show the results of the simulations.

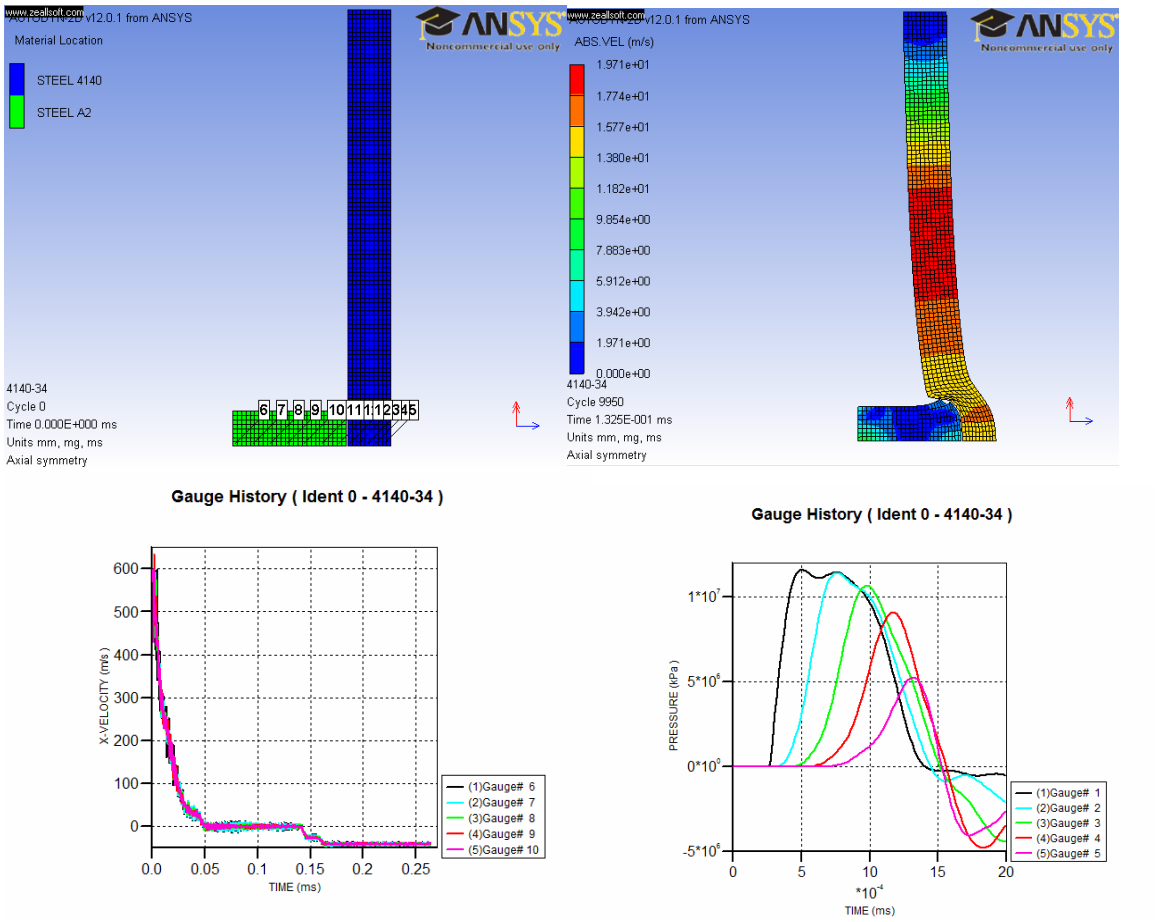


Figure 49. Results of Autodyn® Simulations of a ½" A2 Cylinder Projectile Impacting AISI 4140 Steel at 596m/s. (Top Left)Problem Setup of a ½"A2 Steel Cylinder Impacting at 595 m/s onto a AISI 4140 Steel Plate. (Top Right)Projectile is stopped by the Steel Plate. (Bottom Left)Velocity Profile of the Steel Projectile. (Bottom Right)Pressure-Time Profile in the Target Steel Plate.

As can be seen from Figure 49. , at an impact speed of 596m/s, the ½" projectile is stopped and is in fact repelled by the target AISI 4140 steel plate. A peak interfacial pressure of 11.4 GPa is obtained.

Simulations involving a ¾" cylinder projectile yielded almost the same results. Figure 50 shows the simulations.

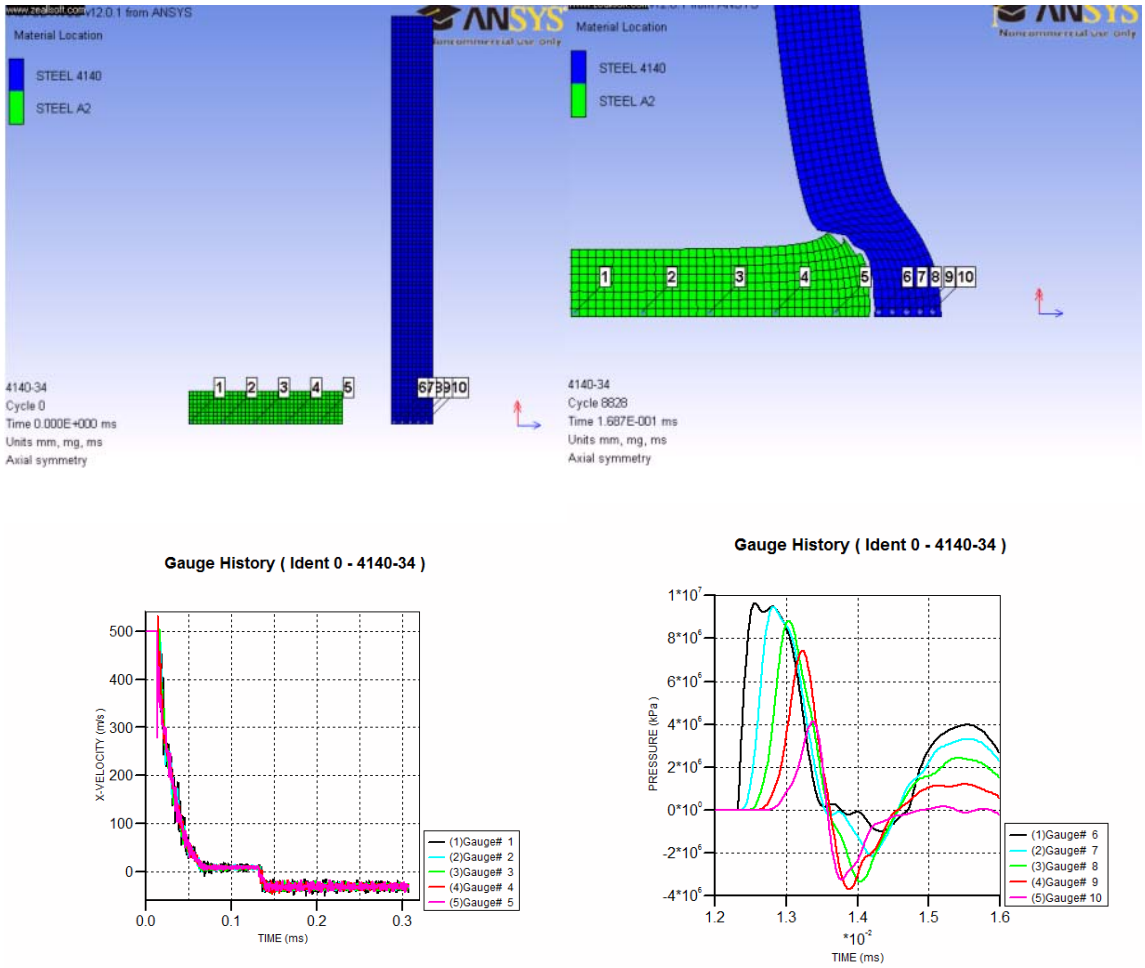


**Figure 50. Results of Autodyn® Simulations of a ¾" A2 Cylinder Projectile Impacting AISI 4140 Steel at 500m/s. Peak Interfacial Pressure was 9.52 GPa. (*Top Left)Problem Setup of a ¾"A2 Steel Cylinder Impacting at 500 m/s onto a AISI 4140 Steel Plate. (Top Right)Projectile is stopped by the Steel Plate. (Bottom Left)Velocity Profile of the Steel Projectile. (Bottom Right)Pressure-Time Profile in the Target Steel Plate.*

The 3rd simulation shown in Figure 51, produced results which replicated that 3rd steel plate experiment. Penetration of the AISI 4140 steel plate was achieved with a projectile residual velocity of 137 m/s, which was higher than the experimental result of 118m/s. This reason for this is that in the experiment, the projectile was completely fractured in the process, and this takes away its kinetic energy resulting in a slightly lower residual velocity observed.

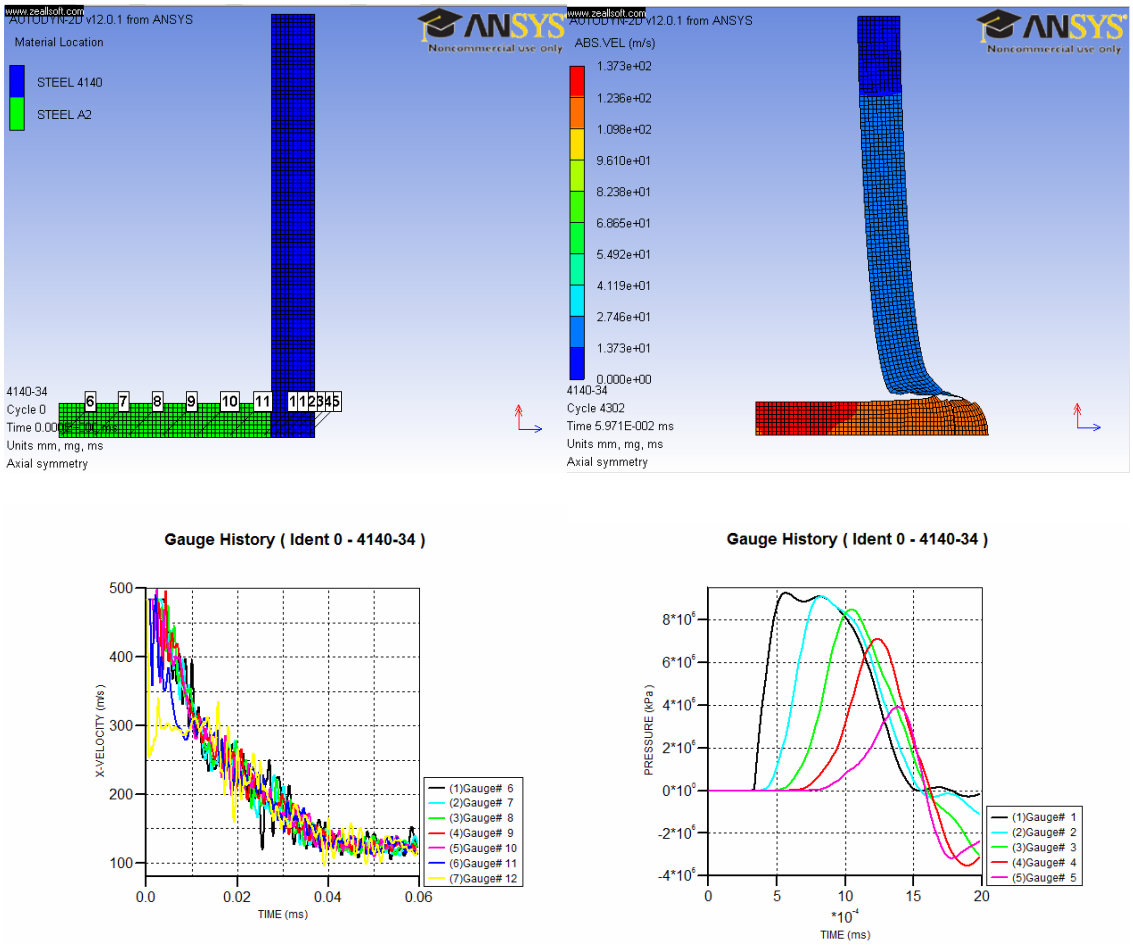


Figure 51. Results of Autodyn® Simulations of a 1" A2 Cylinder Projectile Impacting AISI 4140 Steel at 484m/s. A Peak Interfacial Pressure of 9.07 GPa is Obtained. ***(Top Left)Problem Setup of 1"A2 Steel Cylinder Impacting at 484 m/s onto a AISI 4140 Steel Plate. (Top Right)Projectile is shown to penetrate the Steel Plate. (Bottom Left)Velocity Profile of the Steel Projectile with a residual velocity of 137 m/s is obtained. (Bottom Right)Pressure-Time Profile in the Target Steel Plate.***

The preceding section concluded the simulations which reproduced the results necessary to prove that the 5mm AISI 4140 armor steel plate was unable to resist the penetration from a 1" A2 tool steel cylinder fired at 484m/s. These results serve to bracket the conditions needed to fully penetrate the AISI 4140 plate.

It is now appropriate to present simulations of the composite plates which proved to be more effective than the AISI 4140 armor steel plate of equivalent areal density in resisting penetration from the same projectile.

C. COMPOSITE PLATE NUMERICAL SIMULATIONS

The final set of simulations involved validating the combined performance of Ceramic, Dyneema and PU foams. 3 configurations of the composite plates were tested in a sequential manner: C-D1, C-D1-P1-Al and C-D1-P2-Al. The simulations using Autodyn® are presented here, and a brief discussion and comparison is followed thereafter.

1. Composite Plate C-D

A composite target comprising of a 6mm Ceramic layered over a 5mm D1 material was modeled as shown in Figure 52. . As before, an A2 1" length cylinder was made to impact at 483 m/s. It can be seen in Figure 53. that the failure mechanism observed in the simulations agrees well with what was observed in the experiment. Due to the presence of the ceramic plate, there is delamination of the D1 material in all the layers, without shearing failure, and large deformation of the D1 material in the rear. Comparison of the deformation measurements of the Autodyn® simulations and those of the actual samples is discussed at the end of this section.

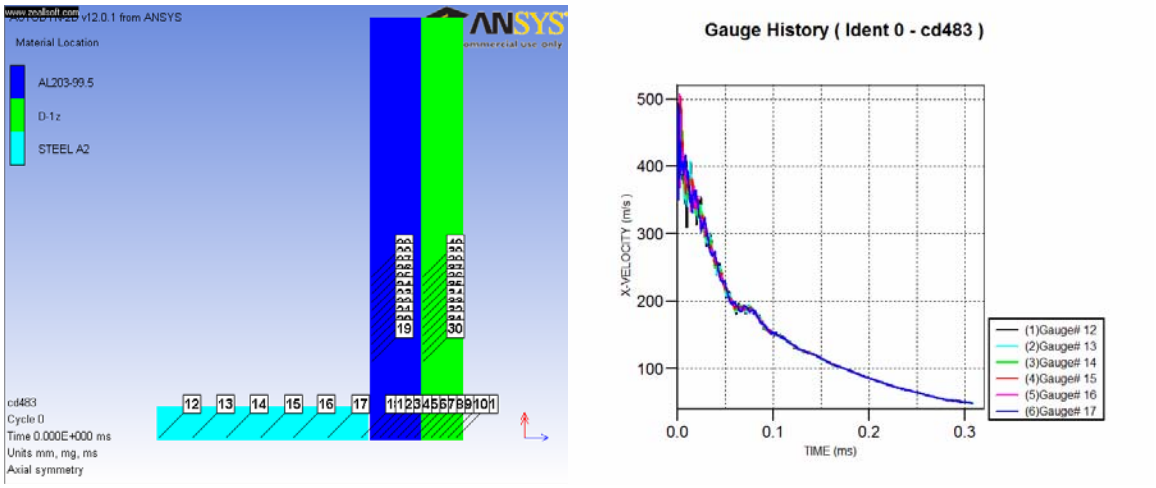


Figure 52. (Left) Problem Setup of 1" A2 Steel Cylinder Rod Impacting at 483 m/s onto a Composite Plate Comprising of Ceramic, and D1 (C-D1). (Right) Velocity Profile showing that the Projectile is stopped after about 0.32 ms.

Gauges were set up in the through thickness direction, as well as the 22-directions. The projectile was arrested (zero velocity) about 0.32ms after impact.

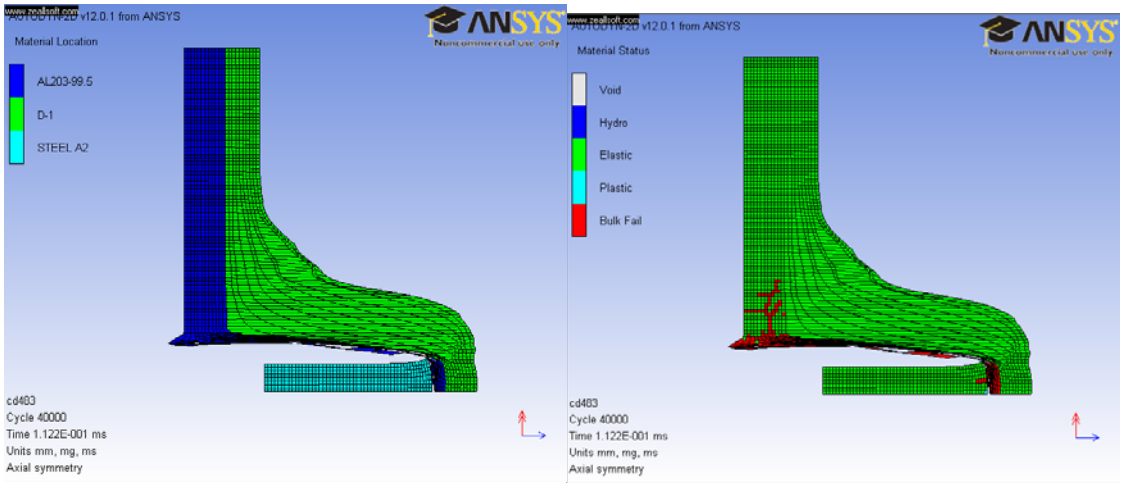


Figure 53. Results of Autodyn® Simulations of Composite Plate (C-D1). (Left) Final Deformation Shape of the Composite Plate. (Right) Bulk Failure and Brittle Fracture of the Ceramic Plate can be observed.

Ceramic is seen to develop cracks and show bulk failure. D1 shows obvious delamination and also tensile failure of the fibers.



Figure 54. Cross Sectional View of the Actual Composite Plate (C-D1) for Comparison.

2. Composite Plate C-D1-P1-AL

Composite plates were modeled with 6mm Alumina ceramic, 5mm Dyneema

HB25, 5mm PU Foam 0.16 gm/cc and a thin 1.5mm Aluminum 6061-T6 backing inertial backing plate to provide confinement for the porous foam. Boey [6] has shown the necessity of adding confinement to PU porous foams so as to facilitate the collapse of the cell walls and volume compression of the air voids. Material properties of the first 3 materials were presented earlier. The material properties of the aluminum are shown in Table 22.

Table 22. Material Properties of AL 6061-T6

EOS	SHOCK
Ref Density	2.703gm/cc
Gruneisen Coeff	1.97
C1	5240 m/s
S1	1.4
Quadratic S2	0
Ve/Vo	0
Vb/Vo	0
C2	0
S2	0
Ref Temp.	300 K
Specific Ht	885 J/kgK
Thermal Conductivity	0 J/mKs

Strength	SteinBerg Guinan
Shear Modulus, G	27.6 GPa
Yield Stress	290 MPa
Max Yield Stress	680 MPa
Hardening Const	125
Hardening Expnt	0.1
dG/dP	1.8
dG/dT	-17 MPa
dY/dP	0.018908
Melting Temp	1220 K

Failure	Hydro (Pmin)
Hydro Tensile Limit	-2 GPa
Reheal	Yes
Crack Softening	No
Stochastic Failure	No
Erosion	Geometric Strain
Erosion Strain	2.0
Type	Instantaneous

Simulation results are presented as follows in Figure 55. .

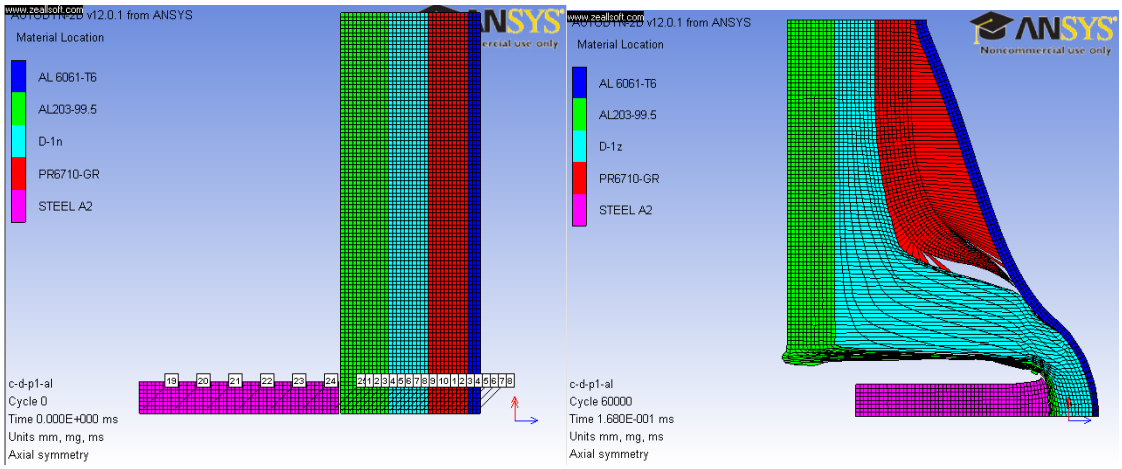


Figure 55. Problem Setup of C-D1-P1-Al Composite Plate. Impact velocity is 481m/s.

The final deformation shape is shown on the right of Figure 55. . Complete crushing of the PU foam, delamination of the D1 layer, and brittle fracture of the ceramic is observed.

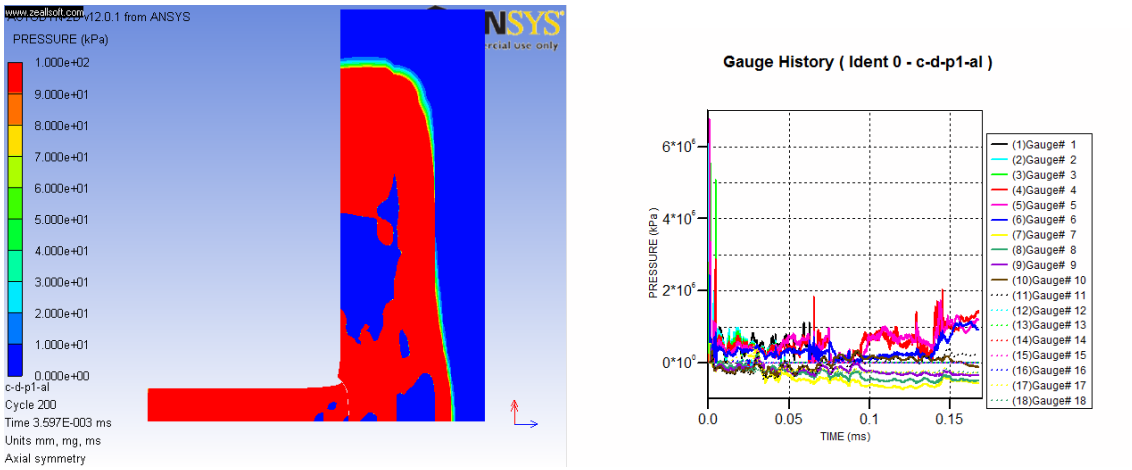


Figure 56. Shock Wave Propagation in the 11 and 22 directions. Overall Shock Pressure is Shown on the Right.

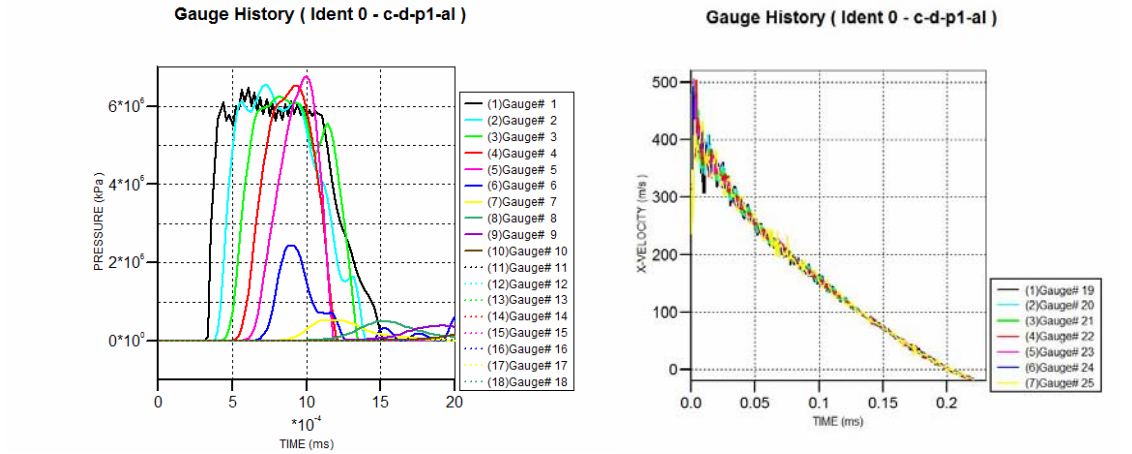


Figure 57. (Left) Peak Pressure Profiles Obtained During the Initial Stages of Impact. (Right) Time Taken for Projectile to Reach Zero Velocity was 0.2 ms.

As shown in Figure 57, the peak pressure was about 6.1 GPa in the ceramic. There is an obvious low pressure region where the shock wave meets the interface

between ceramic and D1 as shown by the very low pressures of gauges 7-12. Time taken to arrest the projectile was about 0.2ms.

3. Composite Plate C-D1-P2-AL

The 3rd configuration of the composite plate used a higher density PU foam of the same thickness. PU foam density was increased from 0.16gm/cc to 0.32gm/cc. All other factors and materials remained the same. The following illustrates the simulation results.

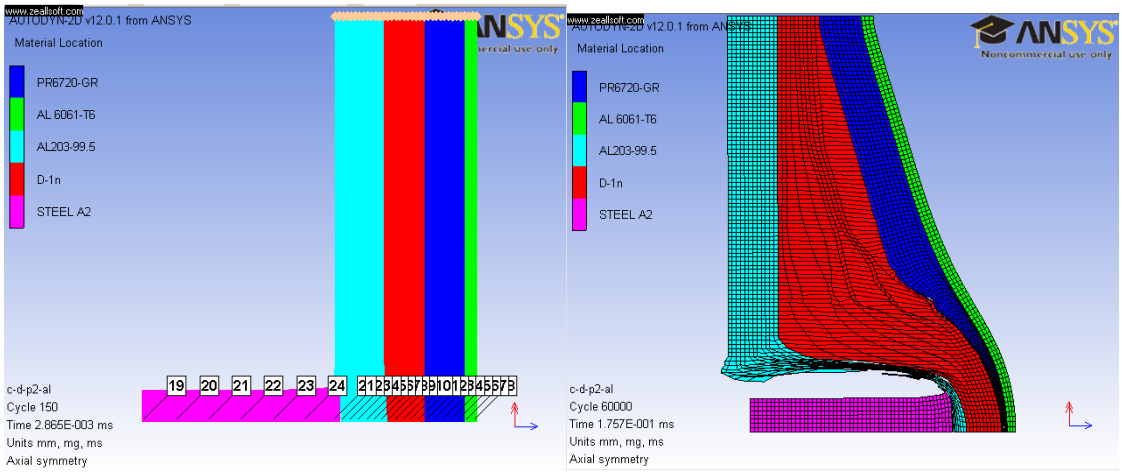


Figure 58. Problem Set up of C-D1-P2-Al Composite Plate. Impact Velocity of 463m/s. Final Deformation Shape is Shown on the Right. .

Partial crushing of the PU foam, delamination of the D1 layer, and brittle fracture of the ceramic is observed.

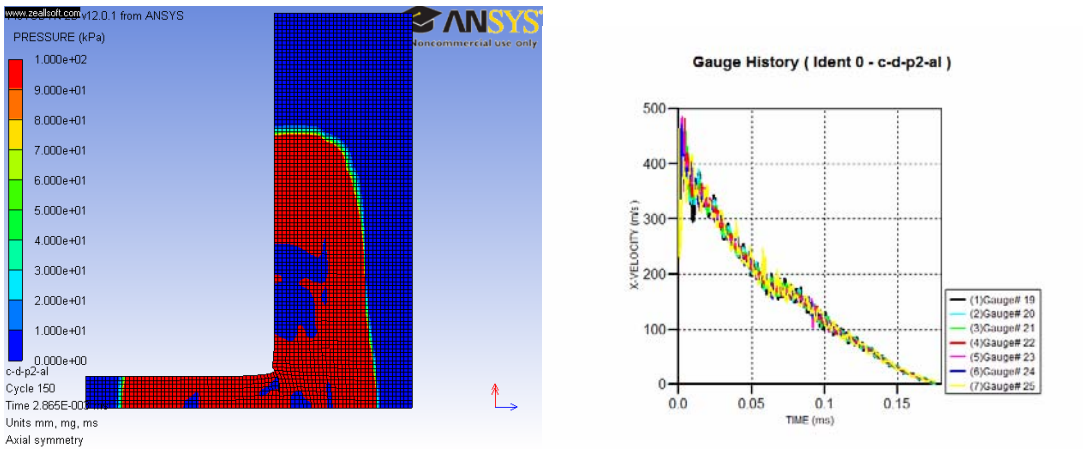


Figure 59. Shock Wave Propagation in the 11 and 22 directions. Time Taken to Arrest the Projectile was 0.177ms

Comparing the total time taken to arrest the projectile, C-D1-P1-AL took 0.023ms (13%) more time than C-D1-P2-AL which was made of a denser foam. From the outset, it is observed that the higher density PU foam (P2) actually reduces the total time taken to arrest the projectile. This could be due to the greater energy absorption ability of a more dense foam and hence a more rapid reduction of impact kinetic energy. As a consequence of this, it would be expected that the total deformation of the composite plate for C-D1-P2-Al be lower than that of C-D1-P1-Al based on simulations. However, due to experimental limitations, the impact velocity for the C-D1-P2-Al sample was about 18m/s (3.7%) smaller than that of C-D1-P1-Al, and therefore, there is a need to compare their performance at the same impact velocity using computer simulations.

D. COMPARISON (EXPERIMENT VS. AUTODYN®)

Having completed the simulations and the live firing experiments, it is possible to compare the results of each in order to determine the quality of the material modeling and the relative performance of the composites. Table 23. summarizes the results.

Table 23. Comparison of Experimental and Autodyn® Results

Target Configuration	Projectile Shape/ Material	Type	Width Bulge (mm)	Overall Depth (mm)	Hole Depth (mm)	Hole Crater (mm)	Hole Dia (mm)	Time (ms)
C-D1	Rod (1")	E	100	45.97	39.36	25.51	25.51	

Impact vel. 483m/s	A2 – RHC 55-56	A	38.98	49.9	43.2	16.85	12.87	0.320
		D	**-61.0%**	**9.14%**	**9.76%**	**-33.94%**	**-49.6%**	
C-D1-P1-Al Impact vel. 481m/s	Rod (1") A2 – RHC 55-56	E	75.16	35.12	21.27	31.76	31.76	
		A	100	39.21	32.91	17.32	13.04	0.200
		D	**33.05%**	**11.65%**	**54.72%**	**-45.47%**	**-58.94%**	
C-D1-P2-Al Impact vel. 463m/s	Rod (1") A2 – RHC 55-56	E	77.51	32.64	17.91	21.58	21.58	
		A	100	34.636	27.135	18.1	12.03	0.177
		D	**29.02%**	**6.12%**	**51.51%**	**-16.13%**	**-44.25%**	

Legend:
C – Ceramic 6mm thick
D1 – Replicate closely Dyneema HB25 5mm thick
P1 – PU foam 5mm thick, ρ=0.16gm/cc
P2 – PU foam 5mm thick, ρ=0.32gm/cc
E - Experimental
A - Autodyn ®
D - Deviation

1. Overall Depth

It is to be expected that Autodyn® produces results which show larger overall depth and bulge width compared to those observed in the experiment because of the confinement effects due to the experimental set up. It can be seen that the simulations have approximated the deformation in the 11-direction fairly accurately, with a maximum error of 11.65%.

2. Time Taken to Arrest Projectile

C-D1 performed the worst in this experiment as it took the longest time, 0.32ms, to arrest the projectile probably due to the failure mechanism of delamination and plastic deformation of the Dyneema fibers. Addition of the PU foams (C-D1-P-Al configurations) cut down the time by almost half (~0.17ms) due to energy dissipation through volume compression, and hence less work done on the Dyneema to cause stretching and delamination.

3. Porous Foams

Between C-D1-P1-AL and C-D1-P2-AL, it is difficult to conclude whether a more dense foam such as P2 was better in absorbing the energy of the projectile due to disparity in the impact velocities during the experiment. The lack of resources and time did not allow the experiment to be repeated. Hence, an Autodyn® simulation is needed to investigate the effects of varying the foam density. This is presented in the next section.

E. COMPARISON (AUTODYN® AT 483M/S)

As the actual experiments were done at slightly varying impact velocities, another set of simulations using the 3 composite target models were run with impact velocity of 483 m/s. This would allow us to establish a baseline from which to compare the attributes of each model.

The results are presented in Table 24. :

Table 24. Deformation Calculations from Autodyn® of Composite Plates with Impact Velocity of 483 m/s

Target Configuration	Projectile Shape	Projectile Matl	Time to Zero Velocity (ms)	Width Bulge (mm)	Overall Depth (mm)	Hole Depth (mm)	Hole Crater (mm)	Hole Dia (mm)
C-D1	Rod (1")	A2 – RHC 55-56	0.320	38.98	49.9	43.2	16.85	12.87
C-D1-P1-Al	Rod (1")	A2 – RHC 55-56	0.200	100	39.89	33.23	17.34	13.03
C-D1-P2-Al	Rod (1")	A2 – RHC 55-56	0.182	100	36.54	30.05	17.06	13.40

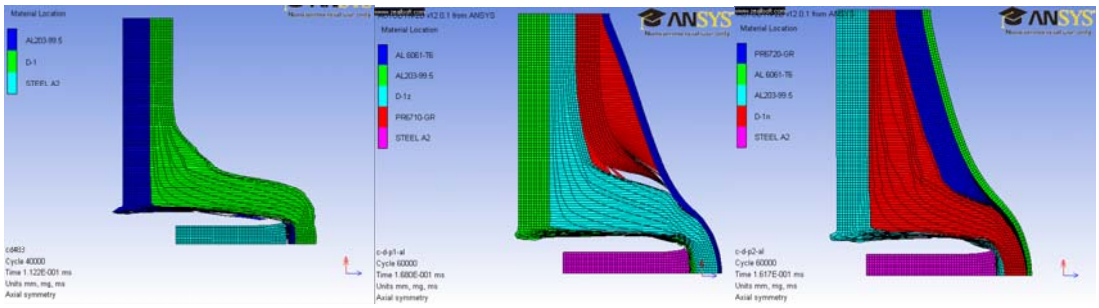


Figure 60. Comparative Autodyn® Simulation of the Three Composite Plates, C-D1, C-D1-P1-Al, and C-D1-P2-Al, Subjected to Same Projectile Impact at 483 m/s

These simulations predict that a more dense foam is able to arrest the projectile more efficiently in a shorter time, as well as produce the least overall deformation. This could be due to the greater amount of energy required to collapse the cell walls of a more dense foam, resulting in greater energy dissipation of the projectile kinetic energy. However, not enough information is available at this time to make a decisive conclusion, and more research needs to be done in this area to draw better conclusions. This will be discussed in more detail in the thesis by Boey [7].

F. LIMITATIONS OF SIMULATIONS AND EXPERIMENTS

Simulations were done using 100mm x 100mm target samples so as to minimize the end effects in resisting the dynamic impact load from the projectile. In the actual experiment, due to the way the clamping jig is constructed, only an effective area of

50mm x 50mm was used to resist the penetration of the projectile. Qualitatively speaking, if this effective area is increased, it would increase the penetration resistance of the composite target.

The maximum velocity of the gas gun was another limitation. Based on a 9/32" steel sphere, the maximum speed was only 658 m/s which was unable to penetrate the AISI 4140 armor steel. As such, a higher mass projectile was required (at the expense of velocity) to provide the necessary kinetic energy to penetrate the baseline sample. It should be noted that the failure mechanism of Dyneema is different at different velocities. At very high velocities (say > 600 m/s), it is expected that Dyneema will undergo shearing first, before delamination takes place. At lower velocities (say ~300m/s), Dyneema dissipates the impact energy more effectively through proper delamination of the layers as well as elastic/plastic elongation of its fiber matrix.

THIS PAGE INTENTIONALLY LEFT BLANK

VI. CONCLUSIONS

It has been shown that a composite plate consisting of a very hard first layer, a wave spreading 2nd layer, and a shock absorbing 3rd layer will perform better than conventional armor steel of equivalent areal density.

In this study, a D1 material model was developed to describe adequately Dyneema HB25. The mechanism of Dyneema failure can be described as elastic/plastic deformation, following by delamination. It is not effective to rely on Dyneema to resist penetration by shearing alone. As such, Dyneema on its own is not useful. When subjected to direct impact, the tendency to fail by shearing in the initial stages of impact degrades the later time performance of Dyneema substantially as sheared layers no longer contribute to energy absorption.

Ceramic has been shown to be important as a 1st layer to meet the incoming projectile. However, ceramics alone are not good armor materials because of their brittle fracture behavior. They convert a great deal of kinetic energy into fracturing their own matrix, but do not do the job of arresting the entire impact on their own. We expect that the ceramic layer will be even more effective against projectiles made of softer materials, where significant plastic deformation in the projectile will occur.

A wave spreading 2nd layer such as an advanced fiber composite, Dyneema, has proved to be an important asset in penetration resistance. By delaying the shock wave propagation in the 11-direction, it allows time for the shock energy to be dissipated through the target in the 22/33-directions.

Porous foam as a 3rd layer has proven to be a good shock absorber, and decreases the time taken to arrest the projectile. It does this by quickly absorbing the initial kinetic energy through pore compression and collapsing cell walls (PV-work), even before the Dyneema starts its delamination/deformation process. This reduces the amount of kinetic energy to be dissipated by the Dyneema, and hence reduces the time taken to arrest the projectile.

In this research, a higher density foam is shown to perform better than a lower density foam of the same thickness. This was shown in the Autodyn® simulations at a common velocity of 483m/s. A more dense foam configuration (C-D-P2-Al) had the lowest time taken to arrest the projectile, as well as the smallest overall deformation. *However*, this conclusion is counter intuitive because physically, a less dense foam of *equivalent* areal density is expected to produce a larger potential PV-work due to the larger void volume compression. Therefore, it is necessary that comparisons be done based on foams of the same area density in order to arrive at a better conclusion.

Through observations of the failure mechanism of each layer (fracture, energy absorption and energy dissipation), it is concluded that the sequence of the layering armor concept is fundamentally correct, and that the next stage of work would be to optimize the thicknesses and performance of each layer, as well as improving our ability to accurately model these materials.

VII. RECOMMENDATIONS FOR FUTURE WORK

A. ACTUAL DYNEEMA HB25 PROPERTIES

As all the properties used in the modeling of D1 were based on literature research, as well as making reasonable assumptions, it is necessary that physical material property experiments be done to ascertain these properties of Dyneema. Important parameters would include the sound speeds in the 11, 22, and 33 directions, Young's modulus, Shear modulus, and stress-strain relationships for Dyneema. Tests of stress-strain behavior at high strain rates of 100,000 s-1 should be done to derive the actual strength model for the Dyneema HB25 so as to model it more accurately using the Orthotropic Yield Function. In order to model the orthotropic softening behavior of Dyneema more accurately, it is recommended that the actual samples be tested to failure to ascertain the fracture energies in the 3 principle axes, and the maximum tensile and shear stress at failure so as to refine the Orthotropic Softening Failure model.

B. DESIGN OPTIMIZATION

With a more realistic material model of Dyneema, it will be possible to optimize the thickness of the various layers so as to increase the energy absorption characteristics, minimize deformation, and increase the ability to resist penetration from projectiles of even higher kinetic energies. It has been established that the sequencing of the layers is fundamentally correct. It is recommended that the next stage of work be focused on optimizing the thickness of each layer, as well as alternative better performance materials to enhance the penetration resistance of this composite armor.

C. MATERIAL CHOICE

Ceramics has been shown to work very well with the wave spreading properties of Dyneema. It has been shown that Dyneema cannot resist high velocity impact on its own, and its ballistic properties must be complemented by a very hard first layer to dissipate the initial impact energy. Momentum is conserved in the initial

projectile direction, but the materials used in this concept spread out the impulse effectively. A commercially available alumina (Al2O3) 98% technical ceramic has been used in this study. It is possible that other type of ceramic materials, such as Boron Carbide, Silicon Carbide, etc., may offer even greater hardness and fracture energies to plastically deform the projectile and absorb the initial impact energy. An emerging material science technology has shown the commercial viability of bulk glass metals which offer high hardness and yet ductility. These materials could prove to outperform technical ceramics. There are a variety of UHMWPE and Aramid fibers available in the market for experimentation, and it is possible that these types of materials can be used as a substitute for the Dyneema used in this experiment to investigate the relative performance of each. Carbon nanotubes have been known to have excellent fiber wave speeds of up to 20km/s, and these could prove to be even better wave spreading materials. Porous solid foam media has been shown to be effective in reducing the total deformation. It has been shown in this research that higher density foam performed better than a less dense foam of the same thickness. However, more work needs to be done in this area to draw better conclusions about the performance of porous foams in ballistic applications and investigate the effects of porosity and density on impact resistance.

D. HIGHER VELOCITY IMPACT

It is also observed from simulations that the failure mechanism is slightly different at different velocities. For example, at very high velocities of impact, the material is likely to undergo shearing first, before delamination and fiber elongation takes place. As such, it might be of value to improve the quality of the experiment with a higher velocity impactor, with the minimum kinetic energy of 1000J, in order to investigate the differing effects.

LIST OF REFERENCES

[1] C. W. Poh, "Investigation of New Materials and Methods of Construction of Personnel Armour,".M.S. thesis, Naval Postgraduate School, Monterey, CA, December 2008.

2 J. R. Robbins, J. L. Ding, and Y. M. Gupta, "Load Spreading And Penetration Resistance Of Layered Structures—A Numerical Study," *Int. J Impact Eng*., vol. 30(6), pp. 593–615, 2004.

3 Y. M. Gupta and J. L. Ding, "Impact Load Spreading In Layered Materials And Structures: Concept And Quantitative Measure," *Int. J Impact Eng.*, vol. 27(3), pp. 277–91, 2002.

4 M. L. Wilkins, "Mechanics Of Penetration And Perforation," *Int. J. Engng. Sci.*, vol. 16, pp. 793–807, 1978.

5 W. Herrman, "Constitutive Equation For The Dynamic Compaction Of Ductile Porous Materials," Sandia Laboratories, Albuquerque, New Mexico, December 12, 1968. Reprinted from *Journal of Applied Physics*, vol. 40, no. 6, pp. 2490–2499, May 1969.

6 C. W. Boey, "Investigation of Shock Wave Attenuation in Porous Materials." M.S. thesis, Naval Postgraduate School, Monterey, CA, 2009.

7 T. J. Holmquist and G. R. Johnson, "Response of Boron Carbide Subjected To High Velocity impact," *International Journal of Impact Engineering* vol. 35, pp. 742–752, 2008.

8 Century Dynamics, *Autodyn® Explicit Software for Nonlinear Dynamics Theory Manual, Revision 4.3*, 2005, 150-151.

9 C. E. Anderson Jr., G. R. Johnson and T. J. Holmquist, "Ballistic Experiments and Computations of Confined 99.5% Al2O3 Ceramic Tiles," 15th International Symposium on Ballistics, Jerusalem, Israel, 1995, pp. 65–72.

10 J. W. S. Hearle, *High Performance Fibers*. Woodhead Publishing, 2001, p. 36

11 Robert M. Jones, *Mechanics of Composite Materials*, 2nd ed. Taylor and Francis, Inc., 1999, pp. 68–70.

12 J. W .S. Hearle, *High Performance Fibers*. Woodhead Publishing, 2001, p. 78

13 J. K. Chen, F. A. Allahdadi, and C. T. Sun, “A Quadratic Yield Function For Fiber-Reinforced Composites,” *Journal of Composite Materials*, vol. 31(8), pp. 788–811, April 1997.

14 J. Rodriguez , I. S. Chocron, M. A. Martinez, and V. Sánchez-Gálvez, “High Strain Rate Properties of Aramid And Polyethylene Woven Fabric Composites,” *Composites Part B: Engineering*, vol. 27(2), pp. 147–4, 1996.

15 Century Dynamics, *Explicit Software for Nonlinear Dynamics - Composite Modelling in Autodyn®. Revision 1.0*, 2005, pp. 23–25.

16 G. R. Fowles and D. R. Curran, “Experimental Testing of Shock Attenuating Materials,” AFSWC-TDR-62–22, March 1962.

17 W. Herrman, “Constitutive Equation For The Dynamic Compaction Of Ductile Porous Materials.” Sandia Laboratories, Albuquerque, New Mexico, December 12, 1968. Reprinted from *Journal of Applied Physics*, vol. 40, no. 6, pp. 2490–2499, May 1969.

18 J. von Neumann and R. D. Richtmyer, “A Method For The Numerical Calculations Of Hydrodynamical Shocks,” *J. Appl. Phys*, vol. 23, pp. 232–237, 1950.

19 Jonas A. Zukas, *Introduction to Hydrocodes*. Elsevier Ltd., 2004, p. 289

20 J. A. Zukas and K. D. Kimsey, “Supercomuting and computational penetration mechanics,” in *Computational Aspects of Contact, Impact and Penetration*. R. F. Kulak and L. E. Schwer, Eds. Lausanne, Switzerland. Elmepress International, 1991.

21 SEM Photo taken by Ms. Harini Karunasiri, an intern at the Naval Postgraduate School, Monterey, CA, 2009.

INITIAL DISTRIBUTION LIST

1. Defense Technical Information Center
 Ft. Belvoir, Virginia

2. Dudley Knox Library
 Naval Postgraduate School
 Monterey, California

3. Professor Robert S. Hixson
 Naval Postgraduate School
 Monterey, California

4. Professor Jose O. Sinibaldi
 Naval Postgraduate School
 Monterey, California

5. Professor Larraza Andres
 Naval Postgraduate School
 Monterey, California

6. Professor Yeo Tat Soon
 Temasek Defence Systems Institute
 National University of Singapore
 Singapore

7. Tan Lai Poh (Ms), Assistant Manager
 Temasek Defence Systems Institute
 National University of Singapore
 Singapore